SLAC - 337
UC - 34D
(E)

Tests of QED to Fourth Order in Alpha in Electron-Positron Collisions at 29 GeV*

Christopher Allen Hawkins

Stanford Linear Accelerator Center
Stanford University
Stanford, California 94309

February 1989

Prepared for the Department of Energy
under contract number DE-AC03-76SF00515

Printed in the United States of America. Available from the National Technical Information Service, U.S. Department of Commerce, 5285 Port Royal Road, Springfield, Virginia 22161. Price: Printed Copy A06, Microfiche A01.

---

* Ph.D. Dissertation

Abstract

Tests of Quantum Electrodynamics to order α^4 in e^+e^- collisions using the ASP detector at PEP ($\sqrt{s} = 29$ GeV) are presented. Measurements are made of $e^+e^- \rightarrow \gamma\gamma\gamma\gamma$, $e^+e^- \rightarrow e^+e^-\gamma\gamma$ and $e^+e^- \rightarrow e^+e^-e^+e^-$ where all four final state particles are separated from the beam line and each other. These are the most precise and highest statistics measurements yet reported for these processes. The ratios of measured to predicted cross sections are

$$\gamma\gamma\gamma\gamma : 0.97 \pm 0.04 \pm 0.14$$
$$e^+e^-\gamma\gamma : 0.94 \pm 0.03 \pm 0.03$$
$$e^+e^-e^+e^- : 1.01 \pm 0.02 \pm 0.04$$

where the first uncertainty is the systematic uncertainty, and the second is the statistical uncertainty. All measurements show good agreement with theoretical predictions. A Monte Carlo method for simulating multi-pole processes is also presented, along with applications to the $e^+e^- \rightarrow e^+e^-\gamma\gamma$ and $e^+e^- \rightarrow \gamma\gamma\gamma\gamma$ processes.

The first measurements of five-body α^5 events (5γ, $e^+e^-\gamma\gamma\gamma$ and $e^+e^-e^+e^-\gamma$) and one candidate six-body α^6 event ($e^+e^-4\gamma$) are reported. Both the α^5 and α^6 measurements agree with estimates of their cross sections.

Acknowledgments

Working on the ASP experiment has been a challenging and rewarding experience for me. The small size of the collaboration coupled with the relatively short amount of time available to build the experiment led to a high level of vitality not often seen in larger High Energy Physics collaborations. This experiment would not have been possible without the hard work and long hours put in by the physicists and technicians who worked on the project. I am grateful to all the dedicated people who made this experiment a reality.

I would like to extend my special thanks to those with whom I have worked closest during my years as a graduate student. I thank my advisor, David Burke, whose has given me valuable advice and encouragement. I am indebted to Natalie Roe and Tom Steele, my fellow graduate students who, along with myself, were the core ASP working group for the last few years. Finally, I wish to thank Martin Perl, with whom I am writing two non-ASP papers. His creative thinking and encouragement were an inspiration to me.

I am especially grateful to my family and close personal friends who have given me so much encouragement and moral support over my many years as a student. In particular, I am eternally grateful to my wife, Mary, who showed me that there is much more to life than just physics. Her love and friendship have made my life a delight.

Contents

Tables

Figures

1

Introduction

1.1 Overview

This thesis presents measurements of Quantum Electrodynamics (QED) processes to order α^4. These measurements were performed with the Anomalous Single Photon (ASP) detector at the PEP e^+e^- storage ring with a center of mass energy of 29 GeV. Three event classes are studied:

$$e^+e^- \rightarrow \gamma\gamma\gamma\gamma$$
$$e^+e^- \rightarrow e^+e^-\gamma\gamma$$
$$e^+e^- \rightarrow e^+e^-e^+e^-$$

All four final state particles are required to be separated from the beam line and each other. Although the ASP detector was designed to do single photon counting, its large acceptance and good photon reconstruction ability makes it an excellent detector for studying these relatively rare high-order QED processes.

Comparisons are made of data with QED predictions. These QED predictions are based on calculations of all α^4 diagrams for each process. A Monte Carlo program written by Berends *et al.*[1] was used to obtain the prediction for $e^+e^- \rightarrow e^+e^-e^+e^-$. Matrix elements for $e^+e^- \rightarrow \gamma\gamma\gamma\gamma$ and $e^+e^- \rightarrow e^+e^-\gamma\gamma$ were available from Berends *et al.*[2,3], but it was necessary to develop an efficient Monte Carlo program. A Monte Carlo method for the simulation of multi-pole processes is presented in Chapter 3,

with applications to the $e^+e^- \rightarrow \gamma\gamma\gamma\gamma$ and $e^+e^- \rightarrow e^+e^-\gamma\gamma$ processes. This method is presented as a general method, and is fairly simple to understand and program for any multi-pole process.

1.2 Why Test QED?

The theory of Quantum Electrodynamics has been one of the most successful applications of Quantum Field Theory. The coupling constant α is small (1/137) which allows a straight forward application of perturbation techniques at low orders in α. Any deviation from QED is a good indicator of new physics. For example, the asymmetry measurements in $e^+e^- \rightarrow \mu^+\mu^-$ made at PEP and PETRA show deviations from pure QED and provide strong support for the merging of the Electromagnetic and the Weak forces into the single Electroweak force of the Standard Model.

Precision measurement of physical constants and cross sections require calculation of high-order QED radiative corrections to the lowest order processes. For example, the current $g_e - 2$ measurements test QED corrections to order $\approx \alpha^{10}$. Another example of more interest to high energy physicists are radiative corrections to the Z^0 width.

Many other physics measurements, such as exotic particle searches and missing energy events, have high order Bremsstrahlung terms as backgrounds. For example, the search for excited electrons looks for mass peaks in $e^+e^- \rightarrow e^+e^-\gamma\gamma$ events. Single photon and single electron measurements require calculations of QED backgrounds at least to order α^3, preferably to order α^4. Bremsstrahlung backgrounds in missing energy searches are particularly important for detectors that have gaps in their solid angle coverage or thin sections in which a photon can escape undetected.

One important question is why test QED to α^4 in e^+e^- collisions when it has already been tested to α^{10} in $g_e - 2$ experiments. First, the radiative corrections involved in the calculation of $g_e - 2$ involve vertex and self energy terms of the type shown in Figure 1.1. These do not involve the production of energetic particles, as do the tests of QED presented in this thesis. Secondly, the $g_e - 2$ experiments test QED at low momentum transfers, Q^2 ($Q^2 = \vec{q}^2 - q_0^2$, where q is the momentum four-vector),

whereas e^+e^- collisions allow tests at large Q^2. The effects of high mass particles become significant in vacuum polarization corrections at large Q^2, even though there is insufficient energy to produce these massive particles directly[4]. One may view the QED coupling constant α in much the same way as the strong coupling constant α_s is viewed. When the vacuum polarization diagrams (shown in Figure 1.2) are renormalized in order to obtain the physical value of α, the radiative corrections can be summed together and included in the definition of α. Thus α is a function of Q^2, like the strong coupling constant. In summary, one should recognize that testing QED at low Q^2 and low energies is not equivalent to testing QED at high Q^2 and high energies. This thesis presents tests of multi-particle production in QED at high energy ($\sqrt{s} = 29$ GeV), but it is not sufficiently sensitive to test the effects of loop corrections to the lowest order production diagrams.

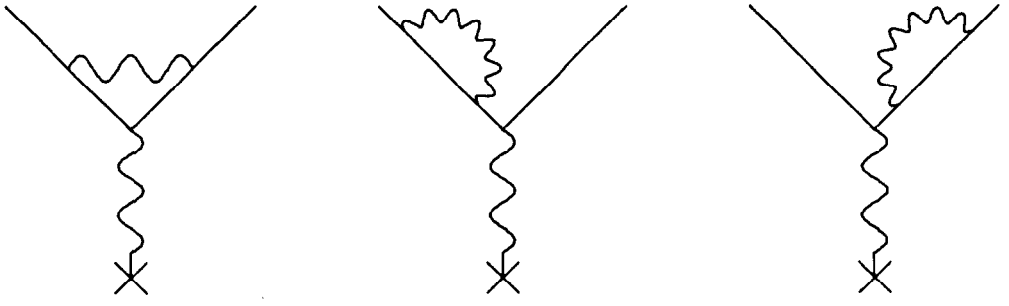

Figure 1.1. Examples of self energy and vertex diagrams that contribute to the $g_e - 2$ measurement.

Calculations of QED contributions above order α^3 are difficult due to the rapid proliferation of Feynman diagrams with increasing order. Similarly, the Monte Carlo integration techniques used to efficiently simulate four or more body final states are difficult due to the large number of poles in the cross section. The techniques used in making these calculations and Monte Carlo programs are difficult and tedious. Testing

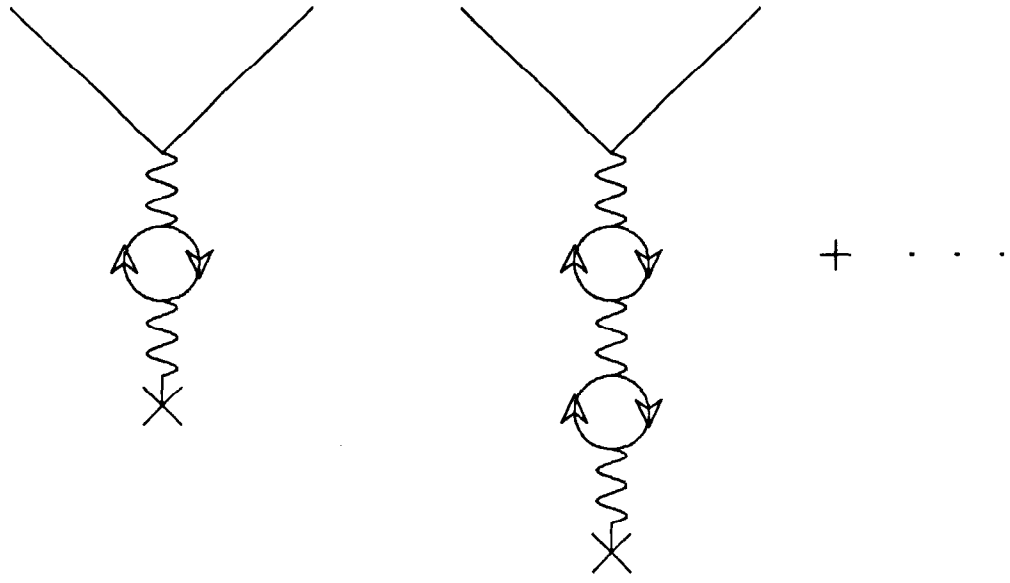

Figure 1.2. Vacuum polarization diagrams.

them with real measurements is crucial. The measurements presented in this thesis represent tests of QED calculations to order α^4, where all four final state particles are hard (in this case, above 300 MeV). All the calculations involve a large number of diagrams — 24 for $e^+e^- \rightarrow \gamma\gamma\gamma\gamma$, 40 for $e^+e^- \rightarrow e^+e^-\gamma\gamma$ and 36 for $e^+e^- \rightarrow e^+e^-e^+e^-$.

2

The ASP Detector

The ASP experiment was designed to detect single photons in the radiative production of weakly interacting particles. It was designed and built by a collaboration of physicists and technicians from SLAC, University of Washington and MIT. Its proposal was approved in May, 1983, and was fully installed and operational by November, 1984. It was located in region 10 of the PEP e^+e^- storage ring at the Stanford Linear Accelerator Center. PEP ran at a center of mass energy of 29 GeV, and had a typical luminosity of 2 x 10^{31} cm^{-2} sec^{-1}. The data analyzed in this thesis was taken from January, 1985 through April, 1986. After data taking was completed in 1986, the detector was dismantled and put into storage.

The goal of detecting single photons from initial state Bremsstrahlung required a number of design considerations. The photons tend to be low energy and at low angles, so it was necessary to have a detector with a low trigger threshold, good energy resolution and a large solid angle acceptance. The central photon calorimeter had to be finely segmented so as to reject background events, where the rejection criteria was based on photon origin and shower shape. The detector had to be completely hermetic down to a small angle with respect to the beam line in order to reject QED events, such as $e^+e^- \rightarrow e^+e^-\gamma$. The detector system had to include good on-line monitoring systems so as to maintain the stability of the system. Special diagnostic event triggers were required in order to later determine counter correction factors, energy reconstruction functions and integrated luminosity. The detector had to be

built and installed in a short amount of time (1.5 years) in order to take at least 2 years of data before PEP shut down. Lastly, budgetary constraints required the detector to be inexpensive. As you will see in the following sections, the ASP detector successfully met all these criteria.

2.1 The Detector in Brief

The primary element of the ASP detector is the lead-glass calorimeter. It is made up of 632 lead-glass bars with phototube read out arranged in four quadrants in a pinwheel design (see Figure 2.1). The bars are placed with their long axis transverse to the beam line and are stacked into 5 layers within each quadrant. Alternate layers are staggered in Z by half a bar width (see Figure 2.2). This arrangement leaves no gaps in azimuth or polar angle down to the edge of the lead-glass detector. Planes of proportional wire chambers (PWC) are placed between the lead-glass layers and provide azimuthal tracking. A central tracker made of thin walled PWC cells surrounds the beam pipe, providing charged particle tracking. Between the central tracker and the lead-glass calorimeter is a set of veto scintillators which provide some redundancy to charged particle identification. Above the central detector is mounted a time of flight system made of scintillator which allows the efficient rejection of cosmic ray events. The low polar angle region is covered by four modules of lead/scintillator sandwich shower counters. Planes of PWC are placed 6 radiation lengths (X_0) into each module and provide shower reconstruction in the X and Y coordinates. Eight planes of drift chambers provide precise tracking for the outermost shower counter modules. The detector is completely hermetic down to 21 milliradians with respect to the beam line.

The beam pipe is thin walled vacuum chamber made of aluminum and stainless steel. The relevant parameters are given in Table 2.1 . The detector acceptance was further defined by a tungsten and lead mask placed in an indentation in the beam pipe. This mask covered the region from 15 to 21 mrad. It also helped to protect detector elements from off-energy beam electrons over-focused by the focusing quadrupole magnets. Without the mask, these particles could intercept the beam pipe at grazing

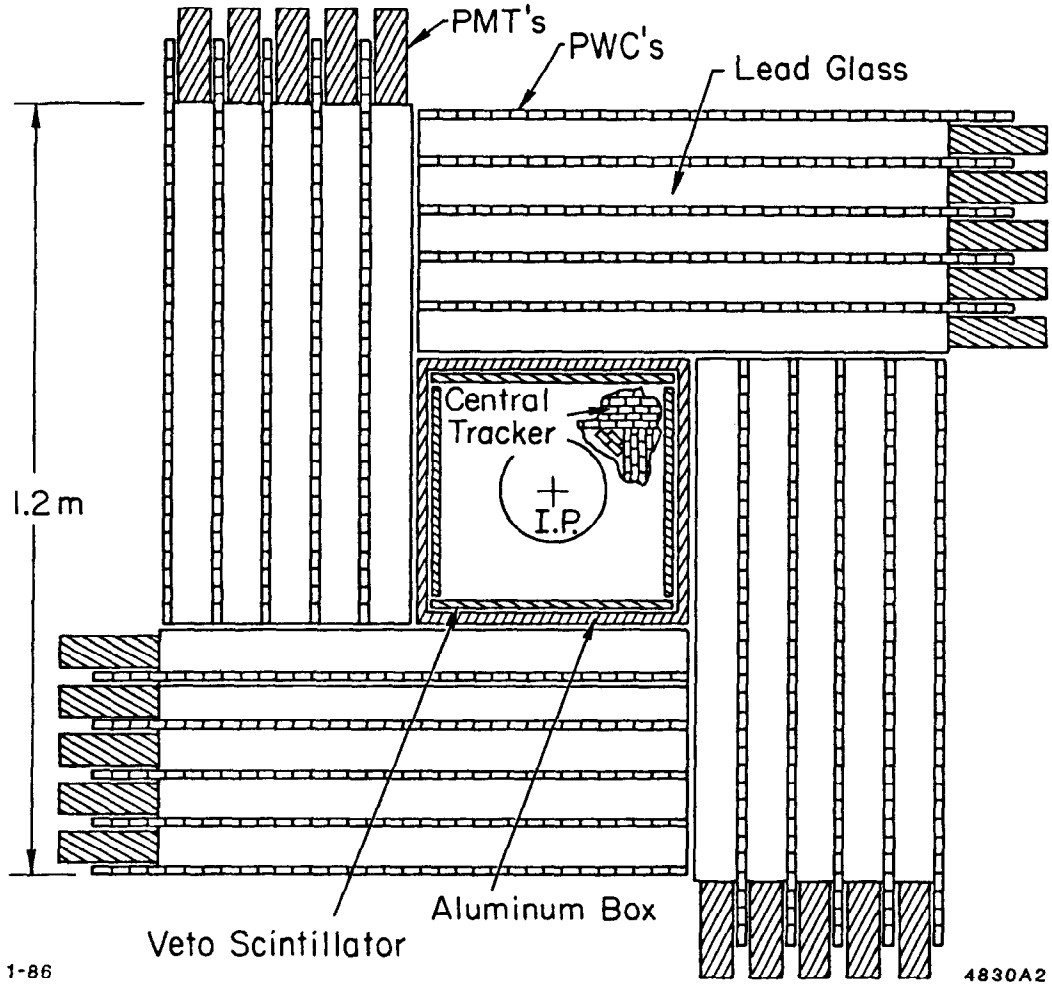

Figure 2.1. Cross section in the x-y plane of the central calorimeter and tracking system. Only a section of the central tracker is shown; it completely surrounds the interaction point (IP).

angles and create background problems in the detector.

2.2 Coordinate System

The detector coordinate system is a right handed system centered on the nominal beam interaction point. The Z axis is along the positron direction, the Y axis is pointed up and the X axis points to the inside of the PEP ring. Azimuth (ϕ) and polar angle (θ) have their usual definitions. Due to the square nature of the central

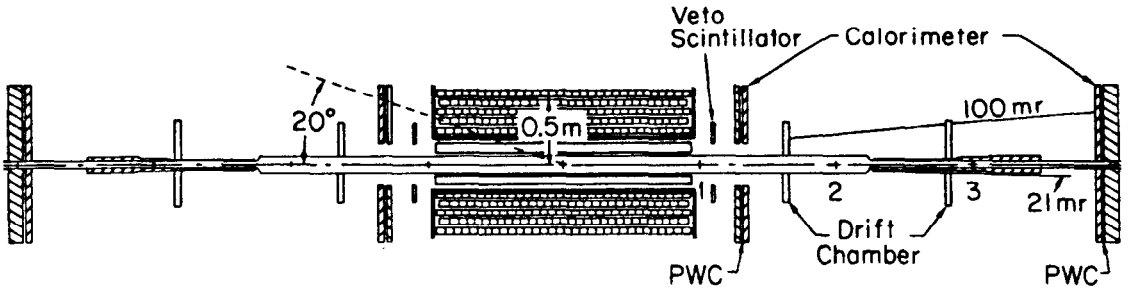

Figure 2.2. A vertical cross section of the ASP detector through the beam axis. The apparatus is 8.8 m long and 1.2 m wide.

Table 2.1. ASP Beam Pipe Materials.

Angle (mrad)	Material	Thickness at Normal Incidence in Radiation Lengths
> 100	120 mil Al	0.034
$50 - 100$	100 mil Al	0.029
$45 - 50$	Al-stainless weld	–
$30 - 45$	stainless flange	3.5
$27 - 30$	60 mil stainless	0.027
$21 - 27$	60 mil stainless @ 30°	0.027

detector geometry, it is more useful to use azimuth and projected polar angle as defining angles in the detector. The projected polar angle, θ_p, is the angle made between the Z axis and a line projected into the XZ or YZ plane. The relationship between θ and θ_p is

$$\tan\theta_p = \tan\theta \cdot \max(|\cos\phi|, |\sin\phi|) \tag{2.1}$$

This is a natural coordinate for the central detector since the lead-glass array measures θ_p, not θ, and the full acceptance is best defined by θ_p.

2.3 Experimental Hall

PEP region 10 (IR-10) is located underground with approximately 20 meters of earth above it. This earth shield reduced the cosmic ray rate by a factor of 2.5 relative to the surface rate. The nearest entrance to the PEP tunnel was located at region 8, 0.43 kilometer away. All detector components were constructed in modules that could be shipped down the tunnel and then installed in IR-10.

The environment in IR-10 was originally adversely affected by an intake air shaft in the hall. The air would cool as it came down the shaft, causing high humidity and large temperature variations in the IR hall. This was very detrimental to the detector electronics. The direction of air flow was reversed so that warm, dry air (heated by the ring magnets) flowed from the PEP tunnels into the IR hall. The temperature was then stable at 29±2°C, with a relative humidity of about 50%. This temperature stability was important in maintaining the stability of the detector electronics, the gas gain in the PWC systems and the drift velocity of the gas in the drift chambers.

Region 10 is located directly downstream of the PEP e^- injection line. Extra lead shielding was placed around the detector in order to minimize radiation damage during injection periods. The central lead-glass boxes were mounted on rails and could be retracted behind lead brick walls during injection for extra protection from radiation damage. This is described further in Section 2.6.1.

2.4 Calibration and Monitoring

All detector subsystems were monitored and calibrated frequently in order to assure stability and reliability. A full electronic calibration was performed at least once every eight hours during data taking periods. A fraction of the triggers were analyzed on-line to monitor actual device responses. The gain of the gas used in the PWC and drift chamber systems was monitored for short term stability by a set of gas monitors, described in Appendix A.

Special triggers recorded event classes that were used for diagnostics purposes and off-line calibration. These include Bhabha events, radiative Bhabha ($e^+e^- \rightarrow e^+e^-\gamma$) events, cosmic rays and random beam crossings. Low angle Bhabha events were used

for determining the experiment's luminosity and setting the energy scales for the forward calorimeters. Cosmic rays were used to set correction factors for individual detector elements. Random triggers were used for occupancy studies.

Radiative Bhabha events were crucial for the determination of the central calorimeter's energy correction functions and for efficiency studies. The radiative Bhabha trigger required a low angle particle (into the forward calorimeters) on each side in Z with energy greater than about 7 GeV, along with at least 200 MeV of signal in the lead-glass calorimeter (see Figure 2.3). These events were tracked off-line and then kinematically fitted with a modified version of kinematic fitting program SQUAW[5]. The number of such events passing the χ^2 criteria for the kinematic fit varied depending on the cuts applied in a particular analysis, but one could expect 40,000 to 85,000 events to pass. By comparing the energy as determined by a kinematic fit in which the lead-glass track's energy was left out to the raw signal in the detector, functions were found which convert raw signal to energy given the angles and shower starting point of the track. The tracking efficiency of the lead-glass calorimeter was studied with $e^+e^-\gamma$ events that had an electron in the central detector. Only the track parameters from the central tracker system for the lead-glass track were used when performing the kinematic fit, and the results of the fit were then used to study the lead-glass tracking. Kinematically fitted events were also used to set scales and determine correction functions in the detector Monte Carlo simulation programs. This was done by taking the track parameters for the central track from the kinematic fit result and then passing these parameters on to the Monte Carlo simulation program. The simulated detector response was then compared directly with the actual response on an event by event basis.

2.5 Luminosity

The detector luminosity was determined by analyzing low angle Bhabha events, recorded by a special low angle Bhabha trigger. An off-line luminosity analysis looked for events that had a track in the 55-95 mrad region on one side, a track in the 50-100 mrad region on the other side, and less than 0.5 GeV of energy in the central

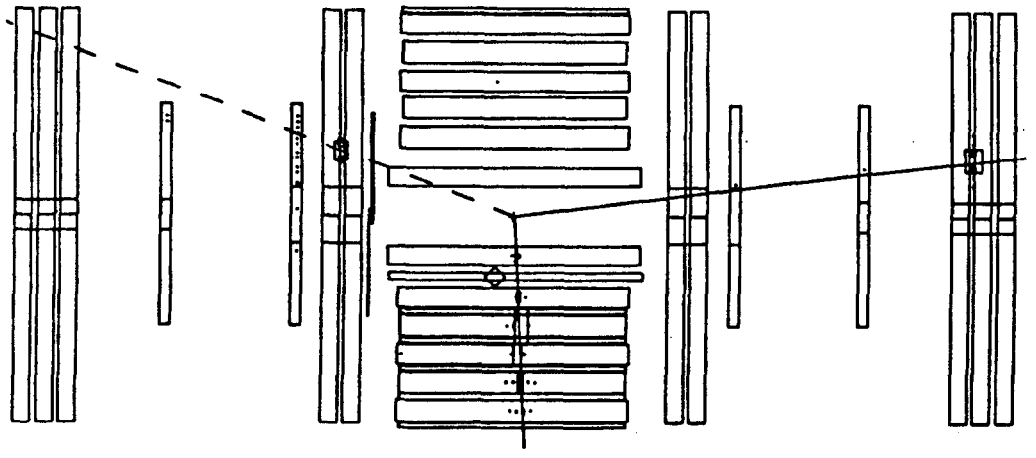

Figure 2.3. An example of a diagnostic $e^+e^- \rightarrow e^+e^-\gamma$ event. Such events were tracked and kinematically fitted, then used to study detector responses.

calorimeter. The two tracks were also required to be colinear to within 20 mrad. This yielded a luminosity of

$$109.56 \pm 0.48 \text{ (stat)} \pm 0.83 \text{ (syst)} \pm 0.79 \text{ (QED)}$$

The first uncertainty is statistical, the second is the systematic counting error and the third is an estimate of the uncertainty in the QED prediction. These values were compared with a less accurate wide angle Bhabha and $e^+e^- \rightarrow \gamma\gamma$ analysis, which agreed with the low angle analysis to a few percent. Details about the luminosity analysis may be found in Appendix B.

2.6 Central Detector

2.6.1 Calorimeter

The central calorimeter consists of lead-glass bars and interleaved PWC elements, as described in Section 2.1. The lead-glass provides the energy measurement and tracking in the X-Z and Y-Z planes. The PWC system provides tracking in the X-Y plane.

The lead-glass bars are extruded F2 (Schott) type bars and measure $6 \times 6 \times 75$ cm^3. The composition is given in Table 2.2 . The lead-glass has a radiation length of 3.17 cm and an index of refraction of 1.58. It is doped with 0.35% cerium in order

to increase its radiation hardness. The extrusion process was chosen over a cut and polish technique because it is much cheaper. This process leaves surface ripples on the scale of a few millimeters, but which are smooth on the order of optical wavelengths. It has been shown that the optical properties are equivalent to polished lead-glass bars[6].

Table 2.2. Lead-glass composition.

Element	Percentage Composition
Lead	41.8
Oxygen	29.7
Silicon	21.5
Sodium	3.7
Potassium	3.3
Cerium	0.35

The Čerenkov light emitted by particles traversing the lead-glass is collected by 12 stage Amperex XP2212C photo multiplier tubes (PMTs) mounted on the outside end of each bar. A square printed circuit board, slightly smaller than a bar cross section (6 x 6 cm), was mounted on the end of each tube and contained the voltage divider ladder and capacitors. Each tube was glued to the end of its bar with clear Stycast 6061 optical epoxy. The photocathode covered 42% of the surface area of the end of the bar. A μ-metal shield was placed around each tube in order to minimize the effect of external magnetic fields. Each bar was then wrapped in aluminum foil on the remaining five sides.

Prior to assembly, each PMT was calibrated with a green Hewlett-Packard Superbright (HLMP-3950) LED. Operating voltages were selected so that all tubes had similar gain factors. When the calorimeter was assembled, PMTs with similar voltages were grouped together in groups of seven to eight. The group was powered

by a single high voltage channel. Precise voltages for each tube were obtained from the single high voltage channel by a resistive divider. The gains of the PMTs were monitored on-line with HLMP-3950 LEDs. There was a single LED per quadrant which was viewed by each tube through a fiber optic network. The LED response was monitored by a reference PMT. The stability of this PMT was monitored in turn by checking its response when viewing a small NaI(Tl) scintillator crystal doped with Am^{241}, which served as a stable light source. This on-line calibration system was used only to monitor relative stability during data taking. Absolute calibration for each PMT was provided by an off-line analysis which looked at the response of each PMT to cosmic ray muons traversing the bar.

The PWC system was made of 80 chambers with eight cells per chamber. There were 4 chambers per plane and 5 planes per calorimeter quadrant. The eight cell chambers were two meters long, eight inches wide and 5/8 inch thick. They were extruded aluminum chambers with 1/16 inch thick walls (see Figure 2.4) chemically etched to provide a smooth surface. This geometry provided the high strength necessary to support the lead-glass layers. Each cell was strung with one 48 μm gold plated tungsten sense wire. The PWCs were operated with a gas mixture of 95% Argon and 5% CO_2 which flowed through the chambers at atmospheric pressure. The short term gas gain was monitored by a gas monitor tube (Appendix A) mounted on the exhaust line for each quadrant. The absolute calibration was obtained from an off-line analysis of Bhabha events in the central detector.

The lead-glass bars were stacked into aluminum boxes made of 3/4 inch aluminum. The two lower boxes were mounted on rails and bolted to the boxes above so that the detector could be split into two L shaped halves. A remotely controlled hydraulic motor system allowed the detector to be opened for easy access to central detector elements or for protection during e^- injection periods. Lead brick walls protected the calorimeter from radiation damage (during injection) when the boxes were in the retracted position.

The combined lead-glass and PWC systems allowed full 3-dimensional reconstruction of both charged and neutral particle trajectories. The resolution in

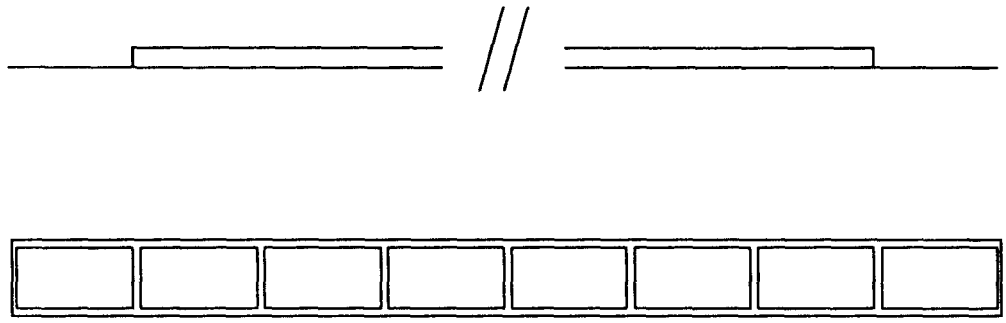

Figure 2.4. Side and end views of the chambers used for the central and forward PWCs. The forward PWCs differ from the central only in length.

projected theta (θ_p) averaged over all angles is 1.9° for high energy tracks, worsening to 4.4° for low energy tracks (0.5 to 3 GeV). The angular dependence is shown in Figure 2.5 for high energy tracks. The resolution in ϕ averaged 3°.

Energy reconstruction was dependent on the angles and conversion point (for photons) of the track. Light attenuation functions in the lead-glass bars were determined using cosmic ray muons. Shower leakage, preradiation in material before the lead-glass and absorption of energy in nonactive elements within the calorimeter were studied using the EGS4[7] shower simulation code. Overall normalization was provided by kinematically fitted $e^+e^- \rightarrow e^+e^-\gamma$ events. After all such corrections were made, an average resolution of $\sigma_E/E = 10.0\%/\sqrt{E}$ was obtained[8].

2.6.2 Central Tracker

The central tracker (CT) consisted of 192 aluminum PWC tubes arranged in 4 quadrants of 5 layers each[9]. Each tube was 2 m long and 1.0 x 2.3 cm^2 in cross section. The tubes ran parallel to the beam line and were staggered in XY view (see Figure 2.6). This left no gaps as seen from the beam line so that no charged particle could traverse it undetected. The tubes were chemically etched to a 0.012 inch wall thickness in order to reduce the amount of material between the beam pipe

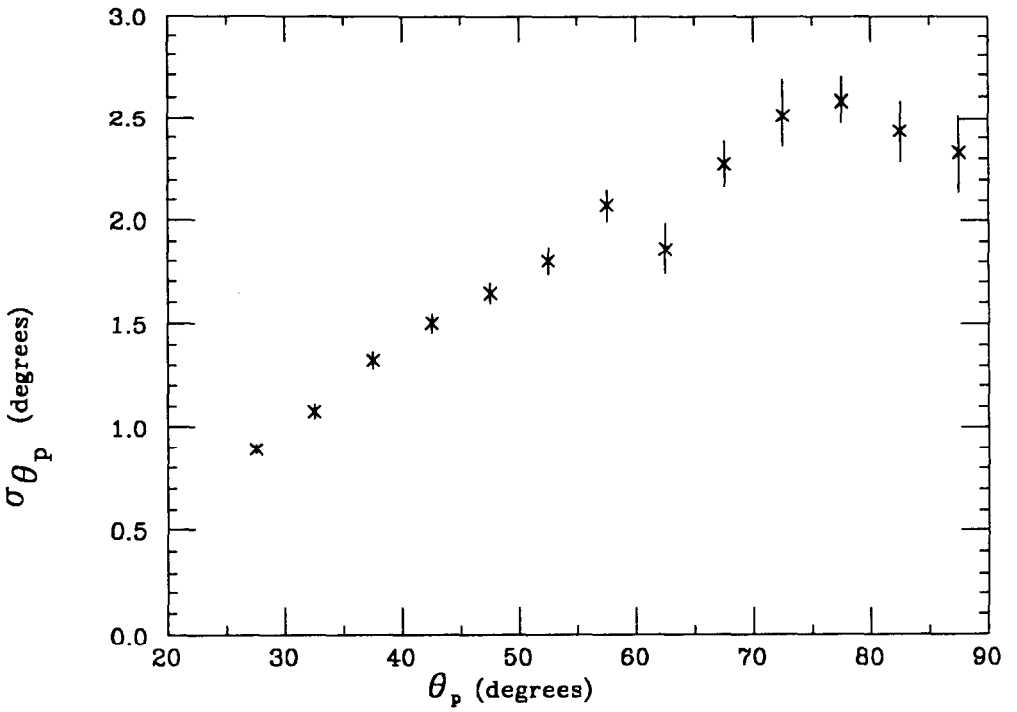

Figure 2.5. The resolution of θ_p versus θ_p for 14.5 GeV tracks.

and the calorimeter, thus reducing the γ conversion rate. They were strung with 5 μm Stablcohm 800 stainless steel resistive wire (200Ω/ft). Both ends of the wire were read out so that a Z position could be obtained by charge division. The tubes in a quadrant were glued together and mounted on a hexcel backplate fitted to form a box around the beam pipe. The central tracker did not retract with the calorimeter boxes. The CT was operated with a gas mixture of 48.3% argon, 48.3% ethane and 3.4% ethyl alcohol vapor. The short term stability of the gas was monitored with a gas monitor tube placed on the exhaust line of the CT.

2.6.3 *Veto Scintillators*

A set of veto scintillators (VS) was mounted between the central tracker and the central calorimeter boxes (see Figure 2.6). They provided a backup to the central tracker for charged particle identification and also were useful for triggering on cosmic rays. There were four scintillators measuring 2 cm thick by 33.5 cm wide and 225 cm long. Wavebar was placed along the ends of each and read out with the same type of

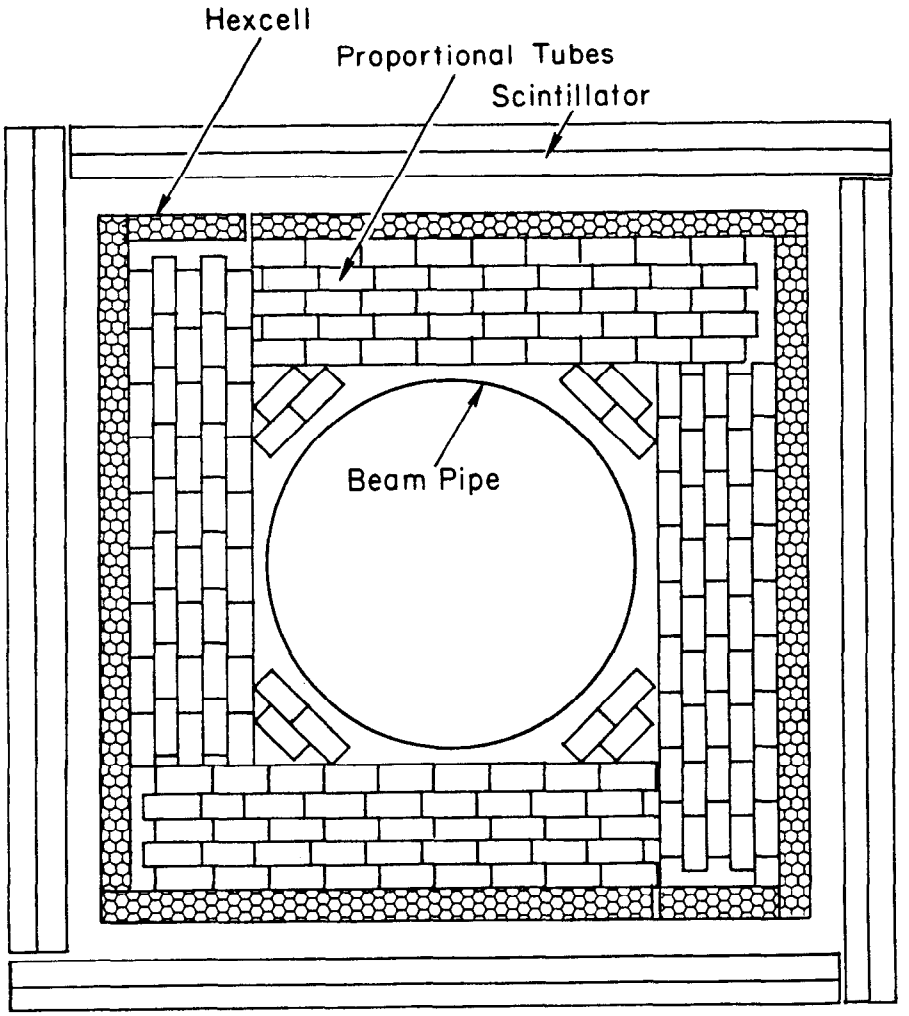

Figure 2.6. Cross section in the x-y plane through the Central Tracker and surrounding Veto Scintillators.

PMTs used by the lead-glass system. A Z position was obtained by comparing the signal at each end.

Another set of veto scintillators was mounted between the central tracker and the inner forward shower counters. These extended the coverage of the VS system to within 90 mrad of the beam line. More details on the VS system may be found in Appendix C.

2.6.4 Time of Flight System

The time of flight (TOF) system consisted of 48 scintillators suspended from the ceiling over the central detector. They were used to reject cosmic ray events by comparing timing information from the lead-glass system with the TOF system. Each scintillator was 3.45 m long, 20 cm wide and 2.5 cm thick, and was mounted with its long axis parallel to the beam line. The light from the scintillator was gathered by light guides placed on both ends and read out by PMTs. A Z coordinate could be obtained by comparing the signals at each end.

2.7 Forward Detector

2.7.1 Forward Calorimeter

The forward shower counter (FS) system consisted of four calorimeters made of lead sheet and scintillator sandwich with an interleaved PWC system used for position measurements (see Figure 2.7). These calorimeters were located at ± 1.56 m and ± 4.0 m in Z (refer to Figure 2.2). The inner units' coverage overlapped with the central calorimeter and the outer units, so that there were no gaps in calorimeter coverage between systems. The inner units extended down to 100 mrad, and the outer units extended below the beam pipe mask of 21 mrad.

Each calorimeter consisted of submodules of lead-scintillator sandwich mounted inside a box made of 0.5 inch aluminum. Each module was a total of 6 radiation lengths thick (5.5 inches), 49 inches high and 49 inches wide. The outer units consisted of 3 such modules (18 X_0) and the inner units consisted of 2 modules (12 X_0). A module could be split into halves for easy installation around the beam pipe. This split was notched, creating a 4 cm overlap between halves, so that there was no gap through which a particle could escape undetected. Each module was read out on four sides by wave bars and PMTs.

Planes of PWC tubes were placed between the first and second modules of each calorimeter units. This position is 6 X_0 in depth, which corresponds to the approximate location of the peak of the charged particle number distribution in showers

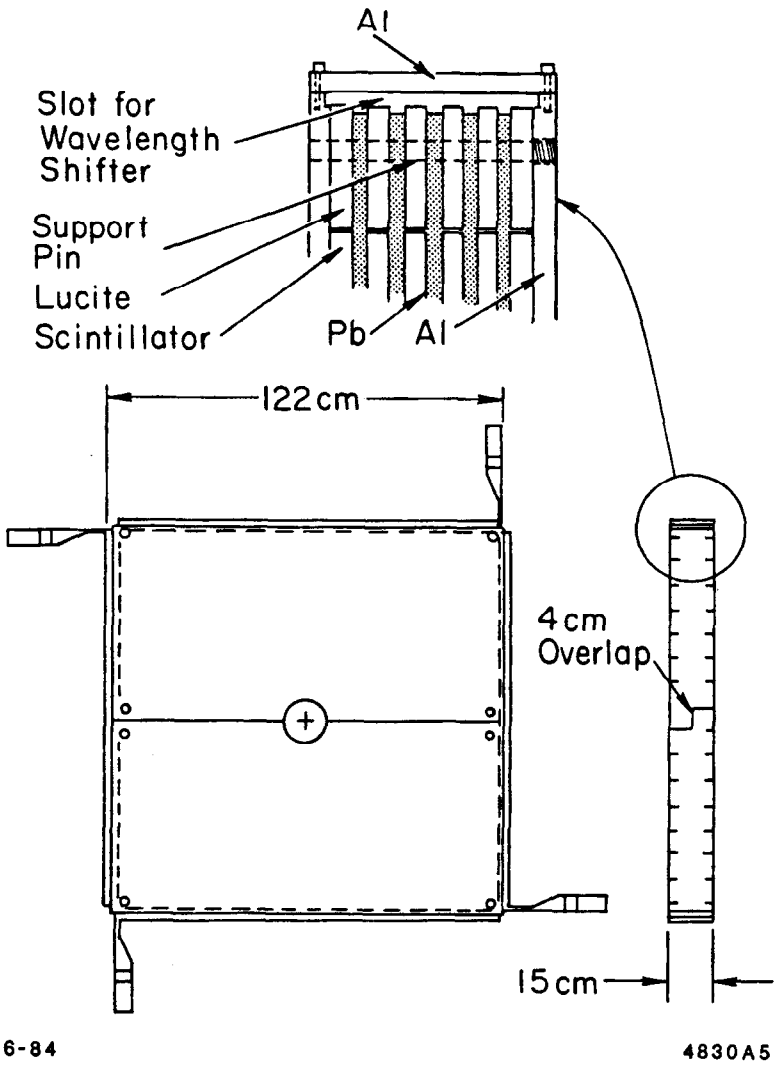

Figure 2.7. Front and side views of a forward shower counter module. The inset shows details of the construction of a corner of the module.

initiated by 14.5 GeV electrons. There were two planes of PWC — one measured X and the other Y. Each plane consisted of 6 chambers of the same type used in the central calorimeter. Chambers next to the beam pipe were cut in order to fit around the pipe. The wires from opposite sides of a cut cell were connected by a 50Ω coaxial cable so that only one channel of electronics was necessary to read them out. The PWC was operated with a gas mixture of 95% argon and 5% CO_2. The short term

relative gas gain was monitored with a gas monitor tube on the exhaust line for each unit. The position resolution for the PWC system was 8 mm in X and 7 mm in Y for Bhabha events. This corresponds to $\sigma_\theta = 2$ mrad for the outer calorimeters. More details on the forward PWC (FP) system design and performance may be found in Appendix D.

Energy reconstruction in the forward system required the measurement of the XY position with the FP system due to large attenuation factors in the scintillator. Energy correction functions were obtained by analyzing the response from colinear Bhabha events. The energy resolution was a function of angle, but was typically $\sigma_E/E = 20\%/\sqrt{E}$ to $25\%/\sqrt{E}$ above 50 mrad. Below 50 mrad, the resolution was severely deteriorated due to the flange in the beam pipe and radiation damage to the scintillator at low angles. The resolution at 21 mrad was $\sigma_E/E = 40\%/\sqrt{E}$. The energy scale for lower energy tracks was checked using kinematically fitted $e^+e^- \rightarrow e^+e^-\gamma$ events. The agreement was good to the 2% level (the level of accuracy of the analysis), showing no dependence of the energy correction function with energy.

2.7.2 *Drift Chambers*

Eight planes of drift chambers (4 in X and 4 in Y) aligned transverse to the beam line allowed precise reconstruction of charge particle trajectories below 100 mrad[8]. They were located at 4 locations along the beam line, at $\pm$ 1.9 m and $\pm$ 3.0 m from the IP. These chambers were essential in precisely determining the position corrections for the forward PWC system and determining the beam spot position using colinear Bhabha events. The increased precision of particle angles over the FP system was also useful in making kinematic fits to $e^+e^- \rightarrow e^+e^-\gamma$ events. However, their overall performance was limited because charged particles tend to start showering in the beam pipe, thus causing many hits in the chambers.

2.8 Trigger and Data Acquisition

The trigger decision was based on analog sums of the lead-glass, forward shower counter and central veto scintillator signals. In addition to the previously mentioned

low angle Bhabha, radiative Bhabha, cosmic and random triggers, there were also a number of triggers optimized for detecting events that deposit energy in the lead-glass system. The first trigger simply required 1.5 GeV of signal in the lead-glass system, irregardless of the pattern of the energy deposition. Three others (optimized for the single photon search) had lower energy thresholds, but required layer deposition patterns in the lead-glass that were consistent with a particle coming from the beam line. One of these three also vetoed on energy in the forward shower counter signal. Only the total energy trigger at 1.5 GeV and the radiative Bhabha trigger were required for the analysis in this thesis. The lead-glass trigger is shown schematically in Figure 2.8 and Figure 2.9.

The trigger decision process took about 1 μs, whereas the time between beam crossings was $\approx$2.4 μs, so no dead time resulted from the trigger decision process. If the trigger fired, the digitized data was read by the experiment's VAX 11/750 computer, written to disk and then dumped to tape as the disk filled. Total read out of the system took about 10 ms, and the trigger fired at an average rate of about 4.5 Hz.

Signals from the forward and central calorimeter phototubes were split, with one of the split signals going to summing circuits followed gated integrators and Lecroy ADC modules, and the other split signal going to a BADC/SHAM IV$^{(10,11)}$system for individual phototube read out. The secondary ADC read out was particularly important for the lead-glass system. The gain of the PMTs was set high so as to optimize the response to low energy photons. Unfortunately, the SHAM channels would begin to saturate for energies above 7 GeV. The secondary ADC did not have such a severe saturation problem, and so the ADC layer sum value was used to perform a saturation correction to the data during the off-line analysis stage.

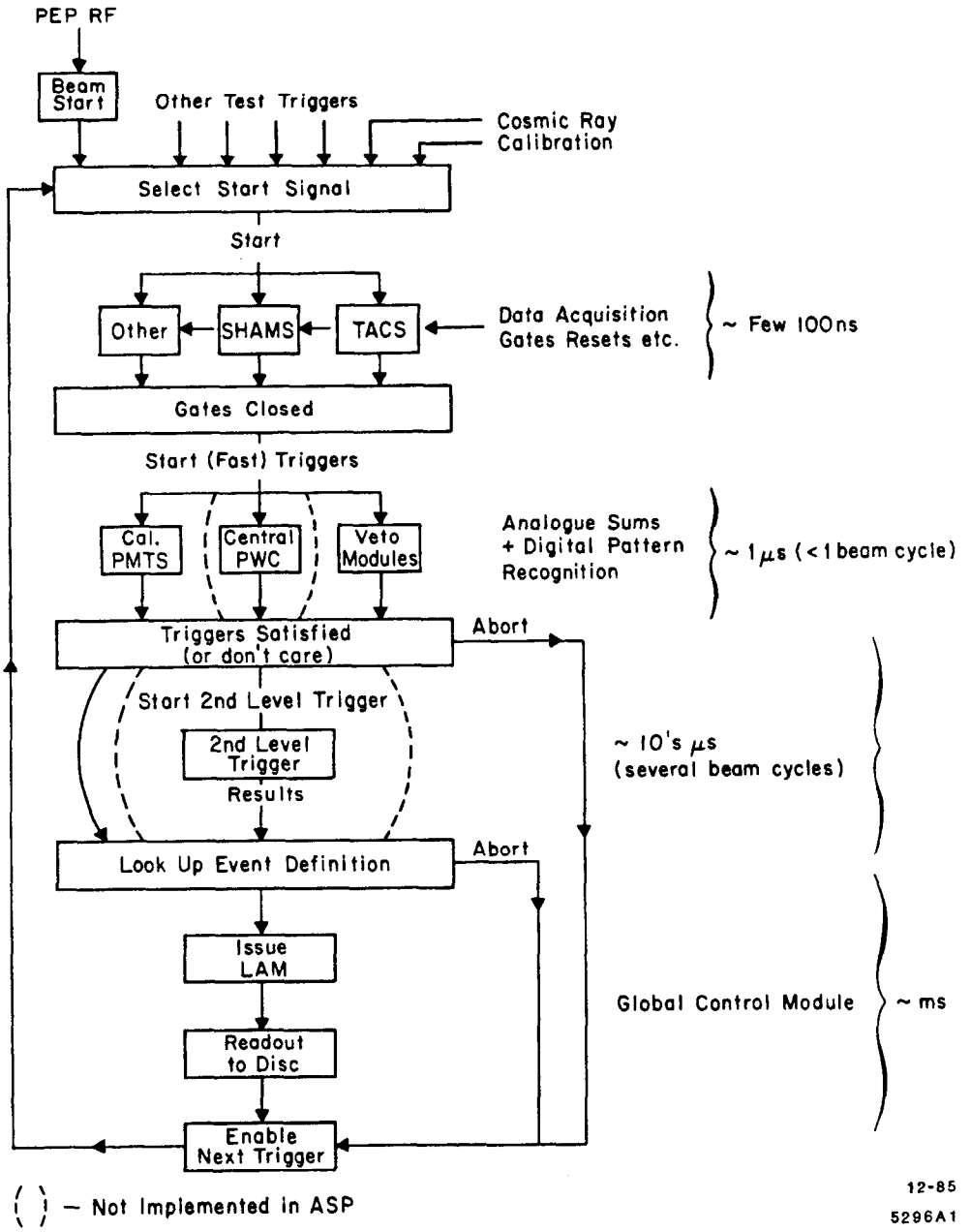

Figure 2.8. Flowchart of the overall trigger timing. The elements of the chart enclosed in dotted brackets could have been implemented if necessary.

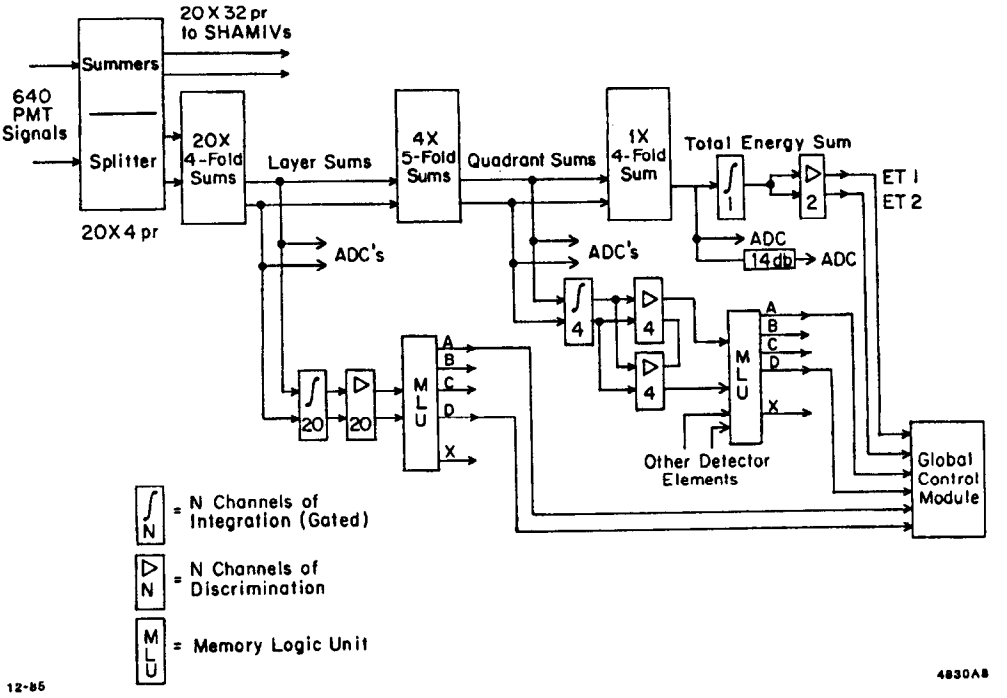

Figure 2.9. Schematic layout of summing circuitry for forming the lead-glass energy triggers.

3

Monte Carlo Event Generation

Efficient Monte Carlo simulation is essential to testing QED to fourth order. While writing a fourth order Monte Carlo program is never easy, programs that are restricted to particular poles in the cross section or programs that are restricted to sampling phase space far away from any poles are easier to write and are more efficient than those that sample phase space near many different types of poles. The reason for these efficiency problems for this last type of program is explained in detail in Section 3.2.

Fortunately, a Monte Carlo program for the $e^+e^- \to e^+e^-e^+e^-$ case written by Berends *et al.*[12] was available at SLAC. This program uses all 36 Feynman diagrams that contribute to this process at fourth order. The version used was optimized for the double tagging case. Despite the complicated procedure used in the program to optimize the efficiency, only an average of five unweighted (*i.e.* weight = 1) events within the detector acceptance were produced per CPU minute on the IBM 3081 at SLAC.

No efficient programs were available for the $e^+e^- \to e^+e^-\gamma\gamma$ and $e^+e^- \to \gamma\gamma\gamma\gamma$ cases, although matrix elements had been calculated for both cases using all contributing diagrams at fourth order[2,3]. In Section 3.1.3 a procedure is described for the relatively efficient generation of multi-pole processes, with applications to the $e^+e^- \to e^+e^-\gamma\gamma$ and $e^+e^- \to \gamma\gamma\gamma\gamma$ cases in the following sections. The procedure is similar to the one used for the $e^+e^- \to e^+e^-e^+e^-$ Monte Carlo, but is simpler to

program for one who is not an expert at calculating high order QED diagrams. The Berends, Daverveldt and Kleiss $e^+e^- \rightarrow e^+e^-e^+e^-$ program required the calculation of sets of gauge invariant diagrams, whereas the procedure shown in Section 3.1.3 only requires knowledge of the approximate functional behavior of simple kinematic variables in the region of the poles.

All generated events must be passed through a detailed detector simulation program — a slow process in terms of CPU time. The detailed detector simulation is required because track reconstruction relies on fitting a line through the shower clusters in the calorimeter. The track reconstruction can be sensitive to normal shower fluctuations and the degree of overlap between two showers of nearby particles. The behavior of the tracking in the case of multiple particle showers can't be well described by an efficiency function or look up table, but the behavior is reproduced by the detector simulation program. Since detector simulation is slow, only unweighted events are simulated. The detector simulation is described in Appendix E.

3.1 Review of the Monte Carlo Method

The Monte Carlo technique is a way of numerically evaluating integrals which can't be easily evaluated analytically. The difficulties with analytic calculations generally involve a highly complicated integrand (including efficiency functions, etc.) and/or complicated limits of integration. The Monte Carlo method that follows will be presented in terms of the e^+e^- scattering cross section case, as well as a few simple examples.

The total cross section in e^+e^- scattering can be written as

$$\sigma = \frac{(2\pi)^4}{4\sqrt{(p_+p_-)^2 - m_1^2 m_2^2}} \int |M|^2 d\Phi_n \tag{3.1}$$

where $|M|^2$ is the scattering matrix element squared and $d\Phi_n$ is the Lorentz invariant phase space element for the n-body phase space. In high energy e^+e^- scattering, the square root in the denominator may be replaced by $s = E_{cms}^2$. The matrix element is calculated by evaluating the Feynman diagrams for the process. The Lorentz invariant

phase space for a initial system with total momentum and mass P, M going to n final state particles with momenta and mass p_i, m_i is given by

$$d\Phi_n(P; p_1, \cdots, p_n) = \delta^4(P - \sum_{i=1}^{n} p_i) \prod_{i=1}^{n} \frac{d^3 p_i}{(2\pi)^3 2E_i} \tag{3.2}$$

In particular, the 2-body phase space element is

$$d\Phi_2(P; p_1, p_2) = (2\pi)^{-6} \frac{|\vec{p}_1^*|}{4M} d\Omega_1^* \tag{3.3}$$

where $|\vec{p}_1^*|$ is the momentum of particle 1 in the M rest frame and $d\Omega_1^*$ is the differential solid angle element in the M rest frame.

The Monte Carlo method is shown schematically in Figure 3.1. One first randomly selects (generates) a point in phase space. This point will have an associated phase space weight which corresponds to the evaluation of the denominator in equation 3.2 and any extra factor due to change of variables. (The subroutine which picks a phase space point and returns the four-vectors and the phase space weight is called the phase space generator.) $|M|^2$ is then evaluated for this point in phase space, multiplied by the phase space weight, and then multiplied by the normalization factors in equation 3.1. This is then the total weight for the event. Events that are outside the experimental acceptance are given a weight of zero. The total cross section is simply the average weight, *i.e.* the sum of weights for all events divided by the number of times a random point in phase space was selected (referred to from now on as the number of tries, N_{try}).

$$\sigma = \langle W \rangle = W_{sum}/N_{try} \tag{3.4}$$

An estimate of the uncertainty in the cross section is simply the standard error of the mean.

$$\delta\sigma = \sqrt{\frac{\langle W^2 \rangle - \langle W \rangle^2}{N_{try} - 1}} \tag{3.5}$$

The procedure described above evaluates the total integral within some set of experimental cuts using weighted events. The occupancy distributions (energy, angle,

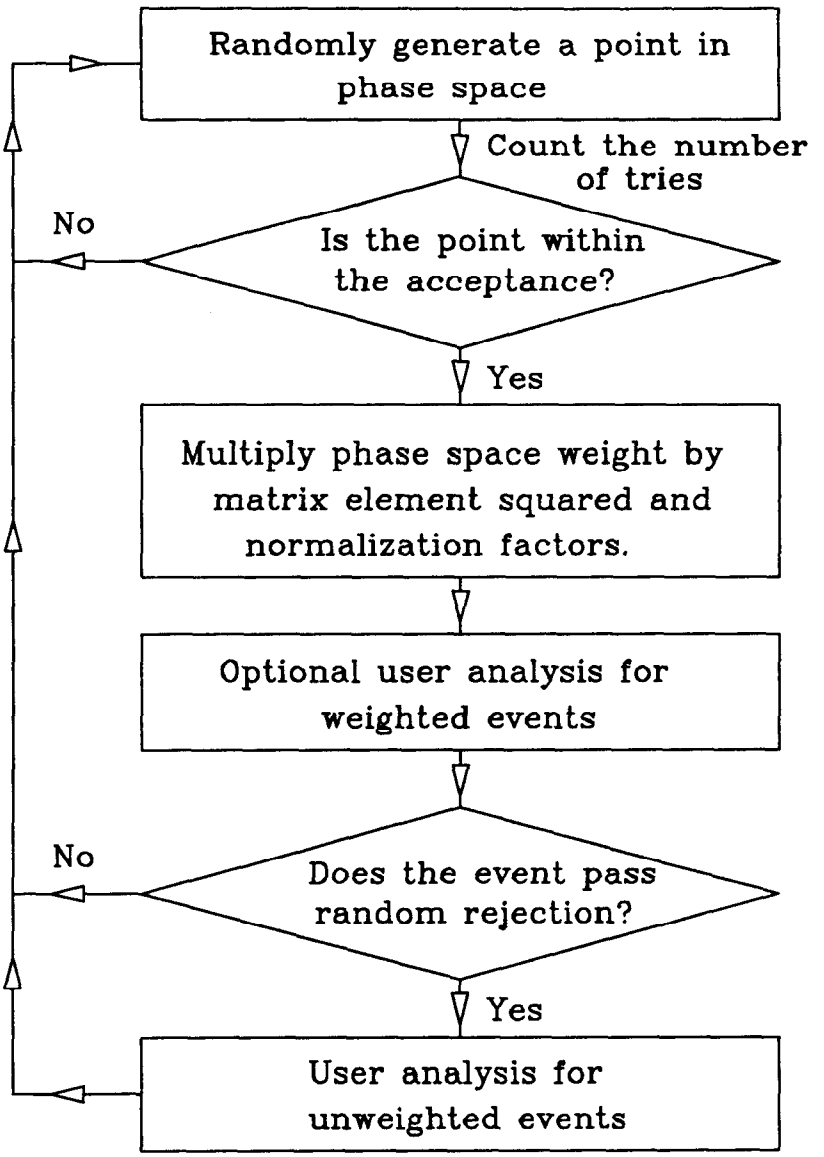

Figure 3.1. Schematic of the Monte Carlo procedure.

etc.) for these events may not correspond to the differential cross section, but the weighted distributions do. It is sometimes necessary to have a set of unweighted events (*i.e.* all events with the same weight) that do have occupancy distributions that correspond to the differential cross section. This set of unweighted events is obtained from the set of weighted events by a simple random rejection algorithm. If the total event weight is greater than a random number (between 0 and 1) times the estimated maximum weight, then the event is kept as an unweighted event. Otherwise, the event is discarded and a new event is generated.

The cross section corresponding to a subset of these unweighted events (the subset chosen by tighter cuts, detector simulation, etc.) is simply

$$\sigma_{sub} = N_{sub} * \sigma_{total}/N_{gen} \tag{3.6}$$

where N_{sub} is the number of events in the subset, N_{gen} is the number of unweighted events and σ_{total} is the total cross section as in equation 3.4. From this equation, one can identify the luminosity of the Monte Carlo generation.

$$\begin{aligned} \sigma_{sub} &= N_{sub}/L_{gen} \\ L_{gen} &= N_{gen}/\sigma_{total} \end{aligned} \tag{3.7}$$

Unfortunately, the fractional uncertainty in the cross section always increases when going to unweighted events, but a lengthy analysis or detector simulation procedure requires using unweighted events. Performing detector simulation on a large number of small weight events which do not contribute significantly to the cross section is wasteful of CPU time.

The key to making an efficient Monte Carlo program is to sample phase space more often in the regions where the differential cross section is large. This is done by a suitable change of variables in the phase space volume element, and is called *Importance Sampling*[13,14]. In such a biased sampling, the phase space weight is reduced for those events in the preferred sampling regions, and is increased in the less sampled regions. Since the total event weight is the product of $|M|^2$ and the phase space weight, the total weight is reduced in the region of the poles. This means the maximum weight is reduced and the integral converges faster (smaller standard deviation for the distribution of weights) and the unweighted event generation becomes more efficient. The average weight, which is also the total cross section, does not change.

The appropriate change of variables is found by using the inversion method. If $F(x)$ is a simple function that approximates $|M|^2$, and r is a random number between

0 and 1, then

$$r = \frac{\int_{x_{min}}^{x} F(y)dy}{\int_{x_{min}}^{x_{max}} F(y)dy} \tag{3.8}$$

Once this integral has been evaluated, one simply solves for x as a function of the variable r (x_{min} and x_{max} are parameters), and then finds the differential $dx = \cdots dr$ necessary to make the change of variables from x to r. A flat distribution of r values between 0 and 1 then generates a distribution in x between x_{min} and x_{max} that follows the form of $F(x)$. (Functions that produce pseudo random numbers between 0 and 1 are commonly available on most computer systems.)

As an example, consider $|M|^2 = 1/x^2$, with $x_{min} = 0.01$ and $x_{max} = 1$, and let the phase space volume element be simply dx.

$$I = \int_{.01}^{1.} \frac{dx}{x^2} \tag{3.9}$$

If x is generated without importance sampling (just a flat distribution between 0.0 and 1, where x values below 0.01 are discarded but counted as tries) then the maximum weight is $1./0.01^2 = 10000$. The efficiency of the unweighted event generation is N_{gen}/N_{try}, which is 1%. However, if $1./x^2$ is inverted, then

$$x = \frac{x_{min}x_{max}}{x_{max} - (x_{max} - x_{min})r} \tag{3.10}$$

$$dx = x^2 \left(\frac{x_{max} - x_{min}}{x_{max}x_{min}} \right) dr \tag{3.11}$$

and the efficiency becomes 100%. Note that the total weight for each event is the generated weight, $1/x^2$, times the transformation of variables factor given in equation 3.11. The transformation given in equation 3.10 preferentially samples small values of x, and the event weight is reduced at these values.

Generally, the integrand is not a simple function that can be inverted easily. One must find an invertible function that approximates the integrand, particularly near the poles.

Importance sampling in multidimensional phase space can be quite difficult. For the 2-body phase space shown in equation 3.3, it is relatively simple to do importance sampling. $d\Omega$ reduces to $d\phi \cdot d\cos(\theta)$ in the CMS frame, so one can easily do importance sampling based on $\cos(\theta)$. It may be necessary to rotate the frame of reference so that θ is relative to an initial state vector boosted into the 2-body decay frame. For three or more body phase space, there are a number of approaches one may take to generating phase space. In the simplest case, one first rewrites d^3p_1 in terms of variables that one wishes to use for sampling, such as

$$d^3p_1 = p_1^2 dp_1 d\phi_1 d\cos(\theta_1) \tag{3.12}$$

or

$$d^3p_1 = -\frac{p_1 dm_{1j}^2 dp_1 d\phi_1}{2p_j} \tag{3.13}$$

(where $m_{1j}^2 = (p_1 + p_j)^2$) or any other set of useful variables. One then generates all variables for particle 1. At this point it is generally easier to work in the CMS frame of the remaining system and keep generating particles until only the two particles are left, at which point the 2-body phase space is used. This procedure is shown schematically in Figure 3.2 and described in more detail in references 13 and 14.

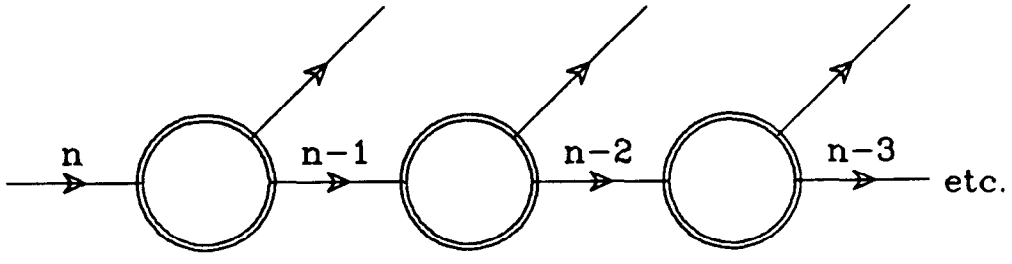

Figure 3.2. Serial two particle break-up scheme. This diagram indicates the flow of logic in the two particle break-up scheme, and is not a Feynman diagram. Lines indicate a single or a group of particles, and circles indicate the logic which generates the 4-vectors of the outgoing lines.

A useful relation in generating multi-particle phase space relates phase space for n-particles to the phase space for n-1 particles by treating particles 1 and 2 as a single system of momentum $p_{12} = p_1 + p_2$ and mass squared $m_{12}^2 = p_{12}^2$. This relation is

$$d\Phi_n(P; p_1, \cdots, p_n) = d\Phi_{n-1}(P; p_{12}, p_3, \cdots, p_n) \times d\Phi_2(p_{12}; p_1, p_2)(2\pi)^3 dm_{1,2}^2 \quad (3.14)$$

Naturally, one is not restricted to using an single system of only 2 particles. For example, if $n = n_1 + n_2$, with $n_1, n_2 \geq 1$, then

$$d\Phi_n = d\Phi_{n_1} d\Phi_{n_2} dm_{n_1,n_2}^2 \quad (3.15)$$

This is shown schematically in Figure 3.3. Whether or not each subsystem is broken up further in this manner depends on what type of importance sampling is required. The $e^+e^- \to e^+e^-\gamma\gamma$ Monte Carlo described in a later section demonstrates how this procedure is used in practice.

3.2 The Multi-Pole Problem

The importance sampling technique works if one has an invertible function which approximates all the major peaking behaviors of the integrand. However, if even one major peak is left out, the efficiency of the generation actually becomes worse than not using any importance sampling at all!

As an example, take the case of an integrand equaling $1/x^2 + 1/(x-1)^2$ and limits of integration $x_{min} = 0.01, x_{max} = 0.99$. If x is generated uniformly from x_{min} to x_{max} as $x = (x_{max} - x_{min})r + x_{min}$, then the transformation of variables contribution to the weight is always 0.98. The maximum total weight occurs at $x = 0.01$ and 0.99, and is simply 9801. If x is importance sampled according to the $1/x^2$ distribution, then the maximum weight occurs at $x = 0.99$. The total weight at this point is 970299, almost ten times larger than the maximum weight using no importance sampling at all.

Of course, if one set x_{max} well away from the pole at $x = 1$, then importance sampling based on $1/x^2$ would have given a good efficiency. The problem occurs only if one is sampling phase space near more than one pole in a single variable.

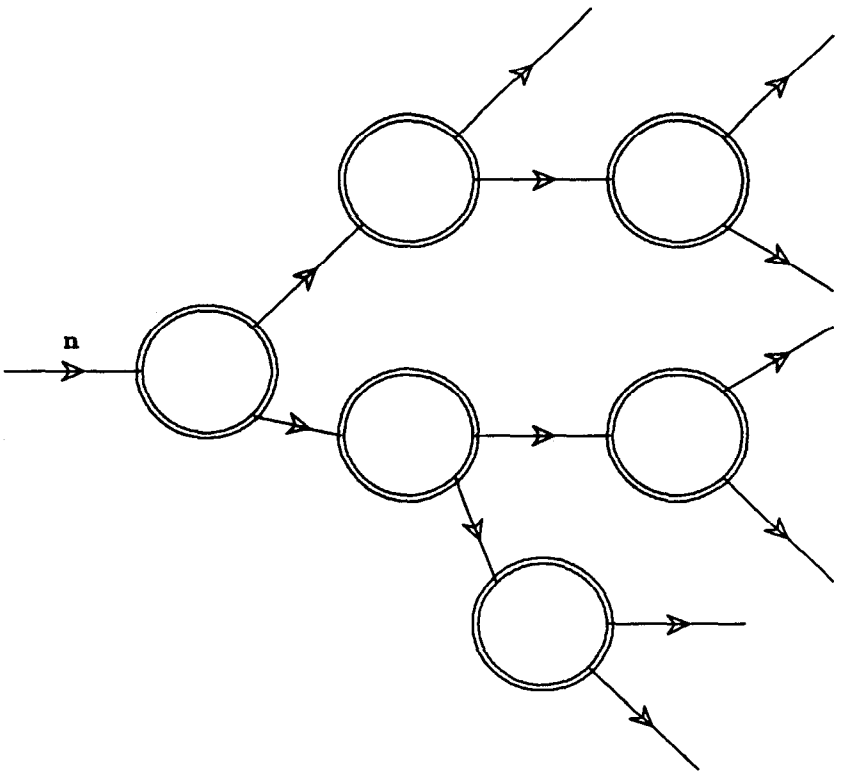

Figure 3.3. Tree-like two particle break-up scheme. This diagram indicates the flow of logic in the two particle break-up scheme, and is not a Feynman diagram. Lines indicate a single or a group of particles, and circles indicate the logic which generates the 4-vectors of the outgoing lines.

An example of a physics problem is Bremsstrahlung radiation in e^+e^- collisions. For a given photon energy, there is a QED pole for the photon to be colinear with any of the initial or final state charged particles. If one does importance sampling for the photon direction based solely on radiation from an initial state particle, but the photon coincidentally lines up with one of the final state charged particles, then the total event weight becomes very large, and the efficiency of the Monte Carlo gets small. However, if one is only interested in initial state radiation of photons and restricts the photon angle to be near the beam line with all other final state charged particles well away from the beam line, then sampling based only on the initial state radiation pole is efficient. It is the general case, where the photon is unrestricted, that is difficult. This is the situation for the $e^+e^- \rightarrow e^+e^-\gamma\gamma$ Monte Carlo program described later.

3.3 A Multi-Pole Solution

A solution to the multi-pole problem is to superpose importance sampling distributions (one for each pole) and symmetrize a generated event with respect to all of these distributions. If the function $F_i(\vec{p}_1, \vec{p}_2, \cdots, \vec{p}_n)$ represents an invertible function that approximates a pole, then the total integral can be rewritten as follows.

$$\begin{aligned}
\sigma &= \frac{(2\pi)^4}{2s} \int |M|^2 d\Phi_n \\
&= \frac{(2\pi)^4}{2s} \int |M|^2 \left(\frac{a_1 F_1(\cdots) + a_2 F_2(\cdots) + \cdots + a_N F_N}{a_1 F_1(\cdots) + a_2 F_2(\cdots) + \cdots + a_N F_N} \right) d\Phi_n \\
&= \frac{(2\pi)^4}{2s} \left(\int \frac{|M|^2 a_1 F_1}{\sum_{j=1}^N a_j F_j} d\Phi_n + \int \frac{|M|^2 a_2 F_2}{\sum_{j=1}^N a_j F_j} d\Phi_n + \cdots + \int \frac{|M|^2 a_N F_N}{\sum_{j=1}^N a_j F_j} d\Phi_n \right) \\
&= \frac{(2\pi)^4}{2s} \sum_{i=1}^N \int \frac{|M|^2 a_i F_i}{\sum_{j=1}^N a_j F_j} d\Phi_n
\end{aligned} \tag{3.16}$$

where N is the number of functions F to be used and the parameters 'a' are simple relative weight factors. Each integral 'i' is evaluated using importance sampling based solely on the function F_i in the numerator, and the results combined in a way transparent to the user of the Monte Carlo program.

The Monte Carlo procedure in this framework is as follows:

1. An integral 'i' is selected with a probability P_i. The probability P_i is provided by the user and is normalized ($\sum_{i=1}^N P_i = 1$).
2. The four-vectors for all particles are generated with importance sampling based on F_i, and a phase space weight is obtained.
3. The phase space weight is then multiplied by $a_i F_i$ and divided by $\sum_{j=1}^N a_j F_j$.
4. The phase space weight is divided by P_i, and the set of four-vectors and the phase space weight are returned to the calling program.

The calling program then evaluates $|M|^2$ and performs the Monte Carlo integration in the usual way.

The power of this technique is primarily in step 3. The selection of an integral 'i' with importance sampling F_i allows one to preferentially sample all poles in the matrix

element. Essentially, the superposition of the functions F ($\sum_{j=1}^{N} a_j F_j$) approximates $|M|^2$. The problem of coincidentally generating a point in phase space near the pole described by F_k when doing importance sampling based on F_i is solved by the division by $\sum_{j=1}^{N} a_j F_j$ in step 3, which symmetrizes the generation with respect to all poles. F_k is large for phase space points near the pole it describes, thus the phase space weight is greatly reduced by the division.

Dividing the result by P_i in step 4 normalizes all the integrals 'i' so that the calling program does not need to know which function F_i was used to generate phase space. Of course, it is best to keep track of the maximum total weight corresponding to generation according to each function F_i so that the user can better adjust the parameters P_i, a_i and possibly the function F_i in order to obtain maximum efficiency. This procedure of dividing by P_i only works if all integrals 'i' are sampled with high statistics, such that $P_i = n_i/n_{total}$, where n_i is the number of times integral 'i' is selected and n_{total} is the number of times all integrals are selected. Essentially, all integrals 'i' are being evaluated separately, and one should normally add up the result of all integrals at the end of the Monte Carlo program. The Monte Carlo integral is simply the average weight and can be expressed in the following manner:

$$\begin{aligned}
\langle W_{tot} \rangle &= \langle W_1 \rangle + \langle W_2 \rangle + \cdots + \langle W_N \rangle \\
\frac{\sum w}{n_{total}} &= \frac{\sum w_1}{n_1} + \frac{\sum w_2}{n_2} + \cdots + \frac{\sum w_N}{n_N} \\
&= \frac{1}{n_{total}} \left(\frac{n_{total} \sum w_1}{n_1} + \frac{n_{total} \sum w_2}{n_2} + \cdots + \frac{n_{total} \sum w_N}{n_N} \right) \\
&= \frac{1}{n_{total}} \left(\frac{\sum w_1}{P_1} + \frac{\sum w_2}{P_2} + \cdots + \frac{\sum w_N}{P_N} \right) \\
&= \frac{1}{n_{total}} \sum \left(\frac{w_1}{P_1} + \frac{w_2}{P_2} + \cdots + \frac{w_N}{P_N} \right)
\end{aligned} \tag{3.17}$$

Hence, by dividing the individual weights by P_i, one can ignore which term 'i' was used to do the importance sampling. This procedure of dividing by P_i rather than n_i/n_{total} does introduce some extra statistical error into the Monte Carlo process, but the standard calculation of the Monte Carlo uncertainty in equation 3.5 accounts for it.

This Monte Carlo procedure can be used to solve the simple example problem given in the previous section. The integral $\int_{0.01}^{0.99}(1/x^2+1/(1-x)^2)dx$ is to be evaluated. Let $a_1F_1 = 1/x^2$, $a_2F_2 = 1/(1-x)^2$ and $P_1 = P_2 = 0.5$. The total weight when generating based on F_1 is simply

$$w = \left(\frac{1}{x^2} + \frac{1}{(1-x)^2}\right) \cdot \frac{a_1F_1(x)}{a_1F_1(x) + a_2F_2(x)} \cdot \left(\frac{dx}{dr}\right) \cdot \frac{1}{P_1} \tag{3.18}$$

with

$$\begin{aligned} x &= \frac{x_{min}x_{max}}{x_{max} - (x_{max} - x_{min})r} \\ \frac{dx}{dr} &= x^2\frac{(x_{max} - x_{min})}{x_{min}x_{max}} \end{aligned} \tag{3.19}$$

which yields

$$\begin{aligned} w &= 2 \cdot \left(\frac{1}{x^2} + \frac{1}{(1-x)^2}\right) \cdot \left(\frac{\frac{1}{x^2}}{\frac{1}{x^2} + \frac{1}{(1-x)^2}}\right) \cdot x^2\frac{(x_{max} - x_{min})}{x_{min}x_{max}} \\ &= 2 \cdot \frac{(x_{max} - x_{min})}{x_{min}x_{max}} \\ &= 197.98 \end{aligned} \tag{3.20}$$

The weight is a constant independent of x. This is also true for sampling with respect to F_2, and thus the Monte Carlo is now 100% efficient.

Another way to view the power of this procedure is to rewrite the cross section as

$$\begin{aligned} \sigma &= \frac{(2\pi)^4}{2s}\sum_{i=1}^{N}\int\left(\frac{|M|^2}{\sum_{j=1}^{N}a_jF_j}\right)a_iF_i d\Phi_n \\ &= \frac{(2\pi)^4}{2s}\sum_{i=1}^{N}\int\left(\frac{|M|^2G}{\sum_{j=1}^{N}a_jF_j}\right)a_iF_i d\alpha_n\delta^4(\cdots) \end{aligned} \tag{3.21}$$

where $d\Phi_n = Gd\alpha_n$ and $d\alpha_n$ is the differential element in terms of the kinematic variables used in the functions F. For example, if F_2 is a function of $|\vec{p}|$, $\cos(\theta)$ and ϕ and

$$d\Phi = \frac{d^3p}{(2\pi)^3 2E}dpd\Omega \tag{3.22}$$

then

$$G = \frac{p^2}{(2\pi)^3 2E}$$
$$d\alpha = dpd\Omega \tag{3.23}$$

In the limit that $\sum_{i=1}^{N} a_i F_i = |M|^2 G$ the cross section becomes

$$\sigma = \frac{(2\pi)^4}{2s} \sum_{i=1}^{N} \int a_i F_i \delta^4(\cdots) d\alpha_n \tag{3.24}$$

Since each F_i was chosen to be invertible, each integral 'i' is evaluated with an efficiency approaching 100%. The efficiency is hampered only by the constraints imposed by the δ function. The δ function problem can be partially cured by simply generating kinematic variables only within the range allowed by the δ function. In other words, the phase space generator subroutine should recompute the limits for each kinematic variable based on the values of any previously generated kinematic variables. These limits should then be used when generating the variable, so that the δ function is satisfied. If the kinematic variables are also generated only within the user specified acceptance cuts, and all the probabilities P_i are equal (*i.e.* $P_i = 1/N$), then the efficiency will approach 100%. In practice, $\sum_{i=1}^{N} a_i F_i$ only approximates $|M|^2 G$, and it is not always possible to generate only within the user's acceptance cuts, so it is often necessary to adjust the probabilities P_i in order to obtain maximum efficiency.

3.4 The $ee\gamma\gamma$ Generator

The process $e^+e^- \rightarrow e^+e^-\gamma\gamma$, where phase space is sampled near all poles, is a good example of a multi-pole problem. It has the usual poles for Bremsstrahlung production of photons — poles occur for low energy photons (1/k distribution), very high energy photons and low invariant mass between any $e^{\pm}\gamma$ pair (both initial and final state $e^{\pm}$). It also has a pole for small values of t or s in the e^+e^- scatter. While these poles are easily described qualitatively, the problem is greatly aggravated by the large number of Feynman diagrams involved. The forty diagrams are shown

in Figure 3.4. Each diagram has four combinations of soft/hard photon energy poles, two poles corresponding to low invariant mass between the $e^{\pm}\gamma$ pairs and one pole for the small t or s channel e^+e^- scatter. Thus there are five poles represented in each of the forty diagrams and four combinations of soft/hard photon poles. This is truly a multi-pole problem.

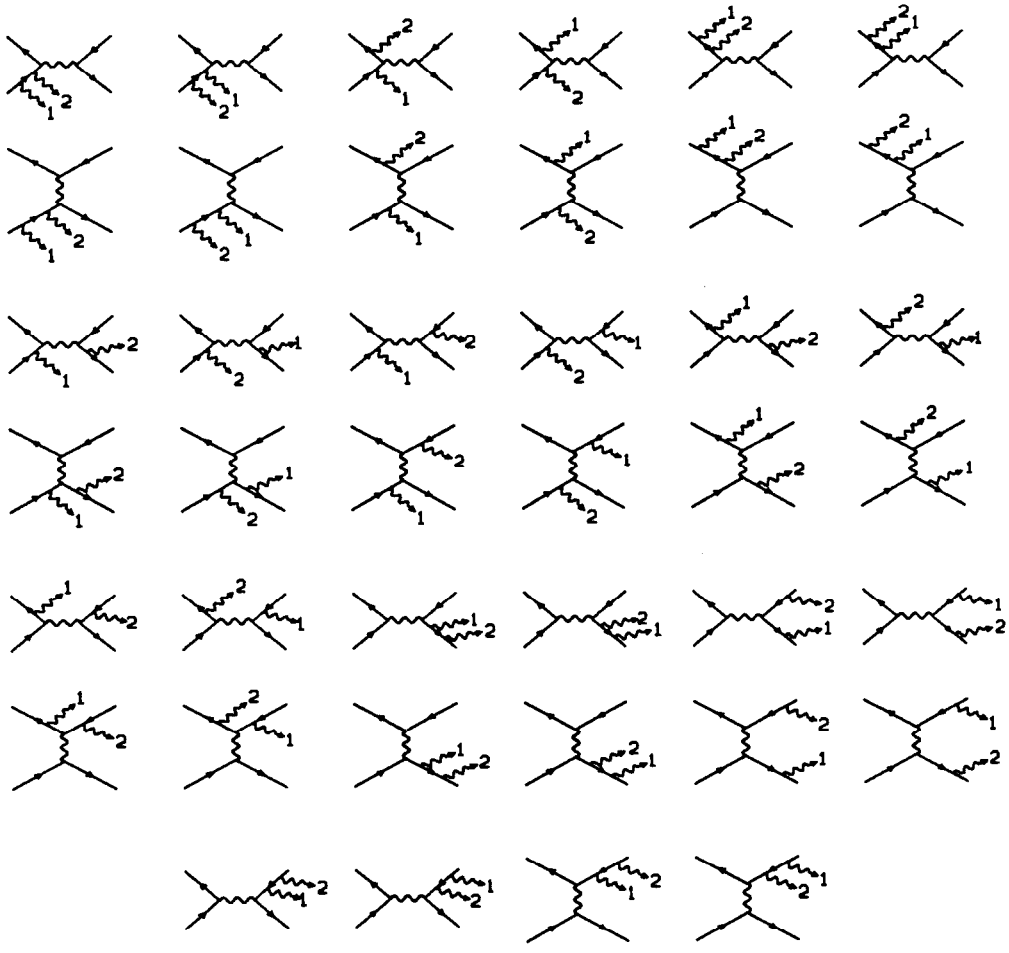

Figure 3.4. All $e^+e^- \rightarrow e^+e^-\gamma\gamma$ Feynman diagrams.

The forty diagrams can be split into six basic topologies, as shown in Figure 3.5. Note that s channel diagrams are now ignored because the t channel dominates. The remaining twenty diagrams can be represented as permutations of charges and indices. This is permitted because the matrix element is symmetric with respect to the charges.

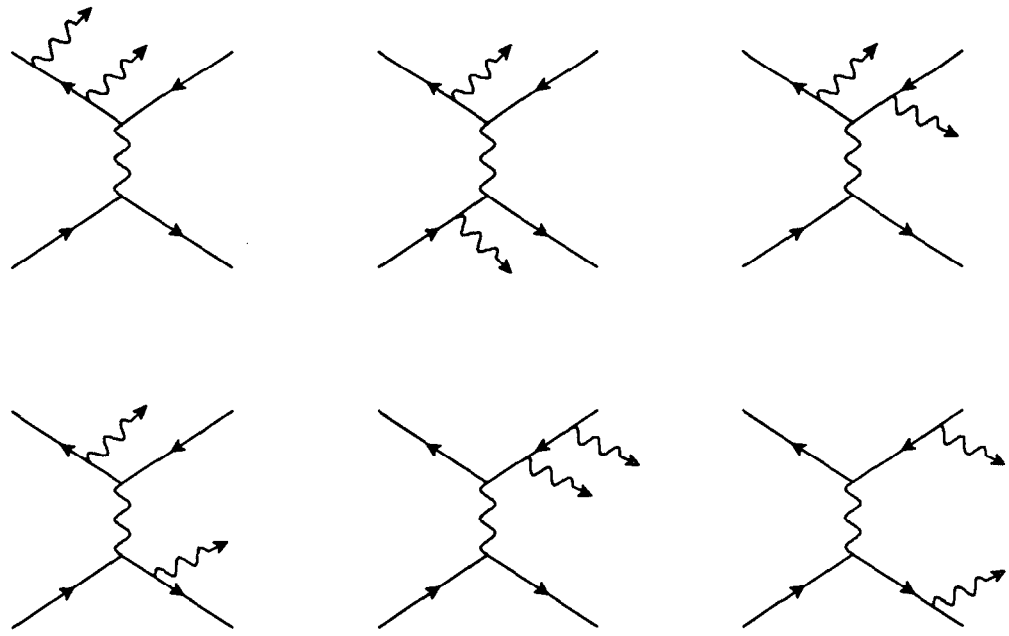

Figure 3.5. Six basic $e^+e^- \rightarrow e^+e^-\gamma\gamma$ diagrams.

In order to use the procedure given in the previous section, it is necessary to determine the functions F used to approximate the integrand. Berends *et al.*[12] used a similar procedure in their $e^+e^- \rightarrow e^+e^-e^+e^-$ Monte Carlo program. They determined their analog of the F functions by breaking up the set of Feynman diagrams into smaller gauge invariant subsets and calculating these subsets explicitly. Performing explicit calculations of α^4 diagrams is beyond the scope of this thesis. Instead, approximate functions are used in which the peaking variables are treated independently (except, of course, for the limits of integration). The matrix element for this process is very complicated, and it is difficult to simply read off an approximate functional behavior. The approximate form was found by supplying a simple set of four-vectors to the routine which calculates $|M|^2$. This simple set of four-vectors consisted of back-to-back e^+e^- and back-to-back photons. The angles and energies were varied, and functions fitted to the results to get simple, invertible approximate functions.

As an example, consider the second diagram in Figure 3.5, corresponding to double initial state radiation from opposite electron legs. This is explicitly shown in

Figure 3.6 with appropriate notation for a single permutation of photon indices. The approximate functional forms used for this diagram are

$$\begin{aligned}
&\frac{a_2 b_s b_s}{k_1 k_2 (w_1^2 - m_e^2)(w_2^2 - m_e^2)(-t + \epsilon_t)^2} \\
&\frac{a_2 b_s b_h}{k_1 (\zeta E_{beam} - k_2)(w_1^2 - m_e^2)(w_2^2 - m_e^2)(-t + \epsilon_t)^2} \\
&\frac{a_2 b_h b_s}{(\zeta E_{beam} - k_1) k_2 (w_1^2 - m_e^2)(w_2^2 - m_e^2)(-t + \epsilon_t)^2} \\
&\frac{a_2 b_h b_h}{(\zeta E_{beam} - k_1)(\zeta E_{beam} - k_2)(w_1^2 - m_e^2)(w_2^2 - m_e^2)(-t + \epsilon_t)^2}
\end{aligned} \tag{3.25}$$

where a_2 is a weighting parameter for this event topology, b_s and b_h are weighting parameters for soft and hard photon energy poles, and ζ and ϵ_t are parameters used to increase the efficiency. The terms $(w_1^2 - m_e^2)$ and $(w_2^2 - m_e^2)$ in the denominator represent the electron propagators, and $1/t^2$ is the e^+e^- scattering behavior.

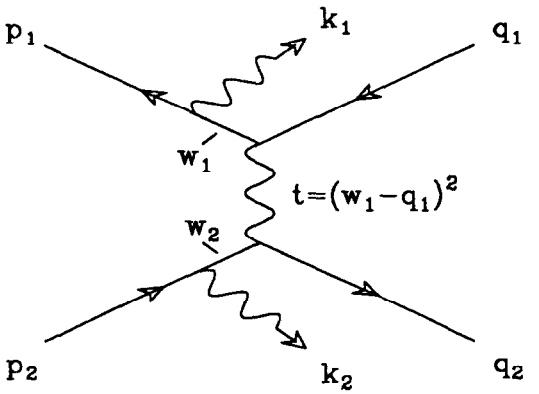

Figure 3.6. Double initial state Bremsstrahlung, opposite legs.

When topology 2 and one of the soft/hard photon combinations are selected, the event is generated in the following manner:

1. The propagator value $(w_1^2 - m_e^2)$ is generated. The limits are determined from the absolute kinematic limits and from user specified limits on photon angles and energies.
2. The propagator value $(w_2^2 - m_e^2)$ is generated. The limits are determined as in 1, with the exception being that the kinematic limits are modified by the value of the propagator generated in step 1.

3. The photon energies are generated.
4. The e^+e^- scatter is generated in the w_1w_2 CMS frame and the results boosted back to the lab frame.

The phase space weight is modified at each step. The weight is then symmetrized with respect to all other poles (as described in the previous section) and divided by the probability to select this topology and photon pole combination. Thus a final phase space weight and a set of four-vectors are returned to the calling routine, which then calculates $|M|^2$ and performs the integration. The calling routine also divides the result by $N_\gamma! = 2$. This is a statistical factor used because both photons are bosons and both photons are integrated over all phase space. It is possible for the phase space generator to produce the same set of four-vectors, except with the photon indices interchanged. This has already been taken into account by the full set of Feynman diagrams, in which all diagrams come in pairs — the only difference between the diagrams in the pair being that the photon indices are swapped.

All other topologies are handled similarly. Topology type 1 (double initial state radiation off the same leg) is the primary exception. This topology, shown explicitly in Figure 3.7, has the complication that the second photon, k_2, can't be generated through this diagram into all the phase space available to the full set of diagrams. More explicitly, if w_1^2 becomes negative after the generation of k_1, then kinematics restricts the angle of k_2 from being colinear with the direction of w_1. However, if the topology was one initial state radiated photon and one final state radiated photon, the final state photon is kinematically allowed in the region of phase space prohibited by topology type 1. Topology type 1 is the only one that has this difficulty. Since the experimental acceptance cuts used in this thesis allow only one particle below 20° on each side of the detector, this topology has only a small contribution to the accepted cross section, and is therefore dropped from the importance sampling in the phase space generator.

The only other significant difference in how topologies are generated involves final state photon radiation. The user is allowed to specify a minimum opening angle between the photon and the electron in the lab frame. This constraint often disallows

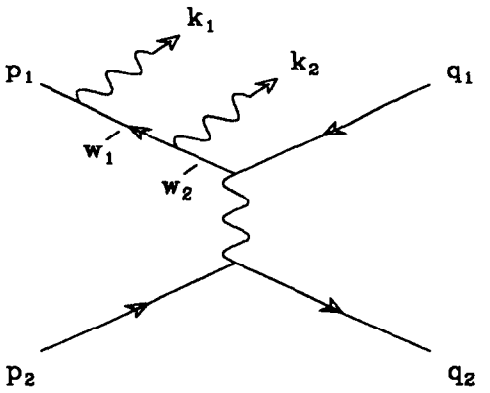

Figure 3.7. Double initial state Bremsstrahlung, same leg.

a range of energies in the middle of the spectrum, but does allow hard and soft photon energies. These energy limits are determined as each event is generated, and photon energies are only generated within the allowed regions, thereby increasing the efficiency of the program.

During the generation process, the four-vectors generated so far are checked against the user specified acceptance cuts. Checking these cuts at intermediate stages, rather than after all four-vectors are generated, saves considerable computer time. If any cut is failed, the program goes back to the top of the phase space generation loop, and a new topology and soft/hard photon combination are selected. Each failure is still counted as a '*try*' with zero weight for integration purposes.

The program is written in FORTRAN 77 and runs on the IBM 3081 at SLAC. The implementation of the four-vector generation portion of the phase space generator was relatively straight forward to program, though lengthy. The primary difficulties involve the calculation of kinematic limits at intermediate stages. The symmetrization of the phase space generator and the calculation of the matrix element make extensive use of nested FORTRAN statement function definitions. This simplifies coding calculations that differ only by a permutation of indices.

Both the matrix element calculation and the phase space generator were tested for accuracy. The routine that calculates $|M|^2$ compares well numerically with a similar routine coded by Kiyotomo Kawagoe[15], which is based on the same published matrix element of Berends *et al.* used in this thesis. The total accepted cross section using

the multi-pole phase space generation technique agrees to less than 1% with the same integration using the uniform phase space generator RAMBO [16].

The performance of this $e^+e^- \to e^+e^-\gamma\gamma$ generator is best shown by the number of unweighted events in a given amount of CPU time. The kinematic cuts used for the generation are:

1. At least 2 particles between 15° and 165° θ_p. Tracks in this central region must have energy $\geq$ 150 MeV and must be acolinear with respect to all other central particles by at least 5°.
2. No more than one particle in the region defined by $\theta > 2.5°$ and $\theta_p < 15°$ (similarly for $\theta < 177.5°$ and $\theta_p > 165°$). Particles in the region must have energy $\geq$ 2 GeV.
3. All particle pair combinations must have an invariant mass > 200 MeV.

When using the uniform phase space generator RAMBO, less than one unweighted event is produced in two CPU hours. When using the program described in this section, approximately 720 unweighted events are produced in two CPU hours. The parameters used for generation were chosen based on a few test jobs, but are not necessarily the most optimal values. However, the rate of event production is sufficient in relation to the available CPU time at SLAC.

3.5 The $\gamma\gamma\gamma\gamma$ Generator

The generation of 4γ events is a much simpler problem than the $e^+e^-\gamma\gamma$ case, but it still requires the application of the multi-pole technique described in this chapter. There are 24 diagrams for the process $e^+e^- \to \gamma\gamma\gamma\gamma$, but they only differ by a permutation of indices.

The algorithms used in this program are more primitive than those used for the $e^+e^-\gamma\gamma$ program (the 4γ program was written well before the $e^+e^-\gamma\gamma$ program), but it is sufficient for obtaining a QED prediction. The first three photons are produced with a 1/k energy distribution. The first two photons are produced with a $1/(1+\epsilon-\cos^2\theta)$ distribution in the lab frame. A better angular distribution is $1/(1+\epsilon-\cos\theta)$, but the former function automatically produces forward and backward scattering with

equal weight relative to either beam direction, thus simplifying the algorithm. The resulting four-vectors are then symmetrized before returning to the main routine. The main routine performs the rest of the integration procedure. It includes a division by $N_\gamma! = 4!$, as described in the previous section.

4

Tracking and Event Selection

The event selection proceeded in multiple stages. There were $\approx$ 31 million triggered events recorded to tape. These were first reduced to $\approx$ 12.5 million events by the ASP production filter, which tracked the events and discarded those identified as not originating near the beam interaction point. The filters specific to this analysis were then run on this reduced set of events.

The event selection philosophy used in all filter jobs is that all cuts should be efficient for four-body QED final states. Backgrounds are eliminated by adding cuts that reject on characteristics specific for the background, but which are efficient for good signal events. In some cases, acceptance cuts are defined so that problem areas of the detector are simply avoided. By having a large number of loose, efficient cuts rather than a smaller number of tight, less efficient cuts, uncertainties in the Monte Carlo prediction for signal events can be minimized.

4.1 Tracking Procedure

The ASP tracking system is shown schematically in Figure 4.1. Before the tracking driver routine ASPTRK is called, all appropriate data has been unpacked and corrected by run dependent calibration factors. ASPTRK first calls the tracking routines for the individual detector subsystems. It then calls the routine TRKTOP (TRacK TOPology) which puts subsystem track segments together to make a final set of global tracks. Finally, ASPTRK calls the routine TRKFIL, which recomputes

the track energies and fills the common TRKLST with the fitting information for all tracks and unused subsystem segments.

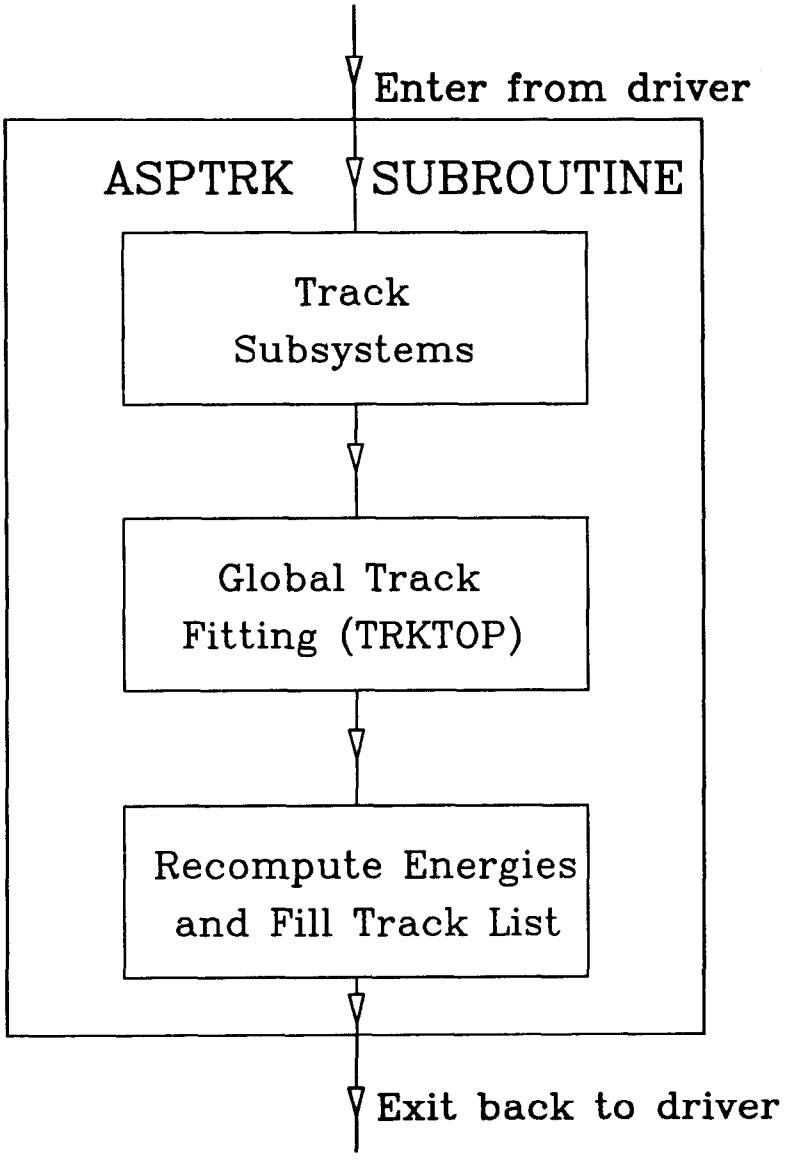

Figure 4.1. Schematic of the ASP tracking procedure.

The subsystem tracking routines find hit clusters and perform least squares fits. The results of the fits are stored as vectors (two intercepts, two slopes and a direction pointer) with associated error matrices in the common block SGMTCM. This common block also stores other information about the fit, such as the fit projection (*i.e.* the specification of the independent axis that defines the slopes and intercepts of the fitted

vector), the χ^2 of the fit, the beam spot constrained fit angles and other information that may be useful in deciding which segments should be put together into tracks. Only the lead-glass, central PWC, central tracker, drift chamber and forward PWC subsystems are used at this level. The Time-of-Flight and veto scintillator systems are added after the global track fitting has been performed.

The forward system fits (drift chamber and forward PWC) are combined before they are entered into SGMTCM. Drift chamber hits are required to have corresponding forward PWC hits (as seen from the interaction point) in order to be entered as a fitted segment. Forward PWC points of sufficient quality are entered as segments without the need of a corresponding drift chamber hit. (Sufficient quality is defined as a point having measurements of both X and Y and a total signal which corresponds to $\approx$ 1 GeV or more of track energy.)

The central PWC system and lead-glass system suffer from an ambiguity problem when there are multiple clusters in either system in the same quadrant. For example, if two photons enter the same quadrant, there are two clusters in each system. There is no way to tell which PWC cluster belongs to which lead-glass cluster just from the fitted vectors. If one or more of the incoming particles is charged, then the central tracker system can resolve the ambiguity, but only if the central tracker track is of good quality and the two particles are well separated. The ambiguity is resolved using the PWC and lead-glass systems alone by forming a χ^2 for each combination of PWC/lead-glass clusters. This χ^2 is based on layer signal deposition patterns in each cluster. A link is indicated in the SGMTCM common for those combinations that show an unambiguous match. Even if the match is not unambiguous, the χ^2 for each match is passed on to the global track fitting routine.

The global track fitting is performed by the subroutine TRKTOP. It starts by looking at high quality central tracker segments, called pivot segments. The central tracker is chosen first because it measures all three coordinates of a hit, rather than just two coordinates as other subsystems do. The pivot segments are then checked against the whole segment list to find those combinations for which a match would be allowed, and the pivot segment and the target segment are fitted together to find

a χ^2 for the match. A candidate track is then formed from the pivot and those target segments which had a good fit with the pivot. The candidate track fit is obtained by fitting all segments together. If the χ^2 of the fit is too high, then the target segment which contributed the most to the χ^2 is dropped, and the candidate refitted. This is done until the track passes the χ^2 cut or only the pivot segment remains.

Once the central tracker pivots are all used, high quality lead-glass segments are used as pivots, followed by high quality forward segments. Once all of these are exhausted, unused lead-glass then unused central tracker segments are used as pivots.

The segments on a candidate track are fitted together using an analytic (not iterative) least squares method which uses the segments' fit vectors and error matrices. First, the segment vectors and error matrices are transformed so that they all have the same projection (*i.e.* independent axis). The segments are fit together using a method that minimizes the χ^2. The total χ^2 for a track is

$$\chi^2 = \sum_{i=1}^{n} \left((b_i - a)^T W_i (b_i - a) + \chi_i^2 \right) \tag{4.1}$$

where

a = fitted track vector $\qquad$ b_i = segment vector

W_i = segment error matrix $\qquad$ χ_i^2 = segment χ^2

n = number of segments

This is minimized by

$$\begin{aligned} \frac{d\chi^2}{da} &= -\sum_{i=1}^{n} W_i (b_i - a) = 0 \\ \left(\sum_{i=1}^{n} W_i \right) a &= \sum_{i=1}^{n} W_i b_i \\ a &= \left(\sum_{i=1}^{n} W_i \right)^{-1} \left(\sum_{i=1}^{n} W_i b_i \right) \end{aligned} \tag{4.2}$$

The fitted vector 'a' can be found using standard simultaneous linear equations methods. The error matrix for the fitted vector is simply $\sum W_i$. Interaction point

constrained fits are found by simply forcing the intercepts in the fit vector to correspond to the nominal interaction point.

A special fitting procedure is required when fitting two lead-glass segments that are in different but adjacent quadrants. Before all the segments on a candidate track are fitted together, pairs lead-glass segments are checked for compatibility. In order for a pair to be compatible, the segments must be in adjacent quadrants (not the same or opposite quadrants). An azimuth is determined for compatible pairs using an energy weighting function. Using this azimuth, the values of the polar angle and its uncertainty for each segment in the pair is calculated, and a χ^2 is formed based on the difference of the two polar angles relative to the calculated errors. The pair with the lowest χ^2 below a cut is fitted together as a single segment, which is then used on the candidate track. If no pair passes the χ^2 cut, then the lead-glass segment with the best χ^2 match to the candidate's pivot segment is used. In both cases, remaining lead-glass segments are dropped from the candidate.

After all tracks have been made, the routine TRKFIL is called. This routine directs the calculation of the track energies and fills the track list common block. The calculation of the energy must be done at this stage using the best fitted angles for each track since the attenuation and collection of light in the lead-glass bars depend on both the position and angle of the electromagnetic showers.

4.2 ASP Production Filter

The ASP production filter, called JUNKIT, is designed to keep any event that has characteristics of an e^+e^- collision occurring near the interaction point. Those events that are to be kept are then fully tracked, and both the raw signal data and track list data are logged to tape.

The JUNKIT cuts are described on the next page. The percentage of simulated $e^+e^-\gamma\gamma$ events surviving each cut are also shown.

Cut	Cut Description	Monte Carlo $e^+e^-\gamma\gamma$ Surviving (Percent)
1	Not a VSCOSMIC trigger	100.00
2	Event time as measured by the lead-glass must be within five sigma of the beam crossing time.	100.00
3	Anti-cosmic CPWC – If there is a CP track with $\geq$ four planes that has the characteristics of a minimum ionizing track, then the distance of closest approach to the beam line must be less than 20 cm.	99.90
4	Anti-cosmic Lead-glass – A lead-glass track identified as minimum ionizing must have a Z intercept (as seen in the XZ or YZ plane) less than 20 cm.	99.73
5	The event must have less than 80 hits in the central tracker	99.70
6	Require one or more good lead-glass clusters, defined as having at least two layers in the cluster, 200 signal counts ($\approx$ 60 MeV), Z intercept (Z_0) less than 0.5 meter and $Z_0 \sin\theta_p$ less than 0.3 meter. This requirement is made only if none of the conditions A-E (described below) are met.	99.93
A	Passes single photon filter routine SELCH0	
B	Two lead-glass clusters in adjacent quadrants that match in their Z coordinates (indicative of a track in the corner between quadrants)	
C	Forward shower counter energy greater than 5 GeV, one or more lead-glass clusters and no forward trigger	
D	Passes $e^+e^-\gamma$ filter routine SELGEE.	
E	At least one good central tracker track with a minimum X or Y intercept less than 8 cm.	
	If conditions 1, 3 and the following are passed, then the event is kept even though cuts 2, 4, 5 and 6 may be failed.	
F	Total signal in lead-glass greater than 10,000 counts ($\approx$ 3 GeV) with total signal in layers 3-5 greater than 1000 counts	
All	Percentage of events passed and logged to tape	99.80

Notice that the efficiency is very good for $e^+e^-\gamma\gamma$ events. Likewise, it is very good for $e^+e^-e^+e^-$ and $\gamma\gamma\gamma\gamma$ events.

4.3 Event Selection

4.3.1 First Level Filter

The first level filter (after the ASP production filter) consists of a series of loose acceptance and background cuts. This filter selects $\approx$ 425,000 events from the 12.5 million events logged out by the ASP production filter. It performs a series precise checks on the ASP tracking results, such as distinguishing good tracks from fake tracks caused by shower fluctuations in the calorimeters and recalculating particle identification and energy assignments. It selects events which are candidates for multiparticle final states.

The heart of the first level filter is a routine which determines the number of primary tracks in the event. Fake tracks can appear in the track list because of shower fluctuations which are reconstructed as separate tracks or because random fluctuations in position measurement of subsystem fit segments and/or detector noise cause the event to be reconstructed improperly. The philosophy of this routine is to attempt to fit each event to the hypothesis that it only contains energetic electrons and photons that are well separated from the beam line and each other.

All lead-glass tracks with energy $E > 50$ MeV are compared with the highest energy lead-glass track to see if they are within specific two-track opening angle cuts. These cuts are taken to be 15° in θ_p and 20° in ϕ. If a track is within this region, it is attached to the highest energy track. The sum of the highest energy track and all attached tracks is now called the primary track. If the highest energy track has a good measurement of ϕ, then this ϕ is used as the value for the primary, else ϕ is recomputed using either the secondary track's ϕ or the ϕ calculated from energy weighting if the two tracks are in adjacent lead-glass quadrants. Once all tracks are checked against the highest energy track, the process is done repeatedly with the next highest energy unattached track until all tracks have been used or until the specified maximum of lead-glass primary tracks has been reached. A total of six lead-glass primaries are allowed if there are no forward system primaries, five if there is one forward primary and four if there are two forward primaries. This method gathers up

tracks within the angle cuts irregardless of whether one of the tracks is real or fake. If all tracks on a primary are real, the primary track will generally fail the shower shape cuts applied at a later filter level.

Primary tracks in the forward system are found if there is a forward track with energy greater than 1 GeV. Only one primary is allowed in each of the $+Z$ or $-Z$ forward systems. All tracks in each forward system that are not attached to a lead-glass track are attached to the highest energy forward tracks, and the energy is recomputed. (Forward tracks may be attached to lead-glass tracks by the general ASP tracking procedure. If a lead-glass track is attached to a central primary and it has a forward track associated with it, then the forward track is also attached to the primary.)

The charge of primary tracks in the central system is determined using the first two layers of the central tracker. In order to be considered charged, there must be at least three CT hits in different planes within 15° in ϕ of the primary track, with at least one of those hits being in the first two CT layers. A track is considered neutral if it does not contain the first two layers. This criteria was chosen so as to minimize the photon identification inefficiency caused by photon conversion in the back three layers of the CT. Forward primaries are considered charged if a drift chamber hit is attached to the track or if there is a CT hit in the first two layers that is within 15° in ϕ. All charge assignments are checked by a hand scan of the final sample. (The final sample is selected by the last filter job, not the first level filter described here.)

The lead-glass system has the ability to distinguish minimum ionizing particles (such as muons) from showering particles (such as electrons and photons). In order to determine if a track is minimum ionizing, the signal for each lead-glass layer on the track is corrected for light attenuation and collection efficiency. A track is considered minimum ionizing if there are at least three layers with 50 signal counts (about 15 MeV) and no layers with more than 400 signal counts (about 120 MeV).

The acceptance criteria applied at the first level filter are much looser than the final criteria. The central region is defined as $\theta_p > 15°$, central primary tracks only need to have energy greater than 50 MeV, forward tracks only need 1 GeV of energy,

and no angular or transverse momentum cuts are applied to the forward tracks. At least four primary tracks are required, but there may be up to six primary tracks and up to two unused lead-glass tracks. The total event energy is only required to be 6 GeV, and no missing momentum cuts are applied. These cuts leave 425,000 events when applied to the ASP production sample.

4.3.2 The Second Level Filter

The second level filter further selects events by applying some of the final acceptance criteria and applying some shower shape cuts. The selection code for all classes first requires at least two central primaries passing the final energy and angular acceptance criteria. Central tracks are required to have $E > 0.3$ GeV, $\theta_p > 20°$, and a two-track opening angle of at least 15° in θ_p or 20° in ϕ. The remaining cuts differ somewhat for the $\gamma\gamma\gamma\gamma$ event class versus the $e^+e^-\gamma\gamma$ and $e^+e^-e^+e^-$ classes.

The $\gamma\gamma\gamma\gamma$ sample is selected by requiring that there be no more than 30 CT hits in the events and that there be no more than one charged track. This allows up to one of the photons to have converted in the beam pipe or the first two layers of the CT. The only other requirement at this stage is that there is at least 10 GeV of reconstructed energy in the event. No cuts on the forward tracks are made at this level. There are 3710 events remaining in this category at this stage.

The $e^+e^-\gamma\gamma$ and $e^+e^-e^+e^-$ classes are handled together in the filter program and are distinguished in the final hand scan. The selection criteria at this stage requires at least two charged tracks, less than six primaries plus unused lead-glass tracks, and at least 15 GeV of total event energy. Shower shape cuts for lead-glass primaries are also applied at this stage. The second moment of the shower width (lateral to the track direction) is computed for each lead-glass primary. The distribution of shower widths for kinematically fitted $e^+e^- \rightarrow e^+e^-\gamma$ events (with only one lead-glass track) is shown in Figure 4.2. No primaries may have a width larger than 0.0041 m^2. If there are one or two forward primaries, then at least two lead-glass primaries (one of which must be the highest energy primary) in the angular and energy acceptance region must have a width less than 0.0025 m^2. If there are no forward primaries, then

at least three lead-glass primaries must have a width less than 0.0025 m^2. There are 20166 events remaining in this category at this stage.

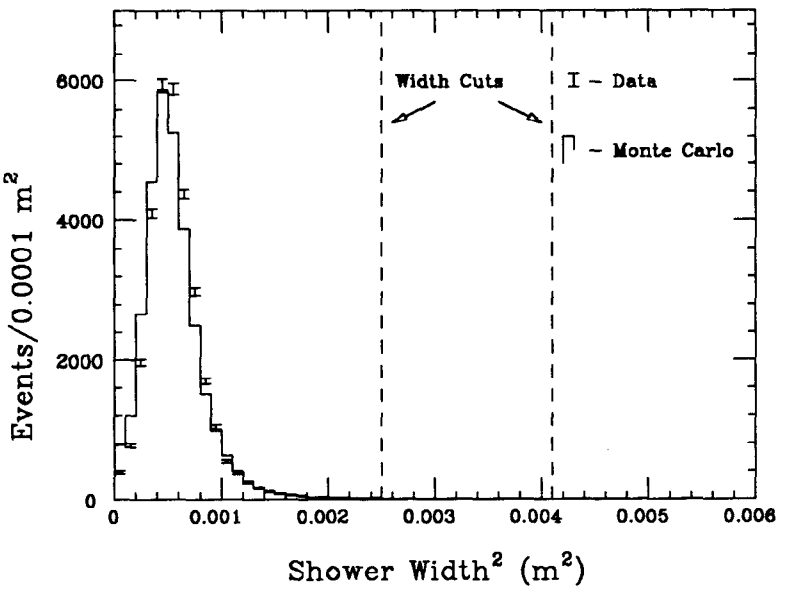

Figure 4.2. Shower widths of lead-glass tracks for $e^+e^- \rightarrow e^+e^-\gamma$ events.

4.3.3 The Third Level Filter

The third level filter is the final filter job. It applies the remaining final acceptance criteria as well as a few cuts designed to eliminate background events. It starts by retracking all events with tracking code optimized for events known to be coming from the beam interaction point. All events are then passed through the first and second level filters, followed by the extra cuts described below.

One cut which requires some explanation is based on the number of *distinct* lead-glass tracks. The lead-glass tracking system sometimes has difficulties reconstructing tracks in the overlap region between quadrants. Such tracks are generally reconstructed properly as a single track, but sometimes they are split into two. This introduces a large background from $e^+e^- \rightarrow e^+e^-\gamma$ and $e^+e^- \rightarrow \gamma\gamma\gamma$ events. To reduce this problem, the Z position of the cluster layers are compared. When a track enters an overlap region, it starts showering in the front quadrant (as seen from the interaction point) first, and the shower continues to develop into the back quadrant. The Z extent of the cluster in the last significant layer in the front quadrant is compared

with the Z extent of the first layer of the cluster in the back quadrant. The choice of clusters to be compared depends on the quality of the clusters' ϕ measurements. Back quadrant clusters must also have at least 60% of their signal in the first layer in order to be checked against a front quad cluster. The Z extent of the layer cluster is defined by the lead-glass bars that have at least 10% of the maximum bar signal in that layer. If the Z extent of the front and back quadrants overlap, then the two clusters are not considered to be *distinct*. The number of *distinct* lead-glass primaries is counted.

The selection code for the $\gamma\gamma\gamma\gamma$ class starts by applying the same shower width cuts used by the $e^+e^-\gamma\gamma$ and $e^+e^-e^+e^-$ classes described in the previous section. It also requires at least 15 GeV total energy, less than five primaries plus unused lead-glass tracks for events with no forward primaries, less than six primaries plus unused lead-glass tracks for events with forward primaries, at least two tracks with energy greater than 4 GeV, and at least $4 - N_f$ (where N_f is the number of forward primaries) *distinct* primaries. The final acceptance criteria for forward tracks is also applied. The acceptance for forward tracks is defined by $E > 4$ GeV, transverse momentum $p_t > 0.4$ GeV, and polar angle in the regions defined by $50 < \theta < 95$ mrad or $\theta > 120$ mrad and $\theta_p < 180$ mrad. Only one forward primary is allowed in each of the $+Z$ or $-Z$ forward systems.

The selection code for the $e^+e^-\gamma\gamma$ and $e^+e^-e^+e^-$ classes is basically the same as the $\gamma\gamma\gamma\gamma$ class, except that it also requires that none of the primary tracks have been identified as being minimum ionizing and that the minimum invariant mass of any two central primary tracks be greater than 0.5 GeV.

The final sample of events for each event class is scanned by hand in order to check event identification. This hand scan is based on a graphic display of the event and a dump of pertinent tracking information. Some tracking errors found in the scan are fixed, and a longitudinal momentum balance cut of 4 GeV is applied. The distribution of the longitudinal momentum balance for events passing the hand scan is shown in Figure 4.3. The results of the hand scan are summarized in Table 4.1 and Table 4.2 .

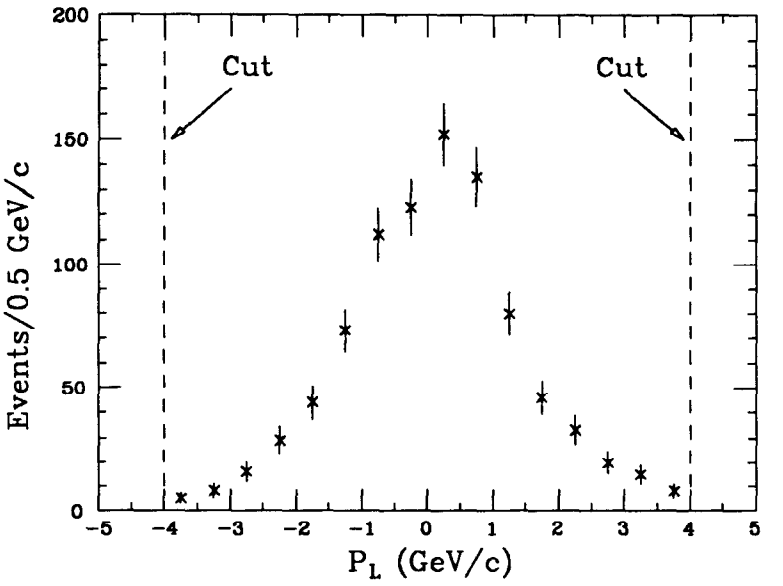

Figure 4.3. Longitudinal momentum distribution for real $e^+e^-\gamma\gamma$ events.

Table 4.1. Results of hand scan for $\gamma\gamma\gamma\gamma$ events.

	2 Central	3 Central	4 Central	Total
$\gamma\gamma\gamma\gamma$	11	11	23	45
$\gamma\gamma\gamma\gamma\gamma$	1	0	2	3
$\gamma\gamma\gamma$	0	1	2	3
$e^+e^-\gamma\gamma$	0	0	6	6
$\gamma\gamma\gamma\gamma$ out of acceptance	1	2	0	3
Junk	1	0	2	3
$P_L > 4$ GeV	1	1	1	3

Most of the categories listed in the tables are self explanatory, though some explanation is necessary. The events in each category (row in the tables) are listed by the number in each topology (2, 3 or 4 central particles) as well as the total of all topologies. Signal events are listed at the top, followed by events identified as α^5 QED. The category listed as $e^+e^-\gamma\gamma$ or $e^+e^-e^+e^-$ in Table 4.2 is for those events that have tracks overlapping in azimuth, such that it is difficult to tell whether only one or both tracks are charged. The events in this category are divided up according to

Table 4.2. Results of hand scan for $e^+e^-\gamma\gamma$ and $e^+e^-e^+e^-$ events.

	2 Central	3 Central	4 Central	Total
$e^+e^-\gamma\gamma$	398	188	325	911
$e^+e^-e^+e^-$	591	42	15	648
$e^+e^-\gamma\gamma$ or $e^+e^-e^+e^-$	14	7	4	25
$e^+e^-\gamma\gamma\gamma$	13	10	14	37
$e^+e^-e^+e^-\gamma$	17	1	2	20
$e^+e^-e^+e^-\gamma$ or $e^+e^-\gamma\gamma\gamma$	4	3	0	7
$e^+e^-\gamma\gamma\gamma\gamma$	0	1	0	1
$\gamma\gamma\gamma\gamma$	3	1	0	4
$e^+e^-\gamma\gamma$ out of acceptance	15	6	0	21
$e^+e^-e^+e^-$ out of acceptance	23	2	0	25
$e^+e^-\gamma\gamma\gamma$ forward track out of acceptance	2	0	0	2
$e^+e^-e^+e^-\gamma$ forward track out of acceptance	1	0	0	1
Minimum ionizing	0	0	2	2
$e^+e^-\gamma$	8	8	32	48
$e^+e^-\gamma$ or $e^+e^-\gamma\gamma$	2	0	1	3
Junk	36	6	5	47
$P_L > 4$ GeV	157	41	22	220

the Monte Carlo predictions from the $e^+e^-\gamma\gamma$ and $e^+e^-e^+e^-$ generators for events in this class. This will be described in detail in the next chapter.

Events identified as being due to α^5 processes have a set of four tracks which pass all the acceptance criteria for α^4 events, plus an extra detected particle with at least 100 MeV of energy. This extra particle need not pass the same acceptance criteria for polar angle, two-track opening angle, energy or two-track invariant mass as do the tracks in α^4 events. These events are discussed further in Chapter 5.

Rejected events are shown in the lower part of the tables. Some of these are

α^3 events ($e^+e^-\gamma$ and $\gamma\gamma\gamma$) that had shower fluctuations or were mistracked and passed the third level filter program. Others are α^4 events that were mistracked and are actually out of the defined energy and angular acceptance regions. Events which include a minimum ionizing particle are also rejected. The *Junk* category is a catch-all class for events which are obviously not signal events, such as high multiplicity events (possibly from tau leptons or hadronic processes) and Bhabha events overlapping on the same beam crossing with cosmic rays, beam gas interactions, $e\gamma(e)$, $ee(ee)$ or other Bhabha events.

The final category shows the events that fail the missing longitudinal momentum cut. Events in this category split into four basic groups. First, many of these would otherwise fall into the *Junk* class and would be rejected anyway. Second, some have four detected particles with an energetic photon or electron missing down the beam line. Third, α^4 QED events that have forward tracks in the region of the beam pipe flange often start showering in the flange. The hits in the PWC are widely scattered, and the particle is often reconstructed as being in the acceptance region. Not only is the energy for the forward particle badly measured because the angle is incorrect, but the poor quality of the PWC hits is readily apparent to the scanner. Finally, some events fail this cut because the energy of one or more central particles is badly measured. This is mainly a problem for photons which convert late in the calorimeter, thus making the energy leakage estimate difficult.

Even though the hand scan is necessary to complete the event selection, the number of events rejected by the scan (not including the momentum cut) is not large in relation to the number of identified signal events. Of the 1865 events that passed the longitudinal momentum cut, 87.3% are α^4 signal events, 3.7% are α^5 QED events, 3.3% are α^4 events that were mistracked and actually out of the acceptance, and only 5.7% are identified as being from other sources.

4.4 Monte Carlo Event Selection

The QED predictions were obtained by running the data analysis filter jobs on Monte Carlo generated events that were then passed through the detector simulation

program (described in Appendix E). The energy and angular limits used in the Monte Carlo generation were well beyond those used as the final acceptance criteria. For example, particles entering the central region were generated with angles down to $\theta_p = 15°$, whereas the final acceptance specifies a 20° cut. All generation limits in angle, energy and invariant mass extended a minimum of three standard deviations (in the appropriate angle, energy or mass variable) beyond the final acceptance criteria.

The luminosity of the Monte Carlo event samples greatly exceeded the actual ASP luminosity of 109.56 pb^{-1}. The results of Monte Carlo event selection are shown in Table 4.3 , Table 4.4 and Table 4.5 . A subset of events in each category was scanned, and the results are shown in Table 4.6 , Table 4.7 and Table 4.8 . The background to the $e^+e^-e^+e^-$ process for three and four central particles is estimated more accurately by scanning all Monte Carlo $e^+e^-\gamma\gamma$ events that have four or five non-neutral tracks (*i.e.* definitely charged or ambiguously charged). The uncertainties shown in the tables are only the statistical uncertainties based on the number of events generated or scanned. These uncertainties will now be considered as systematic uncertainties in the Monte Carlo predictions. Other systematic uncertainties due to detector simulation and hand scanning are discussed in the next chapter.

Table 4.3. Summary of Monte Carlo prediction for $\gamma\gamma\gamma\gamma$ events. The luminosity of the Monte Carlo generation is 3609 ± 33 pb−1. All cross sections are in picobarns.

	2 Central	3 Central	4 Central	Total
Events passing third level filter	427	370	764	1561
$P_L < 4$ GeV/c	426	369	739	1534
Corresponding cross section	0.118 ±0.006	0.102 ±0.005	0.205 ±0.008	0.425 ±0.011
Rejected by hand scan	0.0006 ±0.0006	0.003 ±0.001	0.017 ±0.017	0.020 ±0.004
Net cross section	0.117 ±0.006	0.100 ±0.005	0.188 ±0.009	0.405 ±0.012

Table 4.4. Summary of Monte Carlo prediction for $e^+e^-\gamma\gamma$ events. The luminosity of the Monte Carlo generation is 654.6 ± 2.7 pb-1. All cross sections are in picobarns.

	2 Central	3 Central	4 Central	Total
Events passing third level filter	2621	1371	2142	6134
$P_L > 4$ GeV/c	2618	1362	2123	6103
Corresponding cross section	4.00 $\pm$0.08	2.08 $\pm$0.06	3.24 $\pm$0.07	9.32 $\pm$0.12
Rejected by hand scan	0.12 $\pm$0.05	0.15 $\pm$0.04	0.12 $\pm$0.08	0.38 $\pm$0.06
Background from $e^+e^-e^+e^-$	0.03 $\pm$0.03	0.000 $\pm$0.002	0.001 $\pm$0.001	0.03 $\pm$0.03
Background from $\gamma\gamma\gamma\gamma$	0.0000 $\pm$0.0006	0.0005 $\pm$0.0005	0.002 $\pm$0.002	0.003 $\pm$0.002
Net cross section	3.90 $\pm$0.10	1.94 $\pm$0.07	3.13 $\pm$0.08	8.97 $\pm$0.15

Table 4.5. Summary of Monte Carlo prediction for $e^+e^-e^+e^-$ events. The luminosity of the Monte Carlo generation is 2449 ± 11 pb-1. All cross sections are in picobarns.

	2 Central	3 Central	4 Central	Total
Events passing third level filter	13019	921	329	14269
$P_L > 4$ GeV/c	13001	916	328	14245
Corresponding cross section	5.31 $\pm$0.05	0.374 $\pm$0.012	0.134 $\pm$0.007	5.82 $\pm$0.06
Rejected by hand scan	0.03 $\pm$0.03	0.000 $\pm$0.002	0.0013 $\pm$0.0009	0.03 $\pm$0.03
Background from $e^+e^-\gamma\gamma$	0.08 $\pm$0.04	0.035 $\pm$0.007	0.009 $\pm$0.004	0.12 $\pm$0.04
Net cross section	5.36 $\pm$0.07	0.409 $\pm$0.014	0.142 $\pm$0.008	5.91 $\pm$0.07

Table 4.6. Summary of the hand scan of Monte Carlo $\gamma\gamma\gamma\gamma$ events.

	2 Central	3 Central	4 Central
Events scanned	200	200	200
$\gamma\gamma\gamma\gamma$	199	195	184
$\gamma\gamma\gamma\gamma\gamma$	0	1	1
$e^+e^-\gamma\gamma$	0	1	2
$\gamma\gamma\gamma\gamma$ out of acceptance	0	2	4
$\gamma\gamma\gamma$	0	1	1
$P_L > 4$ GeV/c	1	0	8

Table 4.7. Summary of the hand scan of Monte Carlo $e^+e^-\gamma\gamma$ events.

	2 Central	3 Central	4 Central
Events scanned	200	200	200
$e^+e^-\gamma\gamma$	184	184	182
$e^+e^-\gamma\gamma$ or $e^+e^-e^+e^-$	8	6	11
$e^+e^-e^+e^-$	4	6	0
$e^+e^-\gamma\gamma$ out of acceptance	0	4	1
$e^+e^-\gamma$	2	4	5
$P_L > 4$ GeV/c	0	0	1

Table 4.8. Summary of the hand scan of Monte Carlo $e^+e^-e^+e^-$ events.

	2 Central	3 Central	4 Central
Events scanned	200	200	200
$e^+e^-e^+e^-$	196	193	177
$e^+e^-\gamma\gamma$ or $e^+e^-e^+e^-$	3	5	19
$e^+e^-\gamma\gamma$	1	0	2
$P_L > 4$ GeV/c	0	2	2

5

Results

The results of the data and Monte Carlo analyses are compared in detail in this chapter. Uncertainty calculations are described in the next section, followed by detailed comparisons of differential cross sections for each of the three event classes.

5.1 Systematic Uncertainties

Uncertainties in the Monte Carlo prediction stem from a number of sources. First, there are the systematic uncertainties due to the limited statistics of the Monte Carlo generation. These uncertainties were shown in Section 4.4. Secondly, there are uncertainties arising from the detector simulation due to errors in the determination of positions of detector elements and differences in the values of energy and angular resolutions between real data events and simulated events. Finally, uncertainties are introduced by the hand scan. While all events in the data sample were carefully scanned at least twice by the author, the question arises whether another scanner would yield different results. All uncertainties are summarized in Table 5.1 .

The uncertainties due to detector simulation are straight forward to estimate. The level of uncertainty in the positioning of detector elements is known, and the effect of this on the values of the angular cuts at $\theta_p = 20°$ and $\theta = 50$ mrad are estimated simply by looking at histograms of the distribution of the lowest angle track in an event in the central or forward system. For example, the level of uncertainty for the angular cut in the forward PWC system is 0.16 mrad. The histogram of the

Table 5.1. Systematic uncertainties due to detector simulation, Monte Carlo cross section and hand scan. Each event class is broken down into its respective topologies (two, three or four central particles). The combined uncertainty is all uncertainties in the respective column combined in quadrature. All uncertainties are in percent.

	$\gamma\gamma\gamma\gamma$				$e^+e^-\gamma\gamma$				$e^+e^-e^+e^-$			
Uncertainty	2	3	4	All	2	3	4	All	2	3	4	All
Central θ_p	1.41	2.41	1.94	1.90	1.99	2.47	1.34	2.10	1.31	3.41	2.38	1.46
Forward θ	0.42	0.11	-	0.16	0.51	0.12	-	0.24	0.89	0.25	-	0.83
Central E	0.54	0.31	0.49	0.46	0.39	0.24	0.34	0.34	0.15	0.09	0.18	0.24
Forward E	0.58	3.65	-	1.05	1.05	2.73	-	0.88	0.05	0.65	-	0.10
Central σ_{θ_p}	0.01	0.04	0.02	0.02	0.03	0.04	0.03	0.04	0.01	0.10	0.03	0.02
Forward σ_θ	0.00	0.00	-	0.00	0.00	0.00	-	0.00	0.01	0.00	-	0.01
Central σ_E	0.12	0.03	0.07	0.05	0.03	0.03	0.03	0.03	0.03	0.00	0.01	0.03
Forward σ_E	0.00	0.00	-	0.00	0.00	0.00	-	0.00	0.00	0.00	-	0.00
Shower Width	0.23	0.27	0.13	0.06	0.19	0.07	0.05	0.08	0.07	0.11	0.30	0.06
$P_L < 4$ GeV	0.70	1.63	2.57	1.83	0.29	0.40	0.85	0.51	0.26	0.11	0.96	0.26
Hand Scan	1.00	1.00	1.00	1.00	1.00	1.00	1.00	1.00	1.00	1.00	1.00	1.00
Predicted Cross Section	4.94	5.42	4.58	2.94	2.51	3.51	2.65	1.62	1.32	3.42	5.92	1.25
Combined	5.36	7.24	5.71	4.24	3.59	5.21	3.27	3.04	2.31	4.99	6.54	2.35

lowest angle forward track for Monte Carlo $e^+e^-e^+e^-$ events (Figure 5.1) shows 1450 events in the 2 mrad bin at the 50 mrad cut, out of 13001 events total. The estimate of the uncertainty is simply

$$\left(\frac{1450}{2} \times 0.16\right) / 13001 = 0.89\% \tag{5.1}$$

This procedure was also performed for the central angular cut (uncertainty = 0.24° at $\theta_p = 20°$), the forward energy cut (uncertainty = 0.25 GeV at $E = 4$ GeV) and the central energy cut (uncertainty = 3 MeV at $E = 300$ MeV).

The uncertainties due to differences in energy and angular resolution are more difficult to estimate. For example, if the cross section is rising rapidly at the angular cutoff and the angular resolution from the Monte Carlo is less than that of the real

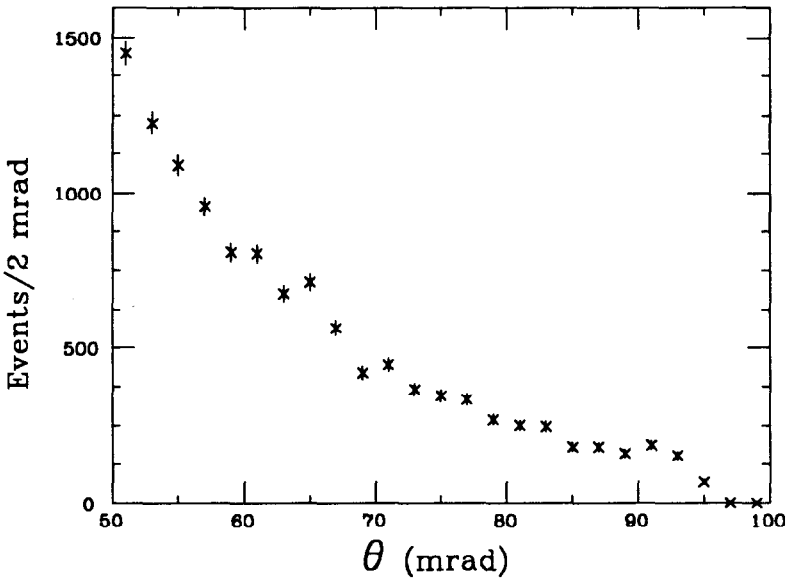

Figure 5.1. Distribution of lowest angle forward tracks for $e^+e^-e^+e^-$ events.

detector, then the feed-up from events whose real trajectory is below the cut into the region above the cut (due to the tracking resolution) will be greater for the data than the Monte Carlo, and the Monte Carlo will underestimate the expected cross section. How this uncertainty is estimated is best illustrated by looking at the Monte Carlo $e^+e^-e^+e^-$ sample in Figure 5.1. The forward angular resolution is 1.92 ± 0.03 mrad. The extra smearing required to get a total resolution of $1.92 + 0.03 = 1.95$ mrad is $\sigma_{ex} = \sqrt{(1.95)^2 - (1.92)^2} = 0.34$ mrad. The extra feed-up of events from below the 50 mrad cut is estimated by using a program which breaks the region 48-52 mrad into 0.1 mrad bins, calculates the number of expected events in that bin from the measured differential cross section (Figure 5.1), then calculates the number of events that feed up into the acceptance region and feed down out of the acceptance region by integrating a Gaussian distribution using σ_{ex}. The difference between the feed-up and the feed-down is then the estimate of the uncertainty in the Monte Carlo prediction due to the uncertainty in the angular resolutions. As seen in Table 5.1, the effect of the uncertainty in angular and energy resolution is small.

The uncertainty introduced by the shower width cut in the lead-glass system is simple to estimate. As can be seen from Figure 4.2, the shower widths from the real data and the Monte Carlo simulation agree to better than 0.00005 m^2 (half a

bin width), and the shower width distribution is quite small at the width cuts. The level of uncertainty is estimated by simply decreasing the width cuts by 0.00005 m^2 in the analysis program and observing the effect on the Monte Carlo events. These uncertainties are quite small, as shown in Table 5.1. If no events are eliminated by the changed width cut, then the uncertainty for a category is estimated by simply dividing 1.0 by the number of events in that category.

How to best estimate the uncertainty in the total longitudinal momentum cut is a difficult question. The distribution of total longitudinal momentum for real and Monte Carlo $e^+e^- \rightarrow e^+e^-\gamma\gamma$ events is shown in Figure 5.2, and the cut at 4 GeV is well away from the main peak for both the real and Monte Carlo events. The distribution for real data is slightly broader than the distribution for the Monte Carlo, but that could easily be due to differences between the real detector resolution and the simulated detector resolution for total longitudinal momentum. The Monte Carlo events that fail this cut do so typically because of late showering photons in the central detector. The energy leakage estimates which are used to reconstruct the energy of the initial photon were found using the detector simulation, so it is no surprise that the resolution is slightly better for the Monte Carlo than for the real data. Some extra width in the real data may also be due to Bremsstrahlung radiation down the beam line (not included in the Monte Carlo). It is not clear whether the differences in the widths is primarily due to detector simulation differences or due to Bremsstrahlung. The uncertainty due to the longitudinal momentum cut is simply given as the fraction of Monte Carlo events in the region $3.5 < |P_L| < 4.0$ GeV/c. The results are shown in Table 5.1.

The accuracy of the hand scan was checked by employing another scanner[17] (other than the author) to scan a set of two hundred events. The set of events given to the scanner was a random mixture of real data and Monte Carlo events, with approximately the same number of each kind (data vs. Monte Carlo). No information was given to the scanner which could allow him to determine the origin of the event. The results found by the second scanner were then compared with the results found

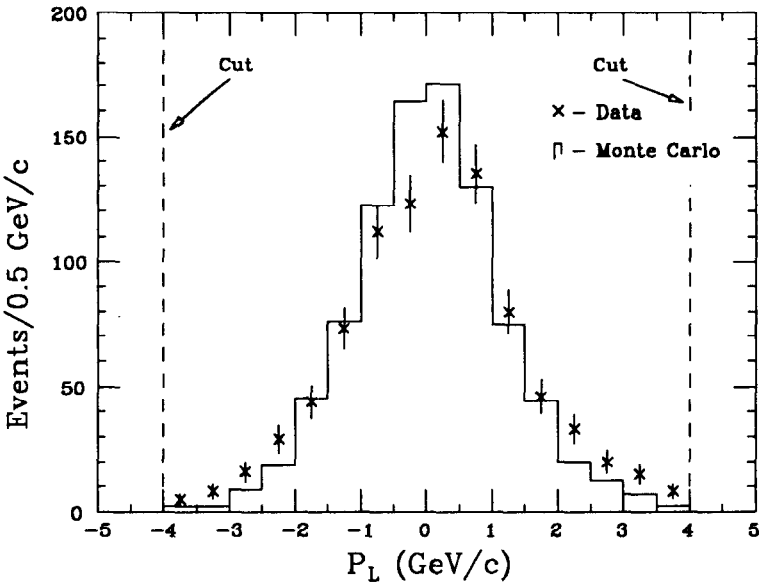

Figure 5.2. Longitudinal momentum distributions for real and Monte Carlo $e^+e^-\gamma\gamma$ events.

by the original scanner (the author). There was no disagreement on deciding which events should be rejected. The only disagreement between the two scanners occurred for deciding whether some events belonged in the $e^+e^-\gamma\gamma$ class or in the '$e^+e^-\gamma\gamma$ *or* $e^+e^-e^+e^-$' class. However, since most of the events in this class are assigned to the $e^+e^-\gamma\gamma$ class anyway (see the next section), the effect on the result is minimal (less than 0.25% for both the $e^+e^-\gamma\gamma$ and $e^+e^-e^+e^-$ results).

Although no serious problem was found with the hand scan, the number of events scanned was limited to two hundred. A different set of two hundred events might have shown some disagreement, but probably no more than a couple of events. Hence, the uncertainty for the hand scan is estimated to be 2/200 = 1%.

5.2 Results

The number of events from both the data and the Monte Carlo prediction are compared in Table 5.2 for all event classes. The agreement is good in all categories. Events in the class '$e^+e^-\gamma\gamma$ *or* $e^+e^-e^+e^-$' shown in Table 4.2 are assigned to the $e^+e^-\gamma\gamma$ and $e^+e^-e^+e^-$ classes according to the ratio of the cross sections for the '$e^+e^-\gamma\gamma$ *or* $e^+e^-e^+e^-$' class as given by the hand scan of Monte Carlo $e^+e^-\gamma\gamma$ and $e^+e^-e^+e^-$ events. The hand scan shows that 66.7 ± 21.7% of the events in the '$e^+e^-\gamma\gamma$ *or* $e^+e^-e^+e^-$'

class for the topology with two central tracks originate from the $e^+e^-\gamma\gamma$ process. (The uncertainty of 21.7% is due to the statistical counting uncertainty based on the number of events found in the hand scan.) This ratio is $89.6 \pm 4.8\%$ for three central tracks and $93.4 \pm 2.4\%$ for four central particles.

Table 5.2. Comparison of the number of events in the data and in the Monte Carlo prediction for all event classes. The first uncertainty for the ratios is systematic, and the second is statistical.

Topology	Data	Prediction	Data	Prediction	Data	Prediction
	$\gamma\gamma\gamma\gamma$		$e^+e^-\gamma\gamma$		$e^+e^-e^+e^-$	
2 central	11	12.9	408	428	595	587
3 central	11	10.9	194	212	43	44.8
4 central	23	20.6	329	343	15	15.5
All	45	46.6	931	983	653	648
Data/Pred	$0.97 \pm 0.04 \pm 0.14$		$0.94 \pm 0.03 \pm 0.03$		$1.01 \pm 0.02 \pm 0.04$	

The following sections show comparisons of the differential cross sections for all event classes. Since it is impossible to know from which process any particular event in the '$e^+e^-\gamma\gamma$ *or* $e^+e^-e^+e^-$' class came, all events in this class are assigned to the $e^+e^-\gamma\gamma$ class for the purposes of comparing differential cross sections. All Monte Carlo distributions are normalized so that there are the same number of Monte Carlo events as data events.

5.2.1 $\gamma\gamma\gamma\gamma$

All differential distributions for the $\gamma\gamma\gamma\gamma$ event class show excellent agreement, with no evidence of any anomalies. The distributions in polar angle are shown in Figure 5.3, and the distribution in energy is shown in Figure 5.4. The invariant mass combinations of all pairs of photons are shown in Figure 5.5. No evidence is seen for any anomalous mass peaks.

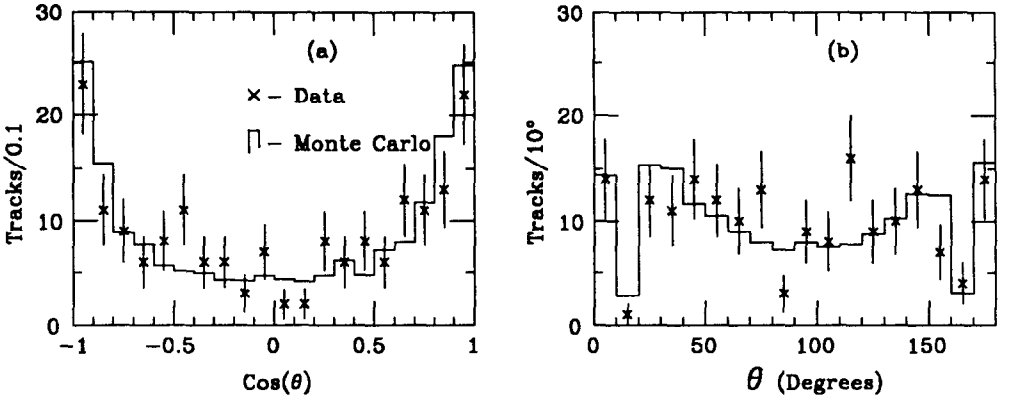

Figure 5.3. Distribution of photons in $\gamma\gamma\gamma\gamma$ events in $\cos(\theta)$ (a) and θ (b). The dips near 15° and 165° are due to the gaps in the angular acceptance criteria.

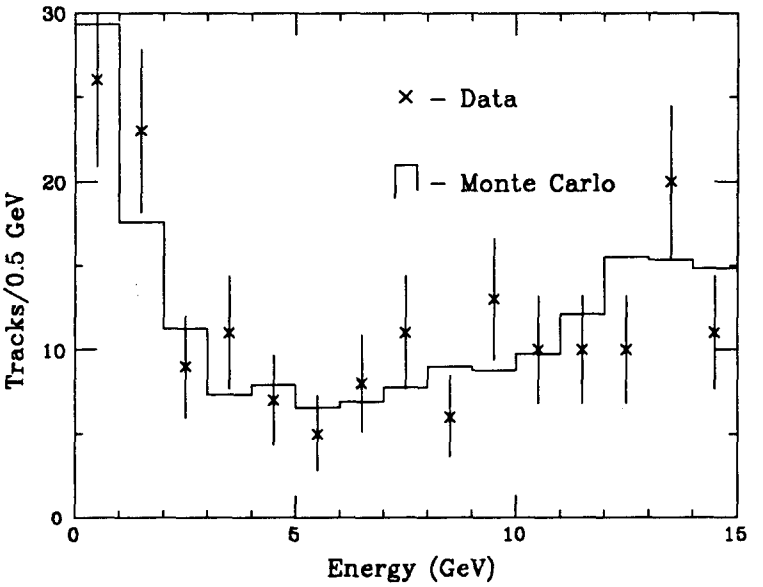

Figure 5.4. Energy distribution of photons in $\gamma\gamma\gamma\gamma$ events.

5.2.2 $ee\gamma\gamma$

Like the $\gamma\gamma\gamma\gamma$ class, all distributions in the $e^+e^-\gamma\gamma$ class show excellent agreement. The higher statistics in this class allow a more detailed comparison of the data and the Monte Carlo predictions. This is evidenced in the $\cos(\theta)$ and energy distributions for all tracks (irregardless of charge) and unambiguously identified photons, as shown in Figure 5.6 and Figure 5.7. The invariant mass distribution of all $e^{\pm}\gamma$ (Figure 5.8) pairs show no anomalous mass peaks. (Only the events in which

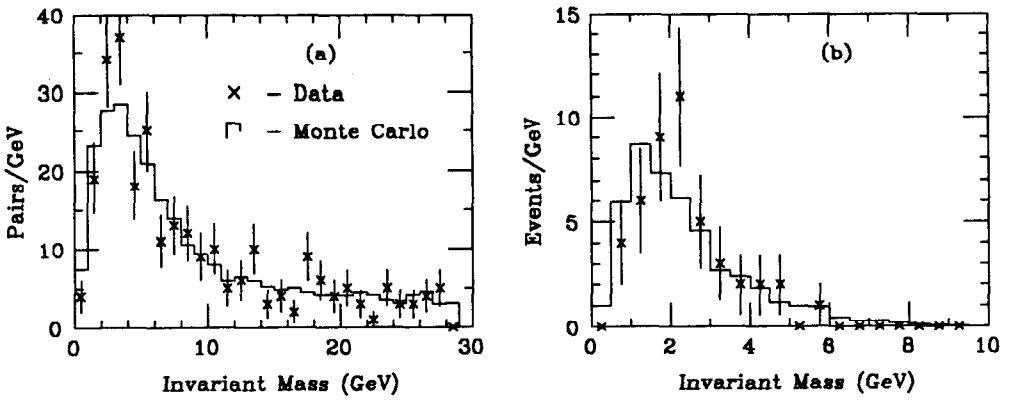

Figure 5.5. Invariant mass distribution in $\gamma\gamma\gamma\gamma$ events for all photon pairs (a) and lowest mass pair (b).

two photons are clearly identified are used in this last histograms. The criteria for selecting $e^+e^-\gamma\gamma$ events allowed one of the photons to convert in the beam pipe or the first layers of the central tracker or drift chambers.)

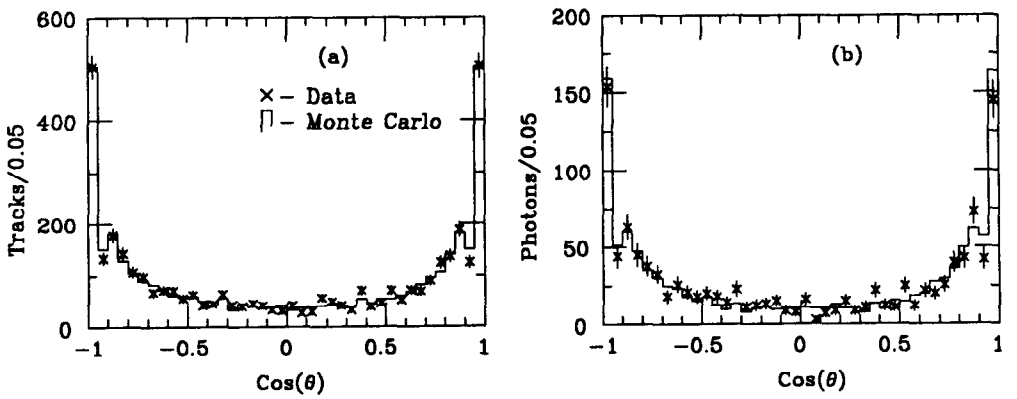

Figure 5.6. $Cos(\theta)$ distributions in $e^+e^-\gamma\gamma$ events for all tracks (a) and unambiguously identified photons (b).

5.2.3 eeee

It should come as no surprise that the differential distributions for $e^+e^-e^+e^-$ events show excellent agreement as well. The distributions of all tracks in polar angle and energy are shown in Figure 5.9 and Figure 5.10. The invariant mass combinations

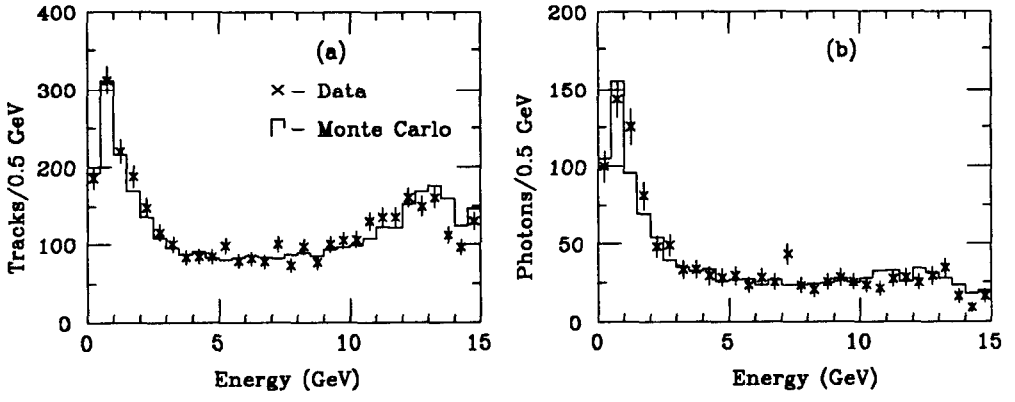

Figure 5.7. Energy distributions in $e^+e^-\gamma\gamma$ events for all tracks (a) and unambiguously identified photons (b).

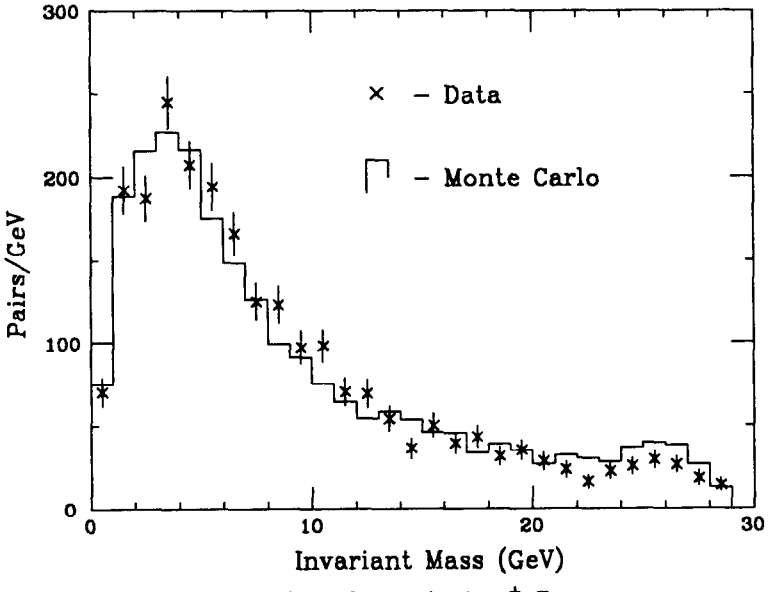

Figure 5.8. Invariant mass distribution of $e\gamma$ pairs in $e^+e^-\gamma\gamma$ events.

of all tracks, irregardless of the charge, are shown in Figure 5.11. (Recall that ASP can't measure the sign of the charge.) No anomalous peaks are observed.

5.2.4 *Fifth and Sixth Order QED*

Tables 4.1 and 4.2 show that a total of 67 events (that did not have a problem with a forward track) are identified as being from α^5 processes. There is even one candidate $e^+e^-\gamma\gamma\gamma\gamma$ event. Most of these events have photons which are outside of the acceptance criteria used for the four tracks in α^4 events. Table 5.3 shows the number

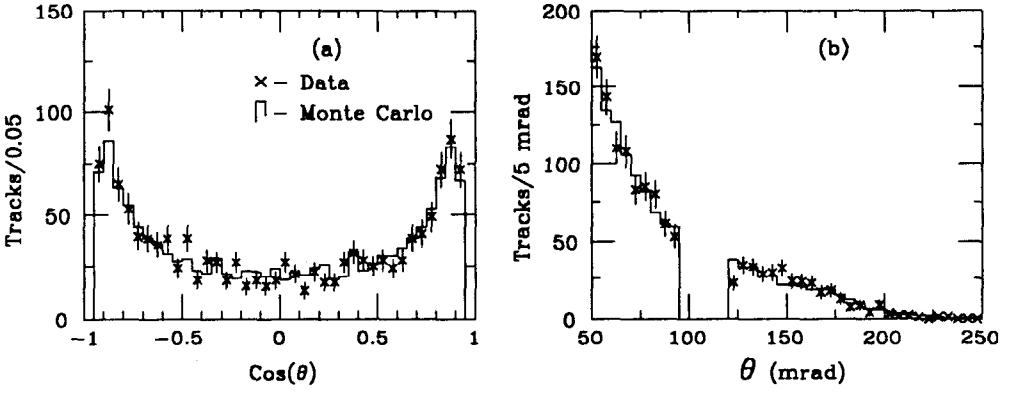

Figure 5.9. Angular distributions of tracks in $e^+e^-e^+e^-$ events. Figure (a) shows the distribution in $\cos(\theta)$ of all tracks in the region defined by $|\cos(\theta)| < 0.95$. For comparison, there are 608 tracks in the region $\cos(\theta) < -0.95$ and 612 tracks in the region $\cos(\theta) > 0.95$. Figure (b) shows the distribution of low angle tracks versus θ.

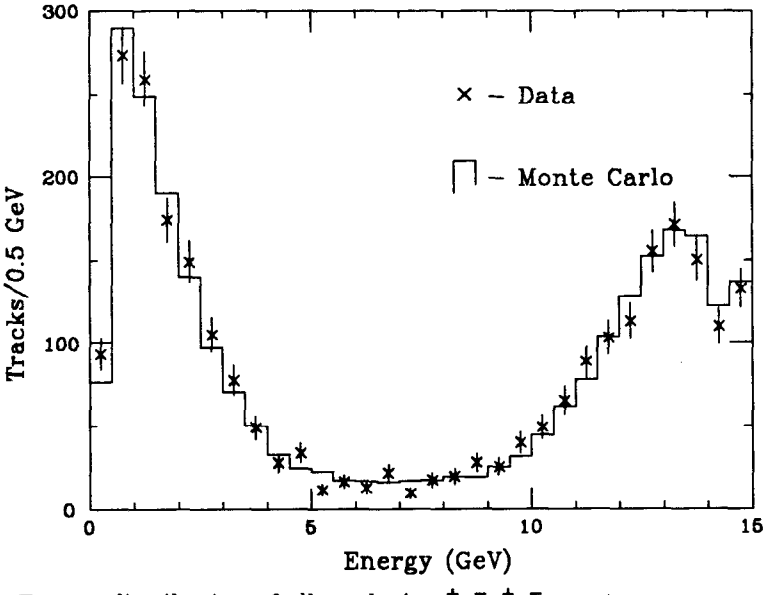

Figure 5.10. Energy distribution of all tracks in $e^+e^-e^+e^-$ events.

of five-body events that pass the same acceptance criteria used to select the usual four-body events (including two-track opening angle and invariant mass criteria). The graphical display of an $e^+e^-e^+e^-\gamma$ event in the ASP detector is shown in Figure 5.12 The one six-body event has a photon with energy $E = 0.25$ GeV (the acceptance criteria requires 0.3 GeV) but otherwise passes the remaining criteria.

There are no published calculations of the matrix elements for the $e^+e^-\gamma\gamma\gamma$ or

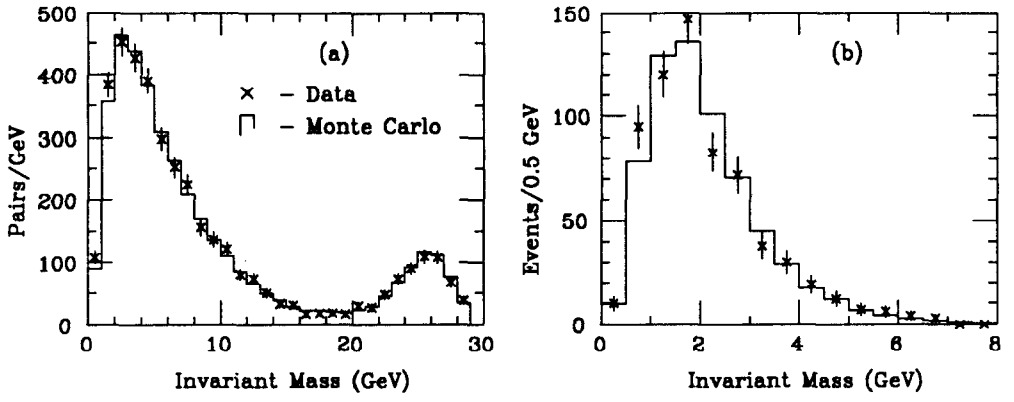

Figure 5.11. Invariant mass distribution in $e^+e^-e^+e^-$ events for all track pairs (a) and lowest mass pair (b).

Table 5.3. Summary of fifth order QED events.

Topology	$\gamma\gamma\gamma\gamma\gamma$	$e^+e^-\gamma\gamma\gamma$	$e^+e^-e^+e^-\gamma$
2 central	1	7	6
3 central	0	7	1
4 central	1	5	0
Total	2	19	7

$e^+e^-e^+e^-\gamma$ processes (for the wide angle topologies) at this time, although there is a calculation for the 5γ process by Brown *et al.*[18]. No attempt was made to write a Monte Carlo program for the 5γ process. Unfortunately, simple Bremsstrahlung estimates are inadequate for these five-body processes because interference terms between the various Feynman diagrams for initial state radiation, final state radiation, and the exchange of photons indices dominate the cross section. The interference terms dominate because the photons are not allowed to be colinear with any initial or final state charged particle.

One way to estimate the expected α^5 cross section is to determine the fractional decrease in cross section between an α^3 process and an α^4 process for the same acceptance criteria. A comparison of cross sections from an $e^+e^-\gamma$ Monte Carlo program[19]

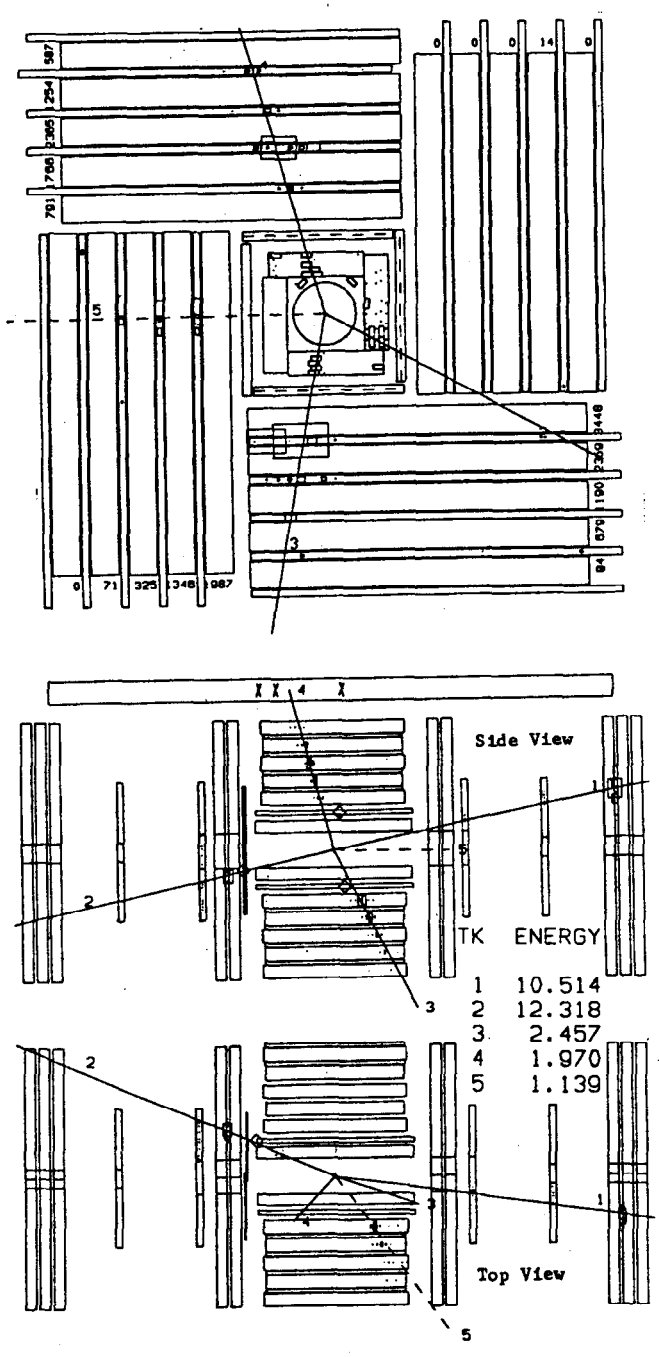

Figure 5.12. Display of a $e^+e^-e^+e^-\gamma$ event in the ASP detector. The scale of the X and Y axes has been magnified in the *top* and *side* views for clarity. Detector elements with signal are drawn as rectangles, where the size of the rectangle is proportional to the signal.

and the $e^+e^-\gamma\gamma$ program is made for acceptance criteria similar to those used for the α^4 analysis. This ratio is

$$R = \frac{\sigma_{ee\gamma\gamma}}{\sigma_{ee\gamma}} = 1.6 \pm 0.1\% \tag{5.2}$$

One thus might expect that there be a decrease of a factor of R in the cross section for every extra order in α. (This is only for events where all tracks pass the acceptance criteria.) The ratio of measured five-body to four-body final states is $4.4 \pm 3.1\%$ for 5γ, $2.0 \pm 0.5\%$ for $e^+e^-\gamma\gamma\gamma$, and $1.1 \pm 0.4\%$ for $e^+e^-e^+e^-\gamma$, where the uncertainty listed for each ratio indicates the simple statistical counting uncertainty (based on Poisson statistics - $\sigma = \sqrt{N}$). These ratios are consistent with the predicted ratio.

Even though one photon in the $ee4\gamma$ event (shown in Figure 5.13 fails the energy acceptance criteria, it is the first of its kind ever observed. The number of $ee4\gamma$ events expected can be estimated in a manner similar to the one used to estimate the number of α^5 events expected. There were 43 observed $ee3\gamma$ events (including the appropriate fraction of events in the '$e^+e^-\gamma\gamma\gamma$ *or* $e^+e^-e^+e^-\gamma$' class) which had no more than one track failing the acceptance criteria. The ratio of these 43 events to the number of $e^+e^-\gamma\gamma$ events is 4.6%. The number of $ee3\gamma$ events that pass all acceptance criteria is 19, so the number of $ee4\gamma$ events expected where up to one track may fail the acceptance criteria is $19 \times 0.046 = 0.9$ events. This is consistent with the one observed event.

5.3 Discussion on Radiative Corrections

The precision of the α^4 measurements makes it possible to observe the radiative corrections to α^4 QED. The most definite evidence for radiative corrections is the observation of the five-body α^5 and six-body α^6 events described in the previous section. However, not all radiative effects lead to a visible particle in the detector.

The experimentally observed cross section may be expressed in terms of radiatively corrected lowest order cross section as

$$\begin{aligned} \sigma_{exp}(e^+e^- \to X) &= (1 + \delta_{rc})\sigma_0(e^+e^- \to X) \\ &= \sigma_{soft}(e^+e^- \to X) + \sigma_{hard}(e^+e^- \to X\gamma) \end{aligned} \tag{5.3}$$

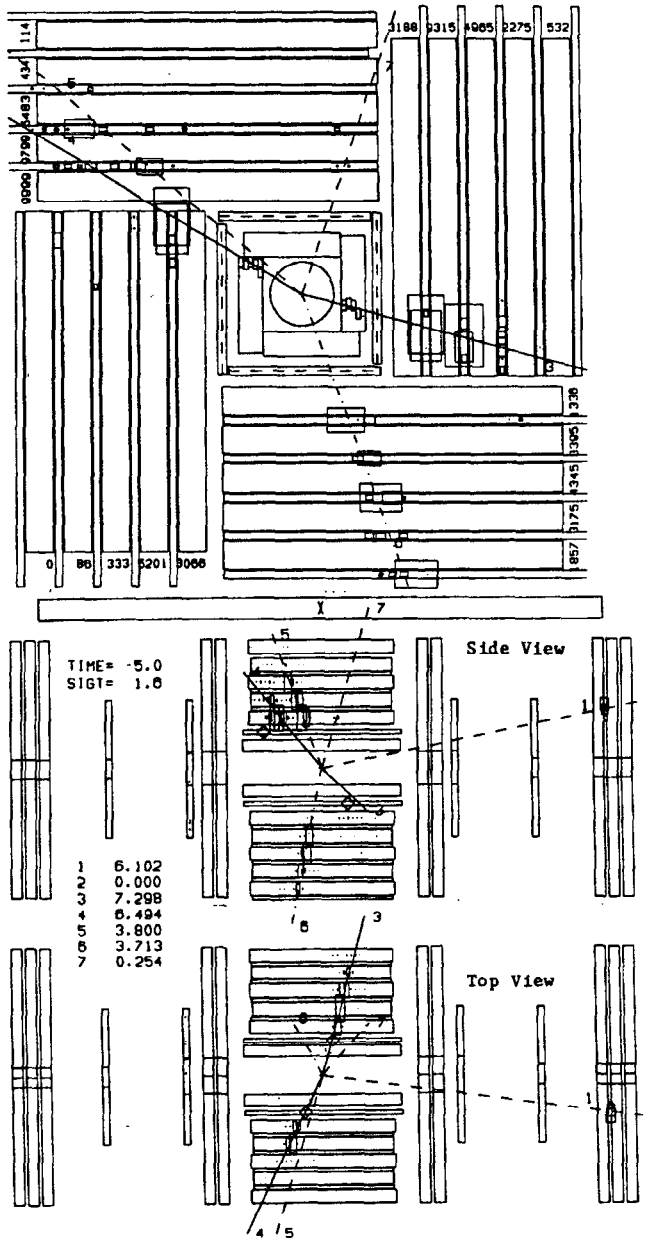

Figure 5.13. Display of the candidate $ee4\gamma$ event in the ASP detector.

where σ_{exp} is the experimentally observed cross section, σ_0 is the lowest order cross section, σ_{soft} is the cross section with soft photon radiative corrections, and σ_{hard} is the cross section with energetic photons. The hard radiative correction is simply the calculation of the lowest order process accompanied by an extra energetic photon. The soft radiative correction includes both the corrections due to loop diagrams (self

energy, vertex and vacuum polarization) as well as soft Bremsstrahlung. Both the loop and Bremsstrahlung corrections to the lowest order cross section are large and diverge for small photon energies, but they of are opposite sign and nearly cancel each other. The boundary between soft and hard Bremsstrahlung is arbitrary, but it is generally chosen to be about 1% of the beam energy. The lowest order cross section σ_0 may be smaller or larger than σ_{soft} or σ_{hard}, depending on the value of the soft/hard boundary (k_0).

A simple estimate of the radiative corrections to $e^+e^- \rightarrow e^+e^-\gamma\gamma$ may be obtained from the known radiative corrections to $e^+e^- \rightarrow e^+e^-$ since both processes involve the same number of electrons and positrons of similar energies. The radiative corrections are proportional to $\ln(\gamma)$, where $\gamma = Energy/Mass$. This quantity, $\ln(\gamma)$, only changes by 10% between 14.5 GeV and 5 GeV electrons, so the level of radiative corrections to $e^+e^- \rightarrow e^+e^-\gamma\gamma$ will be similar to that of $e^+e^- \rightarrow e^+e^-$ despite the lower energies of the final state electrons and positrons in the $e^+e^-\gamma\gamma$ case. Since Monte Carlo programs are available for the $e^+e^- \rightarrow e^+e^-$ case with radiative corrections, the detector acceptance cuts can be applied, as was done in the previous section to obtain the expected number of five body events.

The level of radiative corrections was obtained from a Bhabha Monte Carlo program written by Berends *et al.*[19]. Both the electron and the positron were required to be in the region $\theta > 30°$. The lowest order cross section was 3.282 nb. The hard/soft boundary in the Monte Carlo was set to $k_0 = 0.1$ GeV (the same energy used to identify five and six body events). Along with the requirement that the electrons and positrons have $\theta > 30°$, the event was discarded if one of the following three conditions was met for generated photons:

1. 21 mrad $< \theta_k < 20°$ and $E_k > 1$ GeV
2. $\theta_k < 21$ mrad and $E_k > 4$ GeV
3. $\theta_k > 20°$, $\Delta\theta_{e,k} > 20°$ and $E_k > 0.1$ GeV.

The results are shown in Table 5.4, where the fractional cross sections (with respect to the lowest order cross section, σ_0) are shown after each of the above cuts was made.

Table 5.4. Effects of photon acceptance criteria on radiative Bhabha scattering.

After Cut	σ_{exp}/σ_0
None	1.071
1	1.023
2	0.985
3	0.950

Note the effect of these simple experimental cuts (similar to those used in the $e^+e^- \rightarrow e^+e^-\gamma\gamma$ analysis) actually make the experimental cross section 5% smaller than the lowest order cross section. It is interesting to note that the measured $e^+e^- \rightarrow e^+e^-\gamma\gamma$ cross section is 6% below the lowest order (α^4) calculated cross section.

5.4 Conclusion

The measurements presented in this thesis are the world's most precise and highest statistics measurements of the $e^+e^- \rightarrow \gamma\gamma\gamma\gamma$, $e^+e^- \rightarrow e^+e^-\gamma\gamma$ and $e^+e^- \rightarrow e^+e^-e^+e^-$ processes for all particles separated from the beam line and each other. The agreement with QED predictions is good for all event classes and all differential distributions. The cross sections for these processes are shown to be significant, and should be considered by anyone performing exotic particle or missing momentum searches. These results also demonstrate the accuracy of the complex QED matrix element calculations and Monte Carlo programs used to make the theoretical predictions.

The 28 fifth-order QED events (that satisfy all the acceptance criteria) represent the first measurements at high energies of the $e^+e^- \rightarrow 5\gamma$, $e^+e^- \rightarrow e^+e^-\gamma\gamma\gamma$, and $e^+e^- \rightarrow e^+e^-e^+e^-\gamma$ processes, where all particles are separated from the beam line and each other. The one $ee4\gamma$ event also represents the first reported observance of six particle production in an α^6 QED process. The number of events found in both the α^5 and the α^6 classes are consistent with estimates of their event rates. The observation of these very high-order processes demonstrates the efficiency of the analysis and of the ASP detector for observing rare processes.

Appendix A

Gas Monitors

The short term stability of the gas used in the ASP proportional wire chambers was monitored by a set of small proportional wire tubes irradiated by a radioactive source. The average current drawn a such a gas monitor is proportional to the gain of the gas used. The signal from the gas monitors was available during data taking, and was used to indicate the presence of bad gas or a halt in the gas flow. Long term calibration of proportional wire chamber responses was performed by an off-line analysis of the signals for Bhabha and cosmic ray events in the various PWC systems.

Gas monitors for the central PWC, forward PWC and drift chambers were made from 10 × 1 × 5/8 inch aluminum tubes (Figure A.1) cut from the same extrusions used to make the central and forward PWC systems. A 48 μm gold plated tungsten wire was strung down the center. A thin window for the radioactive source was made by drilling a 1/8 inch diameter hole in the top center of the tube and covering the hole with copper tape. The gas monitor for the central tracker PWC system was made using a 10 inch segment of the thin walled aluminum tubes used to make the central tracker and strung with the same wire used in the CT system. There was no need to make a thin window since the 12 mil walls were sufficiently thin already. A 50 μCu Strontium 90 e^- source was chosen to irradiate the tubes because of long 28 year half-life of Sr^{90}.

The average current from the tube is found by measuring the ground return current with an RC filter and a FET operational amplifier (see Figure A.2). The

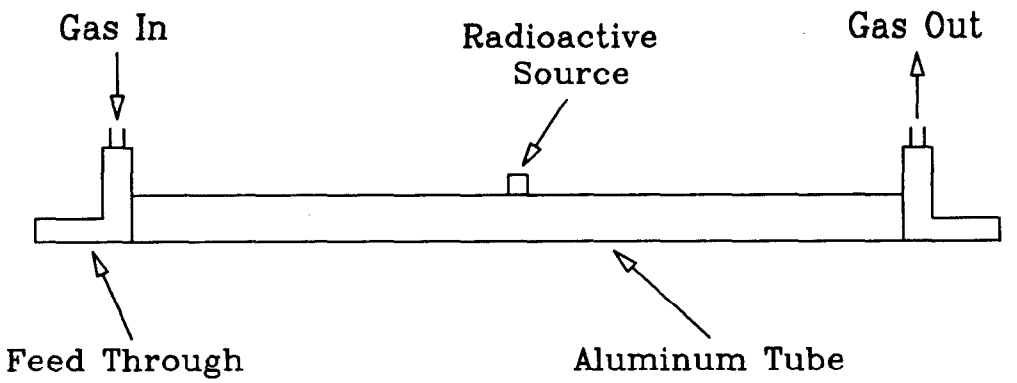

Figure A.1. Gas monitor tube.

time constant for the RC filter was 4.4 seconds. The ground return was chosen because it is much easier to read this current rather than monitoring the current on the high voltage wire. Of course, if the drift velocity or the pulse shape needed to be monitored, then it would have been necessary to monitor the signal on the high voltage wire. But since only the monitoring of the gas gain was needed, the average ground return current was sufficient. The average current for a given gas gain could be chosen by simply adjusting the high voltage on the wire. The voltage was chosen at the beginning of operation of the system so that a current of 30 nA was obtained in each tube. 30 nA was chosen in order to obtain a stable current reading from the RC filter circuit.

The gas monitor tube with attached feed throughs for the high voltage wire and gas ports was enclosed in a sheet metal box that could be easily mounted at various points around the ASP detector. The gas tube was placed in a lucite holder which served to electrically insulate the walls of the cell. Lead shielding was place around this lucite holder, and the assembly mounted inside the sheet metal box. Connectors for the high voltage and ground return cables were mounted on the top of the box.

The gas monitors performed well as a short term monitoring system. The data acquisition computer signaled a warning whenever there was greater than a 5% change

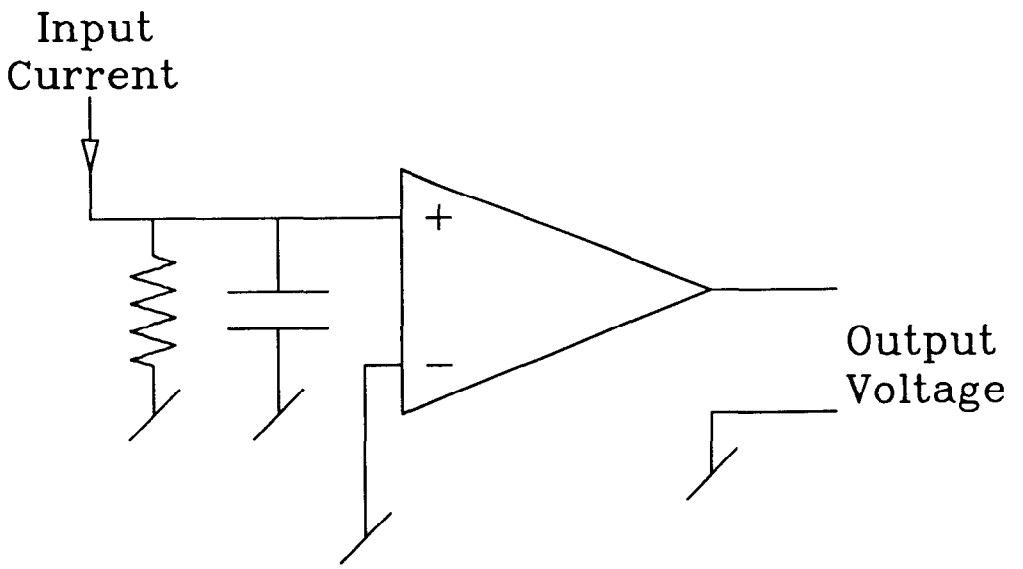

Figure A.2. Basic circuit used to average the current coming from a gas monitor tube.

in the response any of the monitor tubes. Unfortunately, the long term stability of the gas monitors was degraded due to wire damage. The ionization avalanche occurring in the proportional wire cell was concentrated on a $\approx$ 1 cm section of the wire. It would have been better if the radioactive source had been spread out over the entire length of the cell.

Appendix B

Luminosity

The ASP luminosity was determined using low angle Bhabha events that enter the outer forward shower counters. The large Bhabha cross section combined with accurate track reconstruction in the Forward PWC system (Appendix D) allows the determination of luminosity with a precision of 1.1%.

Low angle Bhabha events were collected using a special trigger. The trigger required a signal in both outer shower counters above a threshold of approximately 7 GeV. Due to the high rate of such events, these triggers were prescaled by a factor of 600. Simply counting the number of times the trigger pattern was satisfied yielded a fast measurement of the luminosity. The precise value of the luminosity was determined using an off-line analysis.

The forward tracking was performed solely with the forward PWC system. The drift chamber system was often unreliable because electrons often start showering in the beam pipe, leading to high occupancies in the drift chamber. The resolution of the PWC system was 2 mrad in polar angle, and the uncertainty in the systematic offset of the polar angle was 0.16 mrad. (See Appendix D for details.)

The angular acceptance region used for the luminosity analysis was chosen so as to avoid problem areas in the forward region. A track was required within the interval defined by $55 < \theta < 95$ mrad on one side ($+Z$ or $-Z$), and a second track was required within the interval defined by $50 < \theta < 100$ mrad on the other side in

Z. These cuts avoided problems introduced by a flange in the beam pipe below 45 mrad. Only the highest energy tracks on each side in Z were used. The two tracks had to be colinear to within 20 mrad. This reduced the level of radiative corrections needed to calculate the QED prediction for the cross section.

Only two other cuts were required to eliminate background events. The first cut required that there be less than 0.5 GeV in the lead-glass system. This reduced the background from higher order QED processes that pass the angular acceptance. The last cut required that there be at least 2.5 GeV of energy visible in the shower counter layers behind the PWC planes. Events that shower early in the flange region (less than 45 mrad) often yield PWC hits above 50 mrad. This cut requires that sufficient energy passed through the PWC plane so that the PWC could accurately reconstruct the track. Bhabha events in the flange region typically have less than 2.5 GeV in the back layers, whereas events above 50 mrad typically have more than 4 GeV of energy in the back layers, as shown in Figure B.1. The events in this figure were chosen by using all the same criteria used to determine the experiment luminosity, except for the low and high angle cutoffs and, of course, the back energy cut. Note that between 65 and 90 mrad (well away from the flange region and the inner/outer shower counter overlap region) there are no events with back energy less than 2.5 GeV. Since it is known that the flange ends at 45 mrad and the inner shower counter extends down to 100 mrad, it is assumed that all events with back energy less than 2.5 GeV are actually in the flange region or the overlap region, and thus are not within the defined angular acceptance.

Uncertainties in the luminosity measurement due to uncertainties in tracking and energy cuts are displayed in Table B.1 . The uncertainties in the FPWC offsets and resolutions (assumed to be Gaussian) introduce uncertainties in the QED prediction. The back energy cut of 2.5 GeV and the trigger thresholds also introduced some error. The back energy cut only eliminated 1.33% of the events, and since there was no independent way of determining the cut's efficiency other than hand scanning the events eliminated, half the fraction of events cut (0.67%) was assigned as the uncertainty. The *end run truncation* refers to the Bhabha trigger prescalar being

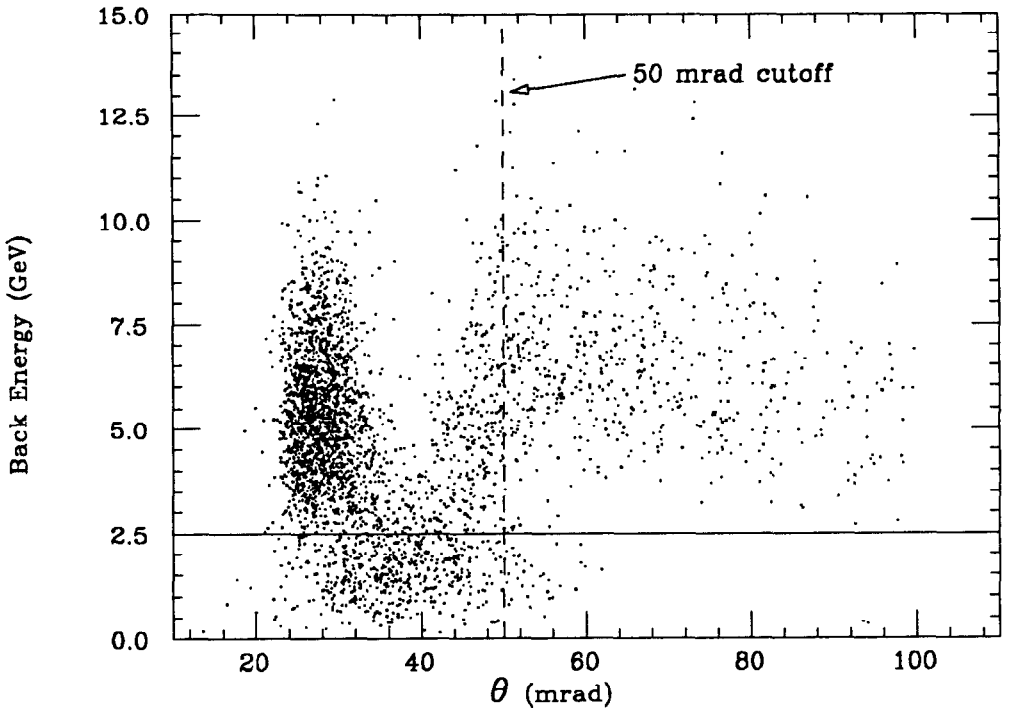

Figure B.1. Back energy versus θ_{pwc} for low angle Bhabha events.

truncated (*i.e.* reset to zero) at the end of each run. A correction of 0.2% is applied to the luminosity, with a 0.1% uncertainty (a conservative overestimate).

Table B.1. Uncertainties in luminosity measurement.

	Uncertainty (%)
PWC Offsets	0.33
PWC Resolutions	0.02
End Run Truncation	0.10
FS Thresholds	0.13
Back Energy Cut	0.67

The QED prediction for the low angle Bhabha cross section was obtained from two Bhabha Monte Carlo programs written by Berends *et al.*[19,20]. The later version included more radiative corrections, but was still somewhat developmental at the

time of the luminosity analysis. The predictions from the two programs differed by 1.44%, so an average value of the two was used as the predicted cross section, with an uncertainty of 0.72%. The predicted cross section was 268 ± 2 nb without smearing the track angles by the FPWC resolution, and it was 283 ± 2 nb with smearing.

The measured luminosity is

$$109.56 \pm 0.48(stat) \pm 0.83(syst) \pm 0.79(QED)\ pb^{-1}$$

The first uncertainty is simply the statistical counting uncertainty, the second is the systematic measurement uncertainties combined in quadrature and the third is the uncertainty in the QED prediction due to the difference in the two Bhabha Monte Carlo programs. The differential cross sections for the data and the Monte Carlo are in excellent agreement, as shown in Figure B.2. The ratio of the differential cross sections versus θ for the data to the Monte Carlo is shown in Figure B.3. The error bars in this figure indicate only the statistical uncertainty, as the systematic uncertainties are small in relation to the statistical (for each 1 mrad bin) except near the acceptance cutoffs at $\theta = 55$ and $\theta = 95$ mrad. When all bins are summed together, the statistical uncertainty drops below 0.5%, and the systematic uncertainties dominate.

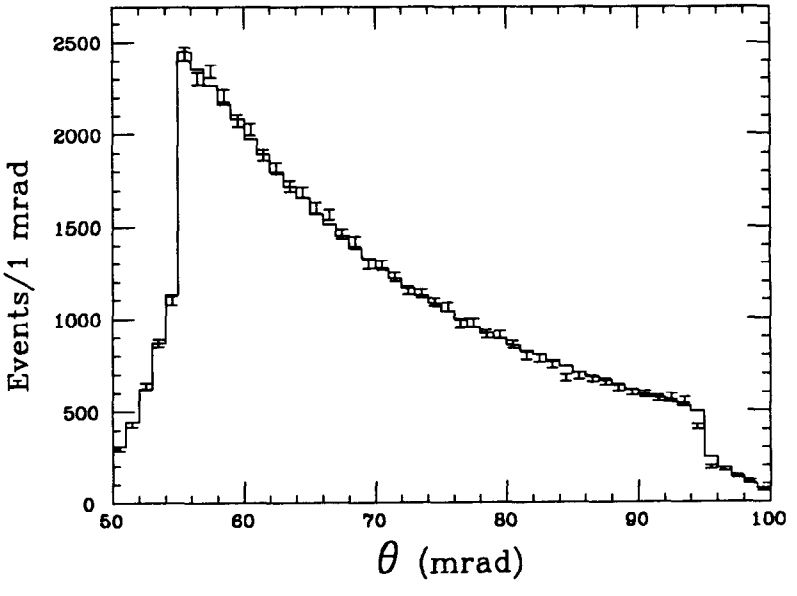

Figure B.2. Low angle Bhabha θ distribution. Histogram plot is the Monte Carlo prediction, points with error bars are the data.

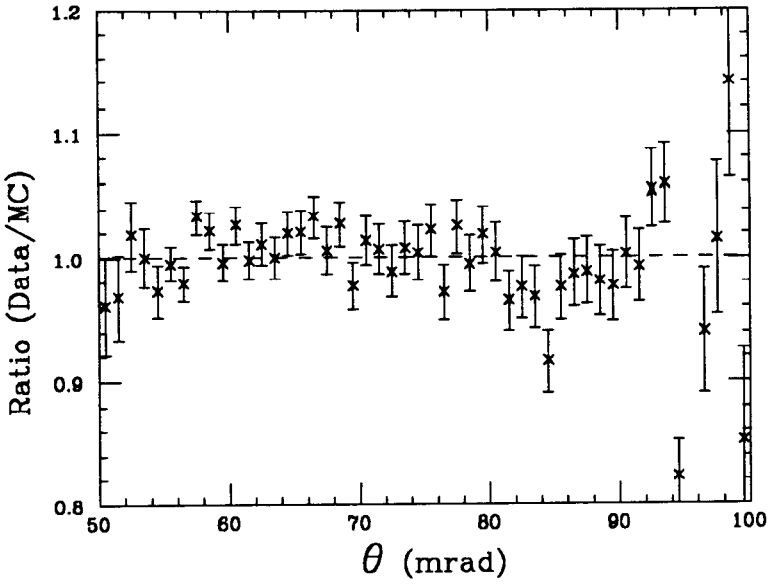

Figure B.3. Ratio of data to Monte Carlo for low angle Bhabha events. The error bars indicate statistical error only for each 1 mrad bin.

Appendix C

Veto Scintillators

The veto scintillator system (VS) was designed to provide charged/neutral particle identification. It is essentially a backup to the usual charge identification done with the central tracker. It is made up of four central scintillators mounted between the central tracker and the lead-glass boxes, and four forward scintillators mounted between the inner forward shower counters and the lead-glass boxes. There are no gaps in the coverage down to 90 mrad polar angle. This system was also used for beam noise monitoring and cosmic ray triggering.

The central veto scintillators consisted of four units, each 225 × 33.5 × 2 cm in dimension, the long dimension aligned in the Z direction. There was one unit mounted against the inside face of each lead-glass box. Each unit was made of two sheets of 1 cm thick Kyowa SCSN-38 plastic scintillator (giving a total 2 cm thickness) enclosed in 0.016 inch sheet metal and aluminum foil. Each unit was read out on both ends in Z by Kyowa Y7 wave bar attached to an Amperex XP2212C photomultiplier tube. The phototube was enclosed in a μ-metal shield to reduce the effect of external magnetic fields. The wave bar was 0.5 cm thick and 2.2 cm wide and was simply pressed up against the end of the scintillators before wrapping with aluminum foil and black photographic tape. Optical Stycast 6061 epoxy was used to glue one end of the wave bar to a lucite adapter, which was in turn glued to the phototube. On-line calibration was achieved by pulsing a green LED glued into the lucite adapter.

The forward veto scintillators consisted of four units mounted transversely to

the beam line. Each unit measured 60 cm high, 32 cm wide and 2 cm thick. They had a 13 cm radius cutout centered 2 cm back from one edge (see Figure C.1). All materials were the same as that used for the central scintillators. A pair of scintillators was mounted on the inside face (towards the interaction point) of each inner shower counter in such a manner that there was a 4 cm overlap region. Each scintillator is read out on three side by wave bar and two phototubes (see Figure C.1). The scintillators were mounted on 1/4 inch aluminum plate, which were then mounted to the shower counters using stand offs (to allow for the scintillators to overlap).

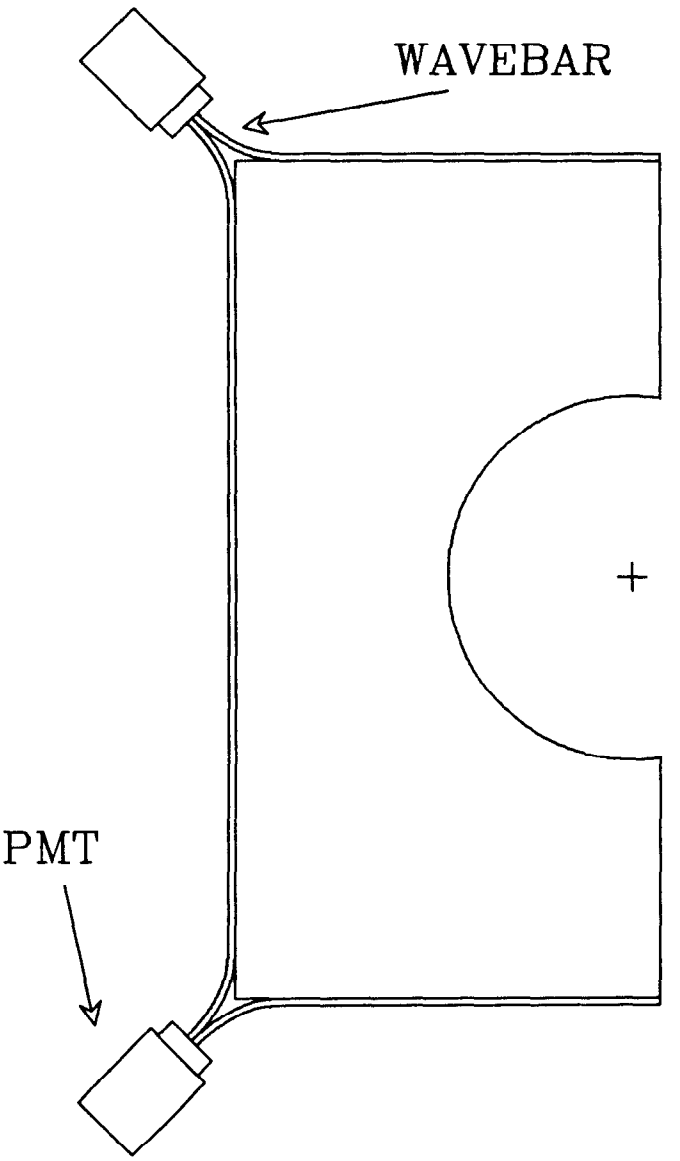

Figure C.1. Forward veto scintillator.

The response to single minimum ionizing particles was measured using cosmic rays. The central scintillators measured an average 25 photoelectrons in both phototubes summed together per muon. The forward scintillators measured an average 30-35 photoelectrons (depending on position in the scintillator) per muon.

The veto scintillators were not used for tracking purposes. After all other tracking had been done, a Z position was determined in the central scintillators by comparing the signals of the phototubes at each end, and this position was assigned to the nearest charged track, but was not included in the global track fit. However, the scintillators were quite useful in making special triggers, monitoring beam noise and providing information useful for the hand scanning of events.

Appendix D

Forward PWC System

The Forward PWC (FP) system provided tracking in the forward regions (less than 300 mrad with respect to the beam line). It consisted of planes of proportional wire chambers placed six radiation lengths into each of the four forward shower counter regions. (Six radiation lengths corresponds to the peak of the charged particle number distribution for showers initiated by 14.5 GeV electrons.)

In each shower counter region there were two planes of PWCs, one measuring the X coordinate and the other measuring Y. Each plane consisted of six chambers made of eight cell aluminum extrusions. Each eight cell chamber was 40 inches long, 8 inches wide and 5/8 inch thick with 1/16 inch thick walls (the same as the central PWCs, except shorter). Feed throughs made of G-10 fiberglass were glued to each end. Printed circuit boards mounted on the feed throughs provided pads for attaching the cell wire and for connecting to the high voltage and pre-amp cards. Each cell was strung with a 48 μm gold plated tungsten wire, which was soldered to the printed circuit boards using low resin solder. Feed through holes were sealed with RTV silicone rubber.

In order to clear the beam pipe, the two center chambers in each of the planes in the outer shower counters each had 3 cells cut so as to clear the three inch radius pipe (see Figure D.1). A rectangular plastic feed through was inserted into the inside end of each cut cell. Wires for the cut cells were strung through the entire length of

the chamber and soldered at both ends just like uncut cells. The wire was then glued to the inside plastic feed throughs by injecting a drop of epoxy into the feed through hole. After the epoxy set for 24 hours, the wires were then cut and sealed with RTV. The separated wire sections of a cut cell were simply connected by a shielded coaxial cable attached to the solder pads at each end. PWC extrusions in the inner shower counters had six cells cut so as to stay clear of the 100 mrad acceptance of the outer shower counters.

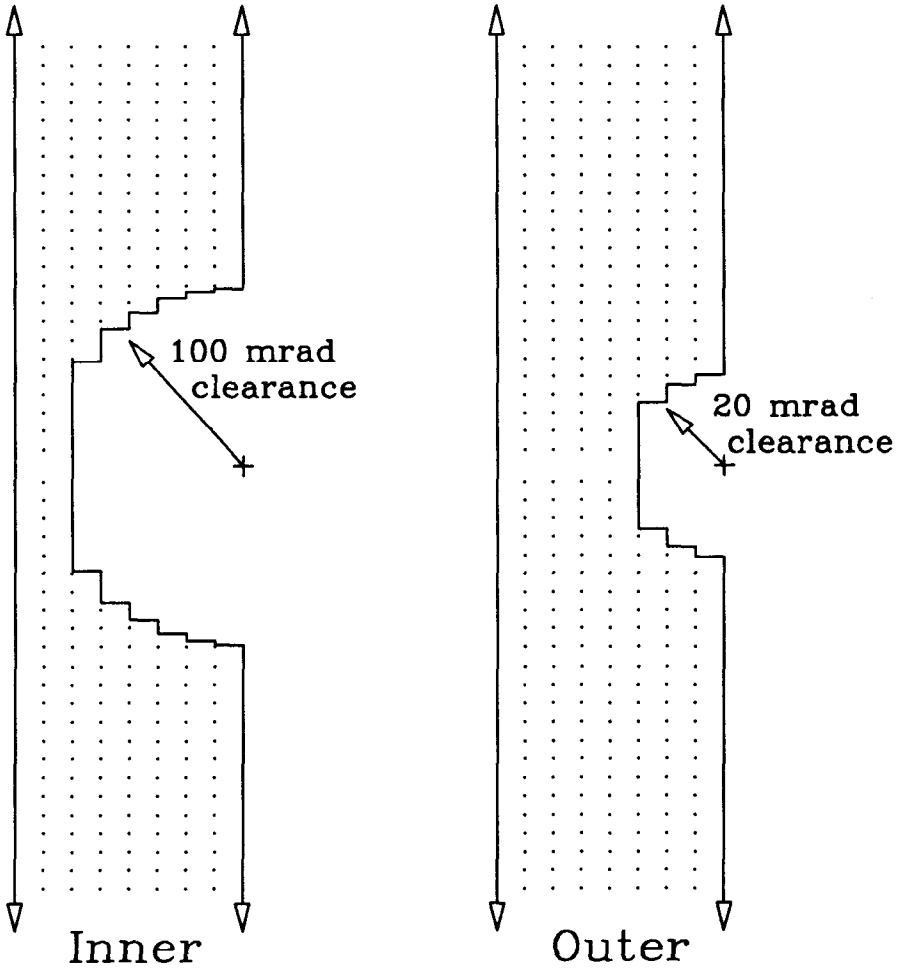

Figure D.1. Cut sections of the forward porportional wire chambers which are next to the beam pipe.

The precise location of the PWCs were determined in an off-line data analyses. The chambers in each plane were carefully bolted to the shower counters, but their positions were not surveyed. The actual positions for the PWCs in the outer shower

counters were determined by selecting back-to-back Bhabha events that had very clean drift chamber tracking. A straight line was fitted through the drift chamber hits (without using the interaction point in the fit) and the projection of the fitted line at the PWC planes was obtained. Events were chosen that had tracks which projected into the central four cells of an eight cell chamber. This requirement insured that the shower position was measured almost exclusively by the hit chamber, so that the chamber position could be determined independently of the other chamber positions. The difference in the projected position (from the drift chambers) to the measured position (in the PWC) was histogrammed, then fitted with a Gaussian function. The PWC positions were then corrected by the mean residual as given by the fitted Gaussian function, and the Bhabha event sample reanalyzed with the new positions. The Gaussian fit was somewhat unstable between iterations of new positions because the event sample changed (due to the requirement that the tracks project into the center four cells) and because the Gaussian was fitted to a histogram and was sensitive to the binning selected. The process was stopped after six iterations when no more significant improvement was observed. The remaining residuals for all chambers are shown in Figure D.2, and the standard deviation of this figure is used as an estimate of the uncertainty of the chamber positions. This uncertainty is 0.65 mm (equivalent to 0.16 mrad in polar angle). (As a comparison, the drift chamber positions were surveyed to an accuracy of 0.05 mm.) The tracking resolution (on an event by event basis) was simply determined from the standard deviation of the residual distribution when no selection is made to have the track enter the central four cells of a chamber. It was determined to be $\sigma_x = 8.15 \pm 0.12$ mm and $\sigma_y = 7.34 \pm 0.12$ mm (≈ 2 mrad in polar angle). The x and y values differ because the y planes are closer to the IP, so the shower is slightly narrower when crossing the y plane as compared to the x plane. The knowledge of these positions and resolutions was particularly important for determining the luminosity using low angle Bhabha events.

The inner PWCs were aligned using minimum ionizing particles created by stray beam particles hitting the beam pipe and masking outside of the detector. These minimum ionizing particles were tracked by the drift chambers, and the resulting

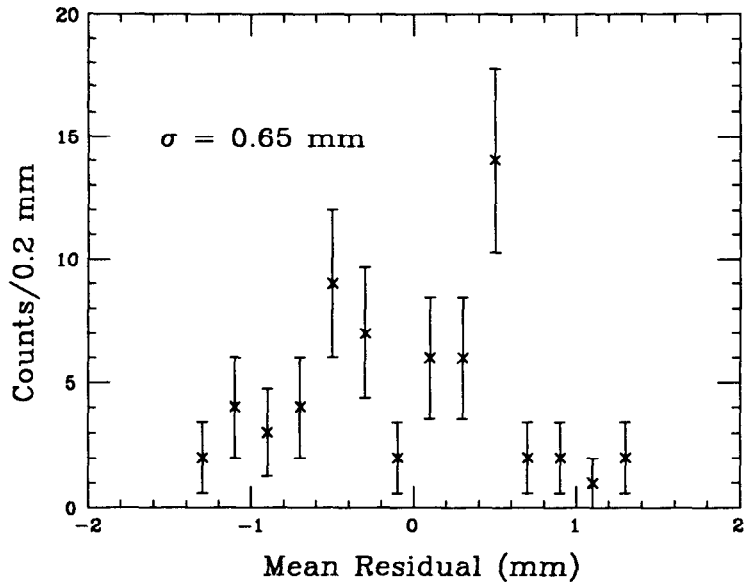

Figure D.2. Distribution of the outer forward porportional wire chamber mean residuals. There is one entry for each chamber for each of the two running cycles, for a total 48 entries.

projected position compared with the actual position measured in the inner PWC planes. This method was necessary because the drift chambers were the only accurate tracking system in the ASP detector and they were located behind the inner shower counters (as seen from the interaction point). It was not necessary to confine the particle to project into the central four cells of a chamber because the minimum ionizing particles did not shower, leaving a signal in only one cell. The distribution of residuals (the difference between the PWC hit and the position projected from the drift chambers) was histogrammed and fitted with a Gaussian function in a manner similar to the procedure used for the outer shower counters. The position of the planes was determined with an uncertainty of 3 mm in both x and y (equivalent to 2 mrad in polar angle).

Appendix E

Detector Simulation

The ASP detector simulation program is designed to accurately mimic the raw detector response for hypothetical events. The program uses the EGS4[7] shower simulation code to simulate the electron-photon cascades initiated by high energy electrons, positrons and photons. All elements of the central detector use EGS4. The forward shower counters and PWCs use a cruder simulation method which simply assigns signals to the forward elements based on the incoming particle parameters and random fluctuations as given by Gaussian distributions and the tracking and energy reconstruction resolutions of the forward elements.

The EGS4 shower simulation code is a package of subroutines which develop electromagnetic cascades based on Monte Carlo simulation of the various electromagnetic scattering processes. It requires the user to provide a main driver routine, a geometry routine and a data accumulation routine. EGS works by taking the initial incoming particle and, using a Monte Carlo technique, calculates where the first major interaction (such as Bremsstrahlung, Compton scatter, *etc.*, but not ionization) will take place, and then calls the geometry routine HOWFAR to see if the particle can be transported to the interaction location without crossing a detector element boundary. If no boundary is crossed, then the particle is transported, energy loss due to ionization calculated, and the appropriate interaction takes place. When the particle is transported, EGS calls the user provided data collection routine, AUSGAB. Any new energetic particles created by the selected interaction are added to the current

list of particles in the cascade, with the lowest energy particle at the head of the list. Particles are discarded when they fall below a total energy cut, which, for the Monte Carlo simulations performed in this thesis, is 0.5 MeV for photons and 1.5 MeV for electrons and positrons.

As the shower develops, EGS4 repeatedly calls the geometry routine HOWFAR to see if it is okay to transport a given particle a requested distance without crossing a detector boundary (such as between two lead-glass bars). Fortunately, all central detector elements (other than the beam pipe) are rectangular in shape. This allows the geometry of all detector elements (and gaps between elements) to be calculated by two box geometry routines. The first box routine, BOX1, is for a simple rectangular box. The position and direction of the current particle is provided to it as arguments, as are the positions of the box walls and the region numbers of the detector elements or gaps that are beyond each wall. For example, this routine is used for simulating the geometry of individual lead-glass bars. The second box routine, BOX3, is for a shell which encloses all six sides of a box. This routine is used for the aluminum box in which the lead-glass is stacked and for various small buffer spaces (gaps) surrounding detector elements. All wall positions are calculated in the program initialization so that no computer time is wasted recalculating them every time HOWFAR is called.

Every time a particle is transported, EGS calls the data accumulation routine AUSGAB. Čerenkov light is collected for the lead-glass bars and ionization deposition is collected for the proportional wire chambers and the veto scintillators. Sums of actual energy deposited in every detector element (including structural members) is also accumulated for diagnostic purposes. After the event is simulated, the signals are normalized to the level of actual detector response, and then they are inversely modified by the gain and offset correction factors for each PMT or wire chamber so that the raw signal of the detector is simulated. The signal in the lead-glass bar phototubes is smeared using a Gaussian probability distribution in order to reflect the presence of electronic noise and uncertainties in the PMT gain correction factors. (The level of this smearing was chosen such that the energy resolution from the

detector simulation matched that of the real data — $\sigma_E/E = 10\%/\sqrt{E}$.) In order to account for random signals in the detector (*i.e.* random electronic noise, stray beam particles, cosmic rays, etc.) the signal from random beam crossings (as taken with the real detector) are overlayed with the simulated signal. The detector trigger is then simulated, and the total raw signal is then packed into the same data format as the real data.

The normalization of the signals in the lead-glass bars is complicated by the attenuation of the Čerenkov light and light collection efficiencies, which are dependent upon the angles and position of the particles traversing the lead-glass. The light attenuation and collection functions were determined using cosmic ray muons. The signal was modified by these functions, where the angles of the original incoming particle (not the individual particles in the cascade) are used as the angles supplied to the correction functions. The supplied position is the intercept point of the original incoming particle with the appropriate lead-glass layer. (If the layer is not intercepted, then the nearest end of the layer is used.) These are the same functions which are used to correct the raw signal when determining the energy of a track in the data analysis. Hence, these functions are used to inversely modify the simulated signal. An attempt was made to correct the light emitted by the individual particles in the cascade (based on its position and angles), but the actual detector response was better simulated by using the original particle's angles. Modifying the signal by these functions is crucial, since the light collection can vary by a factor of three from one end of the bar to the other (see Figure E.1).

The signal in the calorimeter proportional wire chambers also suffers a complication. The signal collected in AUSGAB is the primary ionization deposited by charged particles traversing the gas. In a PWC cell, the free electrons are drawn towards the high voltage wire at the center of the cell. When the electrons reach the high field near the wire, they ionize more atoms in the gas, causing an avalanche of electrons. The resulting electrons are collected on the wire, and provide the signal of the cell. Ideally, this signal is linearly proportional to the amount of primary ionization.

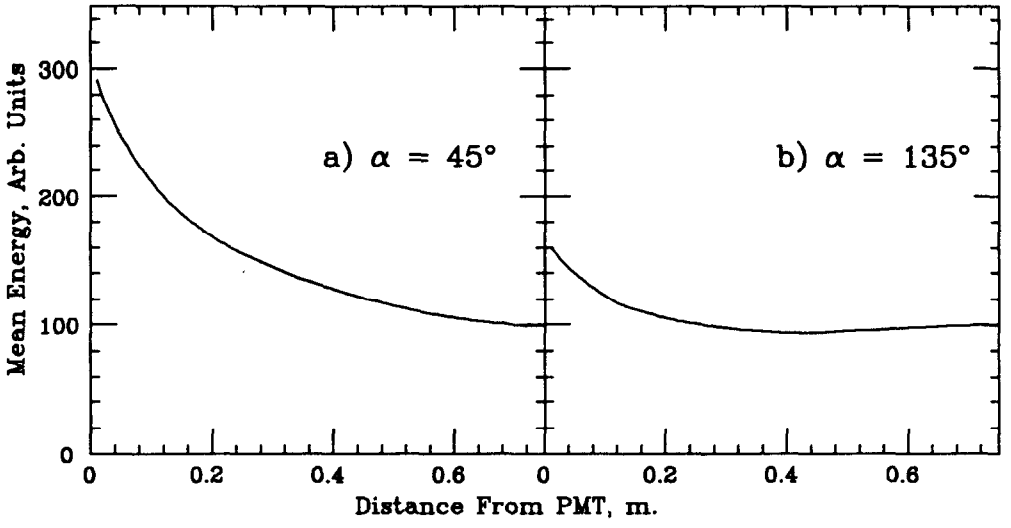

Figure E.1. Attenuation in the lead glass bar as a function of distance and angle. In a), the track is pointing towards the PMT at an angle of 45° with respect to the long axis of the bar, and in b) it is pointing away.

Unfortunately, the amount of primary ionization induced by high energy showers (more than a few GeV) in the calorimeter is high enough such that the avalanche near the wire begins to saturate the gas (*i.e.* a large fraction of the gas molecules were ionized). This effect (know as space charge saturation) is simulated by correcting the total signal in each PWC cell (after all particles in the event have been processed) by a saturation function, so that the typical total PWC signal and typical maximum single cell signal in the detector simulation for a shower at a given energy and angle matches the typical signal for real data events with the same energies and angles.

The detector simulation was calibrated using kinematically fitted $e^+e^-\gamma$ events (see Section 2.4). This was done by taking the track parameters for the central track from the kinematic fit result and then passing these parameters on to the Monte Carlo simulation program. The simulated detector response could then be compared directly with the actual response on an event by event basis. This proved to be a very powerful technique for the study of the performance of the simulation program. For example, it was this technique that was used to provide most of the simulated signal normalization factors, the space charge saturation functions for the PWC, and many of the simulation performance numbers used to calculate the uncertainties in

the prediction of the α^4 cross sections in Chapter 5.

References

1. F. A. Berends *et al.*, Nucl. Phys. **B253** (1985) 441
2. F. A. Berends *et al.*(CALKUL Collaboration), Nucl. Phys. **B239** (1984) 395
3. F. A. Berends *et al.*(CALKUL Collaboration), Nucl. Phys. **B264** (1986) 265
4. B. W. Lynn, M. E. Peskin and R. G. Stuart, SLAC-PUB-3725, 1985.
5. O. I. Dahl *et al.*, Group A Programming Note P-126, University of California, Lawrence Radiation Laboratory, 1968
6. P. Grannis, D. Jaffe and M. Marx, Nucl. Instr. and Meth. **188** (1981) 239
7. W. R. Nelson *et al.*, SLAC-Report-265, 1985 (unpublished).
8. N. A. Roe, Ph. D. Thesis, Stanford University, 1989
9. C. Hearty, Ph. D. Thesis, University of Washington, 1987
10. E. Cisnero *et al.*, IEEE Trans. Nucl. Sci. **NS-28** (1981) 465
11. M. Breidenbach *et al.*, IEEE Trans. Nucl. Sci. **NS-25** (1978) 706
12. F. A. Berends *et al.*, Comp. Phys. Comm. **40** (1986) 285
13. E. Byckling and K. Kajantie, New York, Wiley, 1973
14. Dan T. Gillespie, Ph. D. Thesis, The Johns Hopkins University, 1968
15. Kiyotomo Kawagoe, *private communication*
16. R. Kleiss *et al.*, Comp. Phys. Comm. **40** (1986) 359
17. Courtesy of Tom Steele, fellow ASPian

18. N. Brown, K. Hagiwara and A. D. Martin, Nucl. Phys. **B288** (1987) 782

19. F. A. Berends, R. Kleiss and W. Hollik, Nucl. Phys. **B304** (1988) 712

20. K. J. F. Gaemers, Ph. D. Thesis, Leiden (1974). F. A. Berends, K. J. F. Gaemers and R. Gastmasn, Nucl. Phys. **B68** (1974) 561. M. E. Levi, Ph. D. Thesis, Harvard University (1984) 97.